

CMS Draft Analysis Note

The content of this note is intended for CMS internal use and distribution only

2020/09/05

Head Id: 456230

Archive Id:

Archive Date: 2018/04/18

Archive Tag: trunk

Measurement of B_s^0 meson production in PbPb collisions at $\sqrt{s_{NN}} = 5.02$ TeV

Zhaozhong Shi¹, Júlia Silva², Gwang-jun Kim¹, Jing Wang¹, Nuno Leonardo², and Yen-Jie Lee¹

¹ Massachusetts Institute of Technology

² Técnico Lisboa

Abstract

We present the measurements of the differential corrected yield $\frac{1}{T_{AA}} \frac{dN}{dp_T}$ for B_s^0 mesons with 2018 PbPb collisions at $\sqrt{s_{NN}} = 5.02$ TeV. The exclusive decays $B_s^0 \rightarrow J/\psi \phi$ are used to detect B_s^0 mesons and to obtain the production measurements. The ratios of the B_s^0 and the B^+ cross section vs p_T and centrality are also presented, allowing to probe strangeness enhancement in the QGP environment.

This box is only visible in draft mode. Please make sure the values below make sense.

PDFAuthor: Zhaozhong Shi, Julia Silva, Gwang-jun Kim, Jing Wang, Nuno Leonardo, Yen-Jie Lee
PDFTitle: Measurement of B_s meson production in PbPb collisions at 5.02 TeV
PDFSubject: CMS
PDFKeywords: CMS, physics, B meson, B_s meson, PbPb collisions, quark gluon plasma, open heavy flavor

Please also verify that the abstract does not use any user defined symbols

1 Version Notice

- 2 Answer to the re-approval comments HIN conveners: https://espace.cern.ch/cms-heavyion/hf/hin19011/_layouts/15/WopiFrame.aspx?sourcedoc=/cms-heavyion/hf/hin19011/Shared%20Documents/Answer%20to%20Re-approval%20Comments/Answer%20to%20HIN-19-011%20Re-approval%20Comments.docx&action=default
- 3 Since the re-approval presentation date on 04/24/2020 for the CADI HIN-19-011, we have
4 addressed all the comments from the HIN conveners and updated our studies in this B_s^0 AN-
5 19-055 and the complimentary B^+ AN-19-132. The major changes in the sections of this AN are
6 summarized as below:

10 No major changed except minor text update is made in the following sections:

11 **Introduction**

12 **B_s^0 meson reconstruction and base selections**

13 **B_s^0 meson selection optimization**

14 **B_s^0 candidate properties comparison between data and MC**

15 **Appendix A Cut Optimization**

16 **Appendix B Systematics**

17 **Appendix C Non-prompt Lg background**

18 We have made the changes in the following sections:

19 **Important changes**

20 **Dataset**

- 21 1. Figure 1 the generated B^+ , B_s^0 , and J/ψ pt distribution before and after \hat{p}_T reweighting
22 has been added.

23

24 **Signal Extraction**

- 25 1. Table 9 the comparison between symmetric and asymmetric uncertainties in the raw yield
26 extraction has been added.

27

28 **Acceptance and Efficiency**

- 29 1. Line 450 - 469 the detailed definitions of acceptance α , selection efficiency ϵ , and efficiency
30 correction factor $\langle \frac{1}{\alpha \times \epsilon} \rangle$ have been added.
- 31 2. Table 10 the minimum statistics bin RECO statistics in the 2D map for each p_T and cen-
32 trality bin has been added.

33

- 34 3. A dedicated 7.7 section for the use of sPlot weight and comparison of the sPLOT weighted
35 with the nominal unweighted efficiency correction factors have been added.

36 **Closure Test of the Corrected Yield**

- 37 1. small samples → data-like samples
38 2. We have adjusted the 7 - 10 GeV/c p_T bin to have a background 20 instead of 100 to obtain
39 a good closure in Fig 52 and updated the statistical uncertainties in Table 20
40 3. Figure 54 for the asymmetric statistical uncertainties on the efficiency correction factor
41 $\langle \frac{1}{\alpha \times \epsilon} \rangle$ has been added.
42 4. Table 16 the reused events percentage summary has been added
43 5. Table 21 the comparison between the statistics uncertainties of raw yield, efficiency cor-
44 rection factor, and corrected yield has been added.

45 **Results**

- 46 1. Table 24 the table of sum of 0 - 30%, 30 - 90%, and 0 - 90% of minimum biased events has
47 been added.
48 2. Table 25 B_s^0 cross section and Table 29 B_s^0/B^+ ratio for 7 - 10 GeV/c bin has also been
49 updated. The uncertainties on the B_s^0 cross section goes from +52.7% → +42.9% and -
50 47.4% → -41.4%. The B_s^0/B^+ ratio goes from +57.6% → +48.9% and -53.1% → -47.9%.

51 **Systematics uncertainties**

- 52 1. More detailed descriptions with each step (muon identification, muon trigger, and the
53 tracking) on the TnP analysis (line 780 - 795) and the plots of their contributions to the
54 systematics individually have been added.

Contents

55	1	Introduction	1
56	2	Datasets, MC samples and event selection	2
57	2.1	Datasets	2
58	2.2	Event Selection	2
59	2.3	MC samples	2
60	2.3.1	MC re-weighting	4
61	3	B_s^0 meson reconstruction and base selections	10
62	3.1	B_s^0 meson reconstruction	10
63	3.2	Muon and J/ψ candidates selection	10
64	3.3	Track and ϕ candidate selection	17
65	3.4	ϕ and J/ψ candidates studies vs rapidity	18
66	4	B_s^0 meson selection optimization	22
67	4.1	Cut optimization	22
68	5	B_s^0 candidate properties comparison between data and MC	33
69	6	Signal Extraction	37
70	7	Acceptance and Efficiency	46
71	7.1	Overview	46
72	7.2	$2D \frac{1}{\alpha \times \epsilon}$ vs $B p_T$ and $B y $ Map	46
73	7.3	MC RECO and GEN Statistics	49
74	7.4	Efficiency Correction Over Fiducial Region	51
75	7.5	Event-By-Event Reweighting Techniques	53
76	7.6	Final Results	53
77	7.7	sPlot Weight Techniques Studies	55
78	8	Closure Test of the B_s Corrected Yield	59
79	8.1	Closure Test on the Raw Yield Fits	59
80	8.1.1	Validation of Raw Yield and Raw Yield Error from the Fits	64
81	8.2	Closure Test on Efficiency Correction	67
82	8.2.1	High Statistics Limit	67
83	8.2.2	Low Statistics Limit	67
84	8.3	Conclusion	71
85	8.4	Data Bootstrap to Estimate the Statistical Uncertainties	71
86	9	Results	82
87	9.1	Number of minimum biased events evaluation	82
88	9.2	dN/dp_T in PbPb collisions at 5.02 TeV	84
89	9.3	B_s^0 to B^+ corrected yield ratio	84
90	10	Systematic uncertainties	89
91	10.1	Number of minimum biased events	89
92	10.2	Branching ratio	89
93	10.3	Tracking efficiency	90
94	10.4	Muon efficiency: Tag and Probe	90
95	10.5	Selection efficiency	95
96	10.5.1	Overview	95

98	10.5.2 Systematics Associated with Data-MC Disagreement	95
99	10.5.3 Systematics Associated with MC Statistics	98
100	10.6 Systematics associated with signal extraction	101
101	10.7 Systematics on p_T shape	116
102	10.8 Summary table	117
103	10.9 Additional studies: Invariant mass of BDT variables	120
104	A Cut Optimization	128
105	B Systematics	134
106	B.1 Selection Efficiency	134
107	B.2 Signal Extraction	137
108	C Non-prompt J/ ψ background	141
109	C.1 Individual channel contributions of NP Background	141
110	C.2 B meson contribution of NP Background	143

DRAFT

111 1 Introduction

112 The study of heavy-quark production plays a crucial role in understanding the mechanisms of
 113 heavy-quark interaction with the medium created in heavy-ion collisions. Heavy quarks are
 114 primarily produced at early stages of heavy-ion collisions, and therefore they carry informa-
 115 tion about the pre-thermalization properties of the quark gluon plasma. Compared with light
 116 quarks and gluons, heavy quarks are expected to lose less energy due to smaller color charge
 117 and the dead cone effect [1]. As a consequence of this phenomenon, several theoretical cal-
 118 culations predict sizable differences in the suppression pattern of light particle versus that of
 119 charmed and beauty mesons, in central PbPb collisions. Using the high luminosity LHC runs
 120 of pp and PbPb collisions at 5.02 TeV, the CMS collaboration was able to measure already the
 121 cross-sections of charged particles [2] and of D^0 mesons [3] in different centrality ranges. The
 122 two measurements show a very similar suppression in a very wide transverse momentum in-
 123 terval (from 2 to 100 GeV/c). The goal of the present analysis is to test the flavour dependence
 124 of energy loss and to study the hadronization of beauty quark, by measuring the exclusive
 125 production of B_s^0 mesons in PbPb collisions in a similar kinematic range ($7 < p_T < 50$ GeV/c).
 126 Furthermore, the measurement of the suppression of strange beauty particles in heavy-ion col-
 127 lisions is considered of fundamental importance to study the mechanisms of beauty hadroniz-
 128 zation in heavy ion collisions. In presence of a medium with increased strangeness content, the
 129 relative yield of B_s^0 mesons with respect to non-strange beauty mesons at low-intermediate p_T
 130 can be enhanced in nucleus-nucleus collisions as compared to pp interactions if recombination
 131 is a relevant mechanism of beauty hadronization in the QGP.

132 In this note, the production of the B_s^0 meson in PbPb collisions at 5.02 TeV is studied. The B_s^0
 133 mesons are measured in the rapidity region $|y_{\text{lab}}| < 2.4$, via the full reconstruction of the decay
 134 channel: $B_s^0 \rightarrow J/\psi \phi$ with branching fraction $\mathcal{B} = (3.12 \pm 0.24) \times 10^{-5}$. At low p_T 7-10GeV/c,
 135 most candidates are confined to the forward rapidity region largely due to limited detector
 136 muon acceptance. In this p_T range we adopt fiducial region which is $1.5 < |y_{\text{lab}}| < 2.4$.

137 To probe enhancement with respect to non-strange mesons, the ratios between B_s^0 corrected
 138 yield and the one obtained for B^+ vs p_T and centrality are also presented. The cross-section
 139 measurement was already performed using PbPb datasets, collected at 5.02 TeV, in the 2015
 140 LHC run, with still rather large statistical and systematic uncertainties [4]. Using the 2018
 141 PbPb dataset, with around 3 times more data, a more precise measurement can be obtained
 142 and better constraints on theoretical predictions can be achieved.

143 2 Datasets, MC samples and event selection

144 2.1 Datasets

145 This analysis is performed using the 2018 PbPb data at $\sqrt{s_{\text{NN}}}=5.02$ TeV, which has an integrated
 146 luminosity of 1.7 nb^{-1} . The analysis uses the dimuon primary datasets (*DoubleMu PD*). The
 147 full name of the used datasets can be found in Table 1.

Table 1: List of PbPb HLT datasets and triggers with the corresponding integrated luminosities used in the analysis.

System	Primary dataset	Trigger	Luminosity
PbPb	/HIDoubleMuonPsiPeri/HIRun2018A-04Apr2019-v1/AOD	HLT_HIL3Mu0NHitQ10_L2Mu0_MAXdR3p5_M1to5_v1	$533 \mu\text{b}^{-1}$
PbPb	/HIDoubleMuon/HIRun2018A-04Apr2019-v1/AOD	HLT_HIL3Mu0NHitQ10_L2Mu0_MAXdR3p5_M1to5_v1	$1124 \mu\text{b}^{-1}$
PbPb	Combined All		$1.657 (\sim 1.7) \text{ nb}^{-1}$

148 The PbPb analysis codes are running under the CMSSW_10_3_1_patch3 version, and the global
 149 tag (GT) used for processing these samples is 103X_dataRun2_Prompt_v3.

150
 151 Events used in the measurement are collected with a trigger requiring the presence of two
 152 independent muon candidates. No selection is applied on momentum (including transverse
 153 momentum) or pseudo-rapidity. A list of the various triggers with the corresponding inte-
 154 grated luminosities can be found in Table Tab. 1. The PbPb paths had different prescale values
 155 in different runs during the data taking period. A complete description of the di-muon datasets
 156 and HLT triggers can be found in [5]. Muon JSON file is applied to filter the PbPb dataset.

157 2.2 Event Selection

158 To extract pure collision events, several offline selections are applied to each event:

- 159 • `pprimaryVertexFilter`: Events are required to have at least one reconstructed
 160 primary vertex. The primary vertex is formed by two or more associated tracks and
 161 is required to have a distance from the nominal interaction region of less than 15 cm
 162 along the beam axis and less than 0.15 cm in the transverse plane.
- 163 • `phfCoincFilter2Th4`: An additional selection of hadronic collisions is applied
 164 by requiring a coincidence of at least 2 HF calorimeter towers, with more than 4 GeV
 165 of total energy, from the HF detectors on both sides of the interaction point.
- 166 • `pclusterCompatibilityFilter`: In addition to HF coincidence, a cluster com-
 167 patibility filter is used.

168 There is also a requirement on the centrality (`hiBin`) of the events to selection only 0 - 90%
 169 centrality class events: `hiBin < 181`.

170 2.3 MC samples

171 The PbPb sample is reconstructed using the CMSSW version CMSSW_10_3_1_patch3. The
 172 global tag used for the production is `75X_mcRun2_HeavyIon_v13` for PbPb samples. Dedi-
 173 cated PbPb B_s^0 samples were generated in order to estimate the acceptance and selection effi-
 174 ciencies, to study the background components, and to evaluate systematic uncertainties. PYTHIA8
 175 Tune CUETPM8 [6, 7], set to generate inclusive (all quark/antiquark, as well as gluon initiated)
 176 QCD processes, was used to generate at 5.02 TeV the signal. Several prefilters at the generation
 177 steps are applied in order to optimize the generation process and conserve resources. Only
 178 signal events were kept with at least one B_s^0 (forced to decay through the channel $B_s \rightarrow J/\psi \phi$
 179 by means of the `EVTGEN` package [8]), with $p_T > 5.0 \text{ GeV}/c$, and $|\eta| < 2.4$. In addition, the J/ψ

and ϕ meson, are forced to decay in the two muons and two kaons respectively. Final state radiations (FSR) are generated using PHOTOS [9]. The selected signal B PYTHIA8 events were embedded into a PbPb background simulated with the HYDJET (version 1.8, tune "Drum" for the prompt and non-prompt J/ ψ MC and tune "Cymbal5Ev8" for the B_s^0 signal MC) [10] event generator.

Around fifty thousand events were generated in 5 \hat{p}_T bins, with boundaries of [0, 5, 15, 30, 50], in both signal only, and embedded samples. The list of B_s^0 MC simulation samples used is:

- /Hydjet_Pythia8_BsToJpsiPhi_Pthat5_TuneCP5_5020GeV_Drum5Ev8/wangj-MC_20181231_Bpt5p0_103X_upgrade2018_realistic_HI_v7_REC0-db0f6d951682195192744a8077b2409c/USER
- /Hydjet_Pythia8_BsToJpsiPhi_Pthat10_TuneCP5_5020GeV_Drum5Ev8/wangj-MC_20181231_Bpt5p0_103X_upgrade2018_realistic_HI_v7_REC0-db0f6d951682195192744a8077b2409c/USER
- /Hydjet_Pythia8_BsToJpsiPhi_Pthat15_TuneCP5_5020GeV_Drum5Ev8/wangj-MC_20181231_Bpt5p0_103X_upgrade2018_realistic_HI_v7_REC0-db0f6d951682195192744a8077b2409c/USER
- /Hydjet_Pythia8_BsToJpsiPhi_Pthat30_TuneCP5_5020GeV_Drum5Ev8/wangj-MC_20181231_Bpt5p0_103X_upgrade2018_realistic_HI_v7_REC0-db0f6d951682195192744a8077b2409c/USER
- /Hydjet_Pythia8_BsToJpsiPhi_Pthat50_TuneCP5_5020GeV_Drum5Ev8/wangj-MC_20181231_Bpt5p0_103X_upgrade2018_realistic_HI_v7_REC0-db0f6d951682195192744a8077b2409c/USER

In addition to the signal samples, inclusive non-prompt J/ ψ samples, which include several different B meson decaying to J/ ψ channels, were also generated. These samples were used to determine the peaking background appearing in the $\mu\mu KK$ mass spectrum. The following samples were used:

- /Pythia8_BJpsiMM_ptJpsi_00_03_Hydjet_MB/HINPbPbWinter16DR-75X_mcRun2_HeavyIon_v13-v1/AODSIM
- /Pythia8_BJpsiMM_ptJpsi_03_06_Hydjet_MB/HINPbPbWinter16DR-75X_mcRun2_HeavyIon_v13-v1/AODSIM
- /Pythia8_BJpsiMM_ptJpsi_03_06_Hydjet_MB/HINPbPbWinter16DR-75X_mcRun2_HeavyIon_v13_ext1-v1/AODSIM
- /Pythia8_BJpsiMM_ptJpsi_06_09_Hydjet_MB/HINPbPbWinter16DR-75X_mcRun2_HeavyIon_v13-v1/AODSIM
- /Pythia8_BJpsiMM_ptJpsi_06_09_Hydjet_MB/HINPbPbWinter16DR-75X_mcRun2_HeavyIon_v13_ext1-v1/AODSIM
- /Pythia8_BJpsiMM_ptJpsi_09_12_Hydjet_MB/HINPbPbWinter16DR-75X_mcRun2_HeavyIon_v13-v1/AODSIM
- /Pythia8_BJpsiMM_ptJpsi_12_15_Hydjet_MB/HINPbPbWinter16DR-75X_mcRun2_HeavyIon_v13-v1/AODSIM
- /Pythia8_BJpsiMM_ptJpsi_15_30_Hydjet_MB/HINPbPbWinter16DR-75X_mcRun2_HeavyIon_v13-v1/AODSIM
- /Pythia8_BJpsiMM_ptJpsi_30_inf_Hydjet_MB/HINPbPbWinter16DR-75X_mcRun2_HeavyIon_v13-v1/AODSIM

The inclusive non-prompt J/ ψ samples are also used in the B^+ analysis [11]

Finally, the following prompt J/ ψ samples were used:

- /Pythia8_JpsiMM_ptJpsi_00_03_Hydjet_MB/HINPbPbWinter16DR-75X_mcRun2_HeavyIon_v13-v1/AODSIM
- /Pythia8_JpsiMM_ptJpsi_03_06_Hydjet_MB/HINPbPbWinter16DR-75X_mcRun2_HeavyIon_v13-v1/AODSIM
- /Pythia8_JpsiMM_ptJpsi_03_06_Hydjet_MB/HINPbPbWinter16DR-75X_mcRun2_HeavyIon_v13_ext1-v1/AODSIM
- /Pythia8_JpsiMM_ptJpsi_06_09_Hydjet_MB/HINPbPbWinter16DR-75X_mcRun2_HeavyIon_v13-v1/AODSIM
- /Pythia8_JpsiMM_ptJpsi_06_09_Hydjet_MB/HINPbPbWinter16DR-75X_mcRun2_HeavyIon_v13_ext1-v1/AODSIM
- /Pythia8_JpsiMM_ptJpsi_09_12_Hydjet_MB/HINPbPbWinter16DR-75X_mcRun2_HeavyIon_v13-v1/AODSIM
- /Pythia8_JpsiMM_ptJpsi_12_15_Hydjet_MB/HINPbPbWinter16DR-75X_mcRun2_HeavyIon_v13-v1/AODSIM
- /Pythia8_JpsiMM_ptJpsi_15_30_Hydjet_MB/HINPbPbWinter16DR-75X_mcRun2_HeavyIon_v13-v1/AODSIM
- /Pythia8_JpsiMM_ptJpsi_30_Inf_Hydjet_MB/HINPbPbWinter16DR-75X_mcRun2_HeavyIon_v13-v1/AODSIM

2.3.1 MC re-weighting

For our MC reweighting, we reweight our MC directly to our data shape in the RECO level. We extract the data raw yield from the unbinned fit and the MC raw yield by count the total number of MC candidates with \hat{p}_T , PV_z , and centrality reweighting. The $J\psi$, B^+ , and B_s Gen p_T distribution before and after are shown below on Fig 1

We can see that after \hat{p}_T reweighting, the Gen p_T distributions have become smoother. This validate our \hat{p}_T reweighting procedures.

Then, we take the ratio of the normalized data raw yield to the normalized MC raw yield and perform a variety of functions to fit the distribution. In our studies, we use Linear ($y = p_0 + p_1x$), Quadratic ($y = p_0 + p_1x + p_2x^2$), Linear + Inverse ($y = p_1x + \frac{p_2}{x}$), Linear + Square Root ($y = p_0 + p_1x + p_2\sqrt{x}$), Linear + Log ($y = p_0 + p_1x + p_2 \log x$). The data vs MC raw yield shape and our fitting results on spectra ratio are show as follows on Fig 2

The fitting parameters for all functions are shown below on Table 2

Table 2: Summary of fitting parameters for the fitting functions above is shown above. We will use Linear + Log since its χ^2 is the smallest

Fitting Functions	p_0	p_1	p_2	χ^2
Linear	0.85	0.01	N/A	0.50
Quadratic	1.09	-0.016	0.00056	0.49
Linear + Inverse	7.187	0.030	N/A	0.45
Linear + Square Root	1.84	0.059	-0.45	0.43
Linear + Log	1.81	0.034	-0.500	0.40

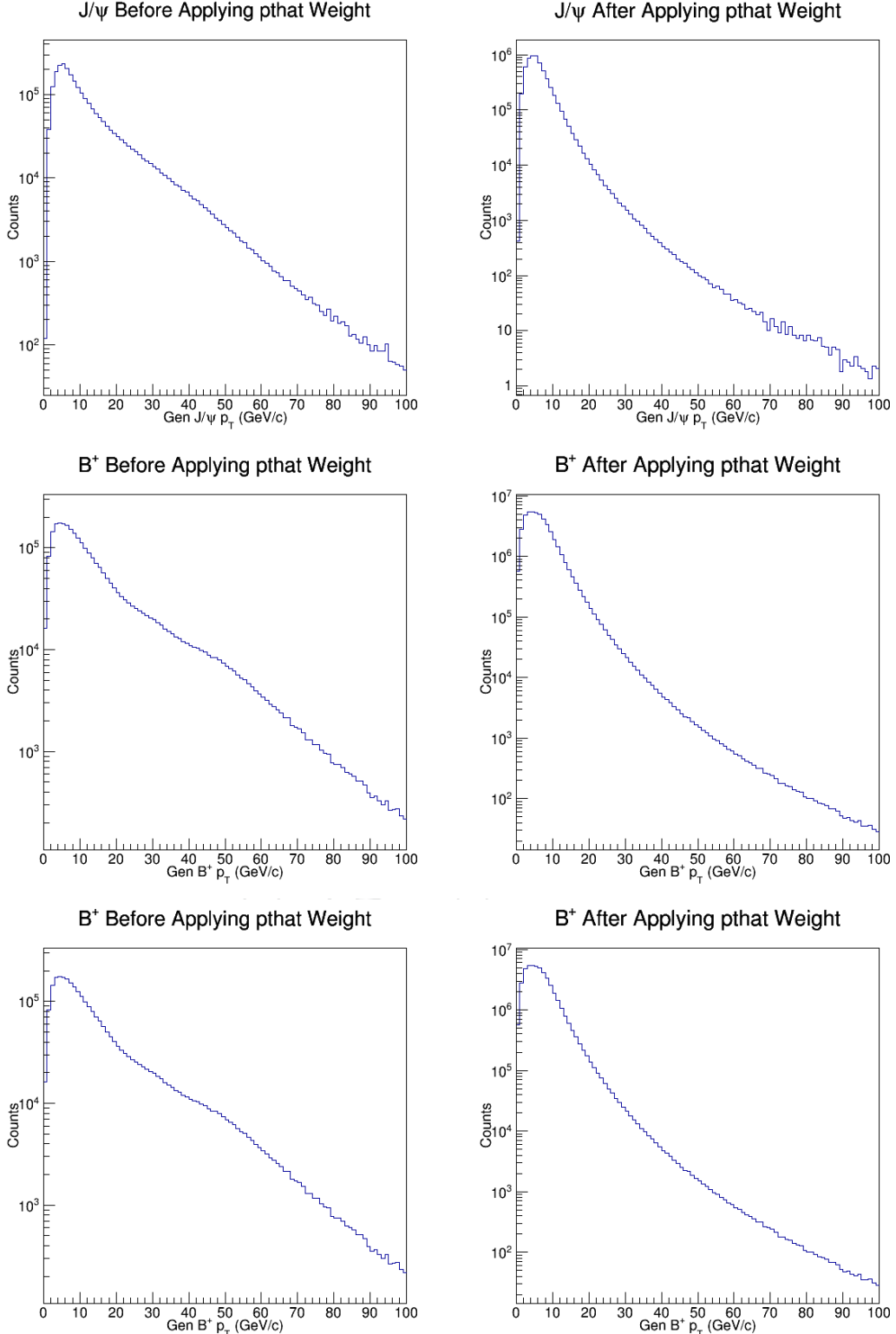


Figure 1: J/ψ generated p_T distribution before (upper left) and after (upper right) \hat{p}_T reweighting, B^+ generated p_T distribution before (middle left) and after (middle right) \hat{p}_T reweighting, and B_s^0 generated p_T distribution before (lower left) and after (lower right) \hat{p}_T reweighting are shown above.

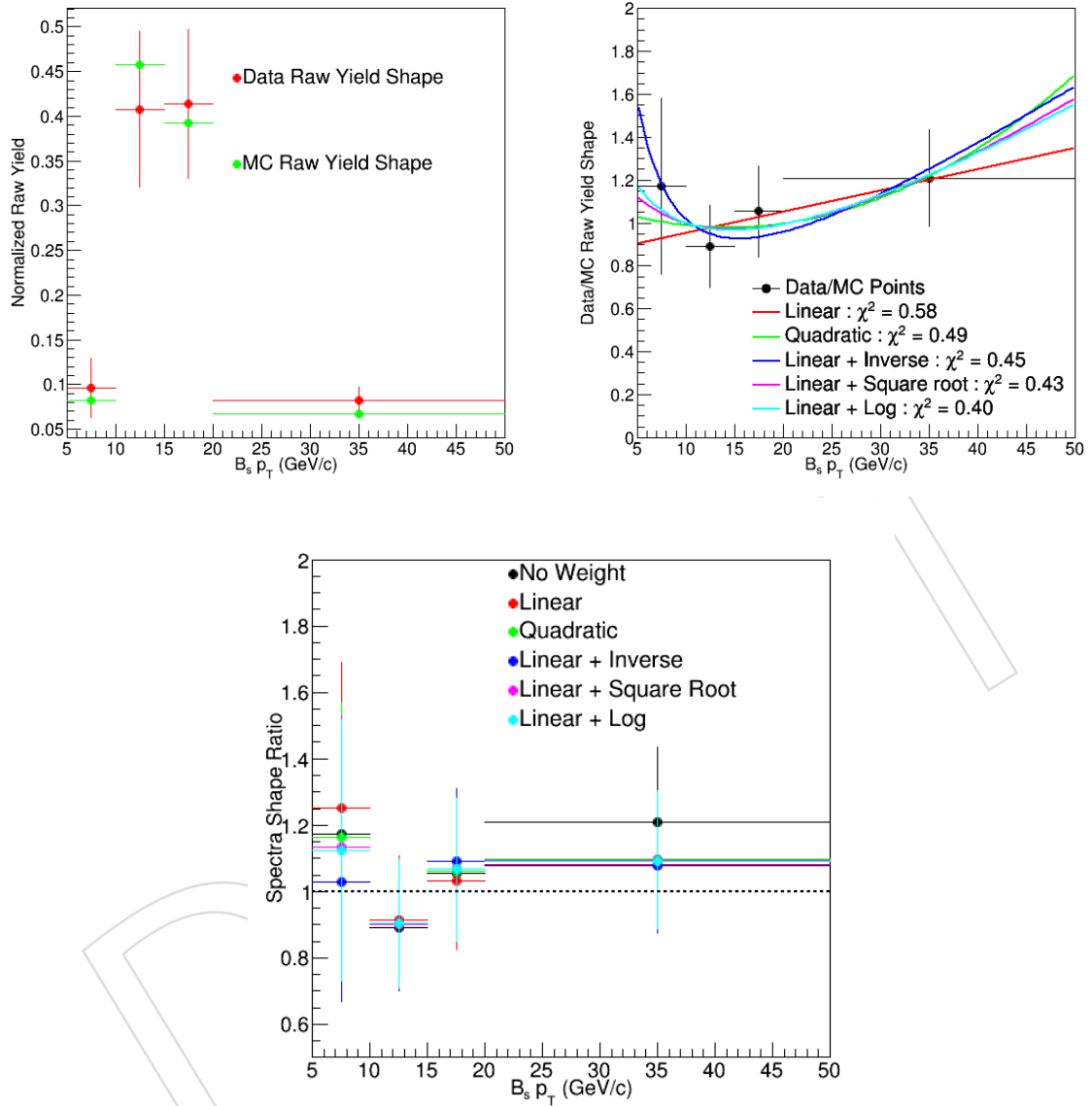


Figure 2: $B_s^0 p_T$ normalized raw yields obtained in PbPb MC and Data are shown above on the top left panel. The data/MC ratio and different fitting functions: Linear (Red), Quadratic(Green), Linear + Inverse (Blue), Linear + Square Root (Purple), and Linear + Log (Cyan) and their χ^2 are shown above on the top right panel. The bottom plots are the data/MC reweighted yields with different functions from the fit on the top right panel. We can see that they all get closer to unity compared unweighted MC. The Linear + Log (Cyan) line, which has the smallest χ^2 and is closest to unity after applying the weight to the MC. Hence, Linear + Log function is use as nominal for our $B_s^0 p_T$ reweighting. All other fitting function are used as reference to calculate the p_T shape systematic uncertainties.

234 Nevertheless, as we mention in Section 7, we will use $\langle \frac{1}{\alpha \times \epsilon} \rangle$ to correct the efficiency. The effect
 235 of p_T shape turns out to be negligible. Hence, we propose to use these weight only as variation
 236 to estimate the systematic uncertainties of the p_T shape on the final results.

237 The MC simulations are also re-weighted in order to match the centrality distribution in data.
 238 In the middle panel of Figure 3, the centrality distribution of the MC simulation (red) is com-
 239 pared to the one in data (blue), before the re-weighting. Each unit (HiBin) on the x-axis repre-
 240 sents 0.5% centrality. The number of binary collisions (N_{coll}) was used as the weight to scale
 241 the MC centrality, and the distribution presented in the right pannel of Figure 3 was obtained.

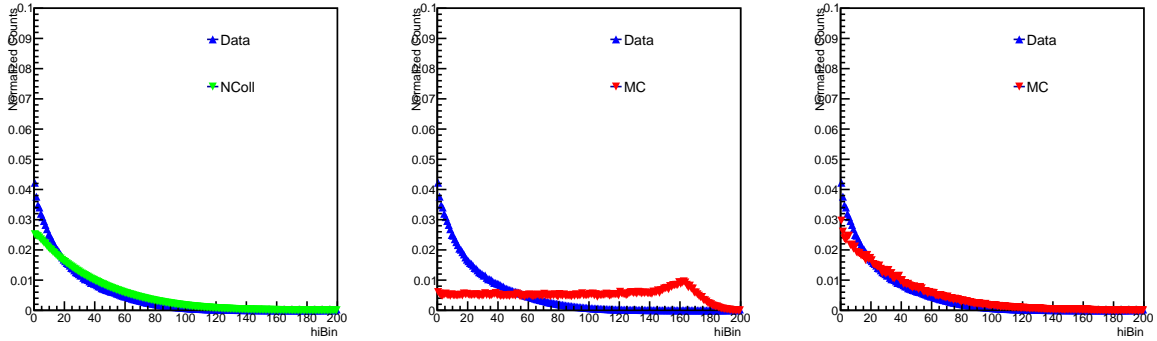


Figure 3: (Left) The comparison between N_{coll} and Data vs HiBin. (Middle) Centrality distribution of MC (red) and data (blue) in PbPb collisions in the centrality interval 0-100%. (Right) Ratio between the centrality distribution of data and MC fitted with a exponential function.

In addition to above pt shape and centrality re-weighting, there must be a primary vertex z position (PVz) re-weighting. It is known that the MB samples use for embedding for PbPb signal MC samples (with Cymbol5Ev8 tune) has a PVz offset. Also, the offsets between data and MC in the X and Y directions are observed in the 2018 PbPb collisions. A Gaussian fit is applied to both the data and MC PVz distributions, as showed in Fig. 4. The black markers represent the distribution points for MC (left), and data (right), while the red line represents the fit result. Then, the ratio between the two fit results is taken as the weighting function. The result after this weighting can be found in Fig. 4 But note that this analysis is not sensitive to the absolute value of the PV position because the reconstruction of the B_s^0 meson rely only on the relative distance between PV and B_s^0 reconstructed vertex which is presented in the following section.

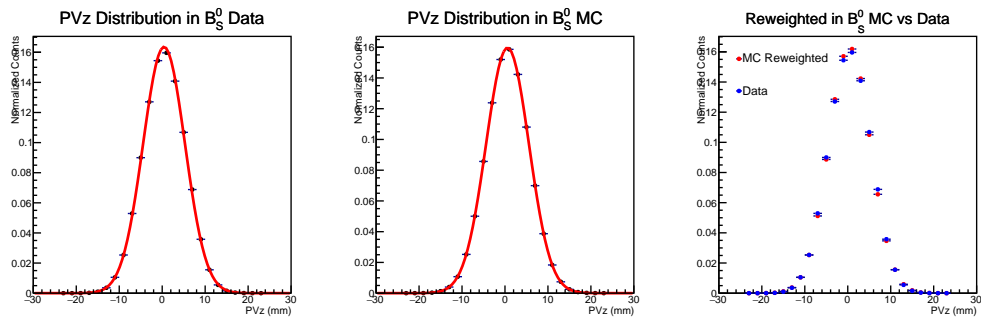


Figure 4: On the left, B_s^0 primary vertex z position (PVz) spectrum obtained in PbPb MC simulations (black marker), fitted with a gaussian function (red line). On the middle, the same but for the data. One the right is the MC and data after reweighting the MC to data with ratio of data-to-MC Gaussian Fits.

- ²⁵³ All the results derived using MC were obtained after applying the above re-weighting procedure with respect to p_T shape (only for p_T shape systematic studies), PVz and centrality .

DRAFT

255 3 B_s^0 meson reconstruction and base selections

256 The reconstruction procedure and preselection applied are described in this section. The pres-
 257 election includes all the cuts applied to the datasets before any selection optimisation.

258 3.1 B_s^0 meson reconstruction

259 In this section, the B_s^0 meson reconstruction strategy is presented. The schematic diagram of
 260 the work flow is shown in Fig. 5, starting from muons and tracks to B_s^0 meson candidates.
 261 Muon candidates and tracks are required to pass several quality selection criteria as described
 262 in Section 3.2 and Section 3.3. J/ψ candidates are reconstructed by vertexing muon pairs with
 263 opposite charge, using KinematicConstrainedVertexFitter. ϕ meson candidates are reconstructed in
 264 the same way as J/ψ candidates, i.e., via the vertexing procedure. The B_s^0 candidates are built
 265 by combining the J/ψ candidates with the ϕ candidates. Finally, a kinematic fit to the J/ψ -
 266 K^-K^+ system is performed, forcing the mass of dimuon pair to be equal to the nominal J/ψ
 267 mass based on PDG [12].

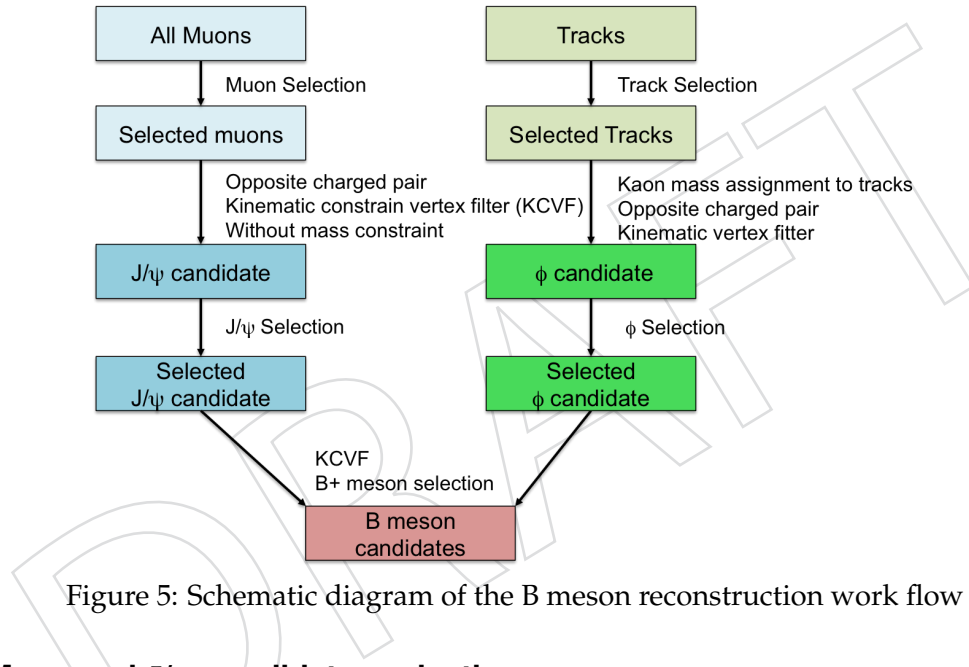


Figure 5: Schematic diagram of the B meson reconstruction work flow

268 3.2 Muon and J/ψ candidates selection

269 The muon candidates are selected according to the *hybrid-soft muon selection*, developed for the
 270 muon analysis on the 2015 5.02 TeV data analysis [13]. It is adapted from the soft-muon ID
 271 developed in the BPH group, with two modifications: a) the purity selection is removed, and
 272 b) the muon is required to be also global. This selection will be updated for the one developed
 273 in 2018. The *hybrid-soft muon selection* includes the following cuts:

- 274 • *isGlobalMuon* and *isTrackerMuon*;
- 275 • *isGoodMuon* > 0;
- 276 • transverse impact parameter $D_{xy} < 0.3$;
- 277 • longitudinal impact parameter $D_z < 20$;
- 278 • $nPixWMea > 0$ and $nTrkWMea > 5$ ($nPixWMea$ and $nTrkWMea$ are the number of
 279 pixel layers and strips, with valid hits, crossed by a single muon track)

Muons are also requested to fulfill the following acceptance selections:

$$\begin{aligned}
 p_T^\mu &> 3.5 \text{ GeV}/c & \text{for } |\eta^\mu| < 1.2 \\
 p_T^\mu &> (5.47 - 1.89 \times |\eta^\mu|) \text{ GeV}/c & \text{for } 1.2 \leq |\eta^\mu| < 2.1 \\
 p_T^\mu &> 1.5 \text{ GeV}/c & \text{for } 2.1 \leq |\eta^\mu| < 2.4
 \end{aligned} \tag{1}$$

280 This single muon selection is chosen in order to guarantee a reasonable (above $\approx 10\%$) recon-
281 struction and trigger efficiency for all the selected muons [13].

282 In addition to single muon quality selections, for a pair of muon candidates, the following
283 selections are performed:

- 284 • two muons have opposite charge sign;
285 • two muons are tracker muons;
286 • dimuon invariant mass be within 0.15 GeV from the PDG J/ψ mass [12];
287 • probability of the two muon tracks to originate from the same decay vertex $> 1\%$.

288 The J/ψ invariant mass, p_T , η , and ϕ , after muon selections applied can be seen in Figure 6, 7,
289 8, 9 and 10,. and all the selection applied in the analysis (even the part described in the next
290 section), observed in data and MC can be seen in Figure 11.

DRAFT

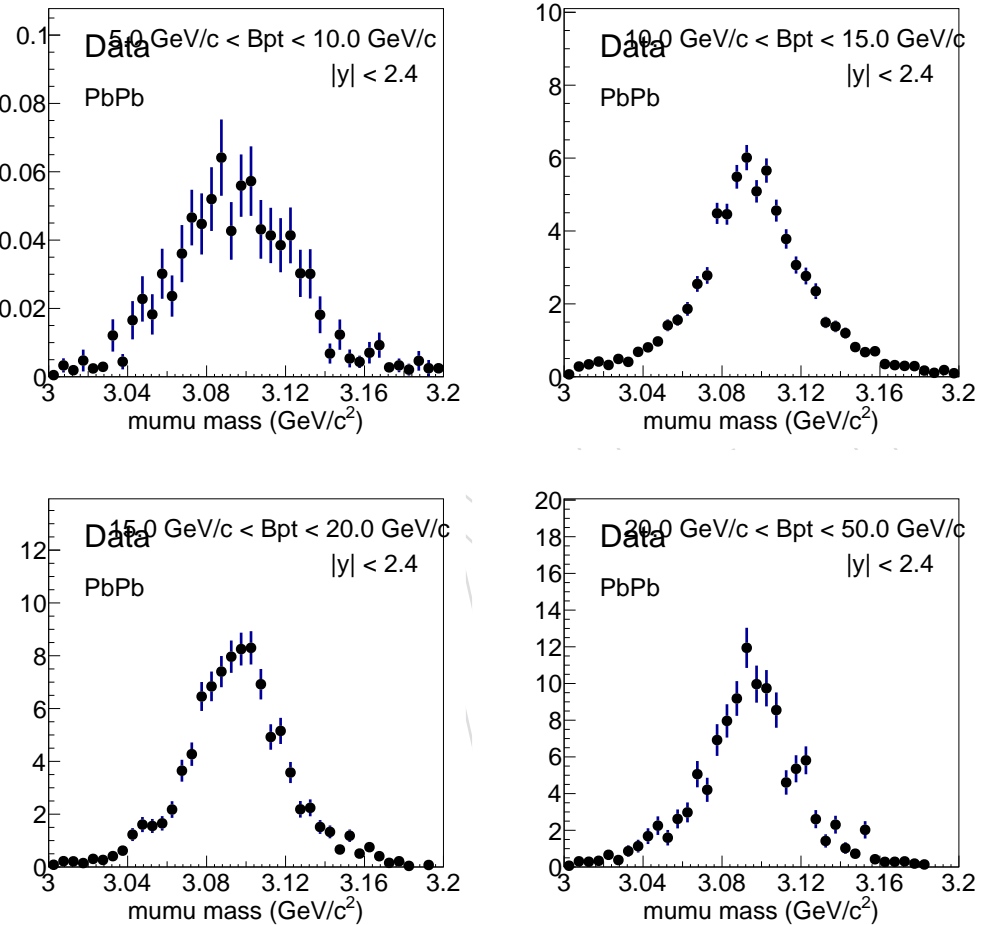


Figure 6: The J/ψ invariant mass distributions in data for $5 \text{ GeV}/c < B_s p_T < 10 \text{ GeV}/c$, $10 \text{ GeV}/c < B_s p_T < 15 \text{ GeV}/c$, $15 \text{ GeV}/c < B_s p_T < 20 \text{ GeV}/c$, $20 \text{ GeV}/c < B_s p_T < 50 \text{ GeV}/c$ before BDT selections are all shown on the plots above from top left to bottom right. We can see very clear peaks for all p_T bins.

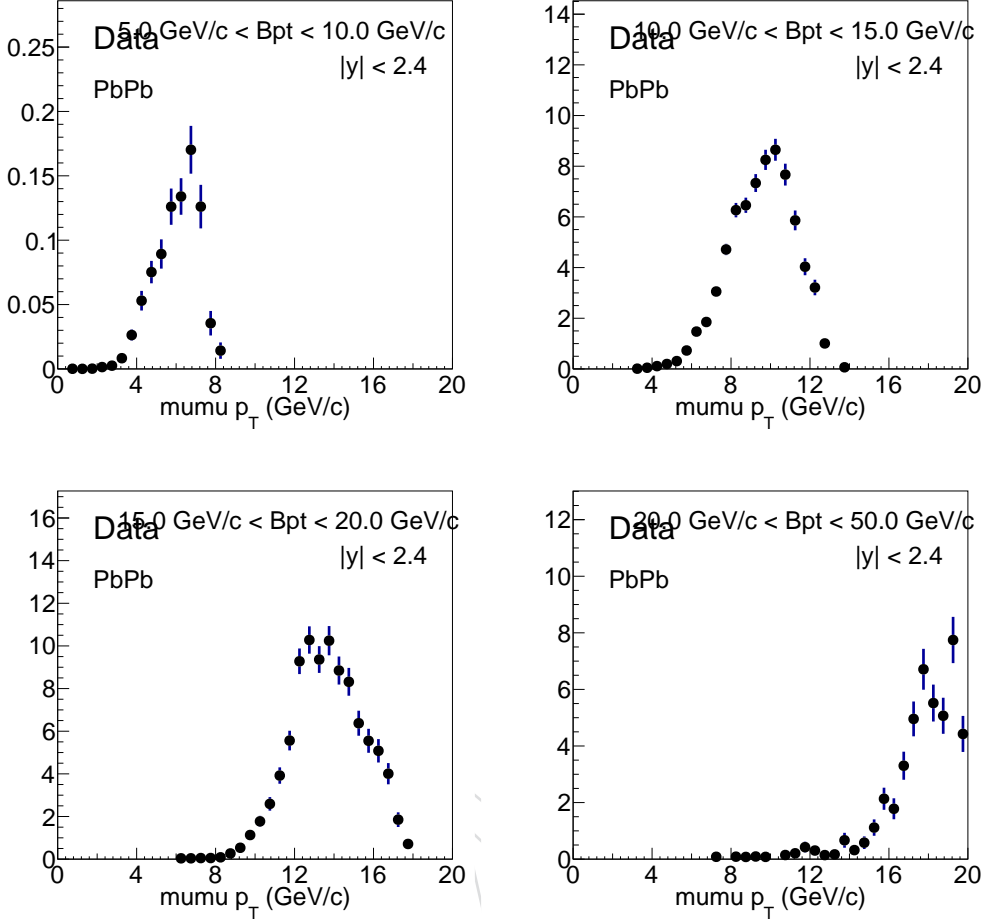


Figure 7: The J/ψ p_T distributions in data for $5 \text{ GeV}/c < B_s p_T < 10 \text{ GeV}/c$, $10 \text{ GeV}/c < B_s p_T < 15 \text{ GeV}/c$, $15 \text{ GeV}/c < B_s p_T < 20 \text{ GeV}/c$, $20 \text{ GeV}/c < B_s p_T < 50 \text{ GeV}/c$ before BDT selections are all shown on the plots above from top left to bottom right. We can see very clear peaks for all p_T bins.

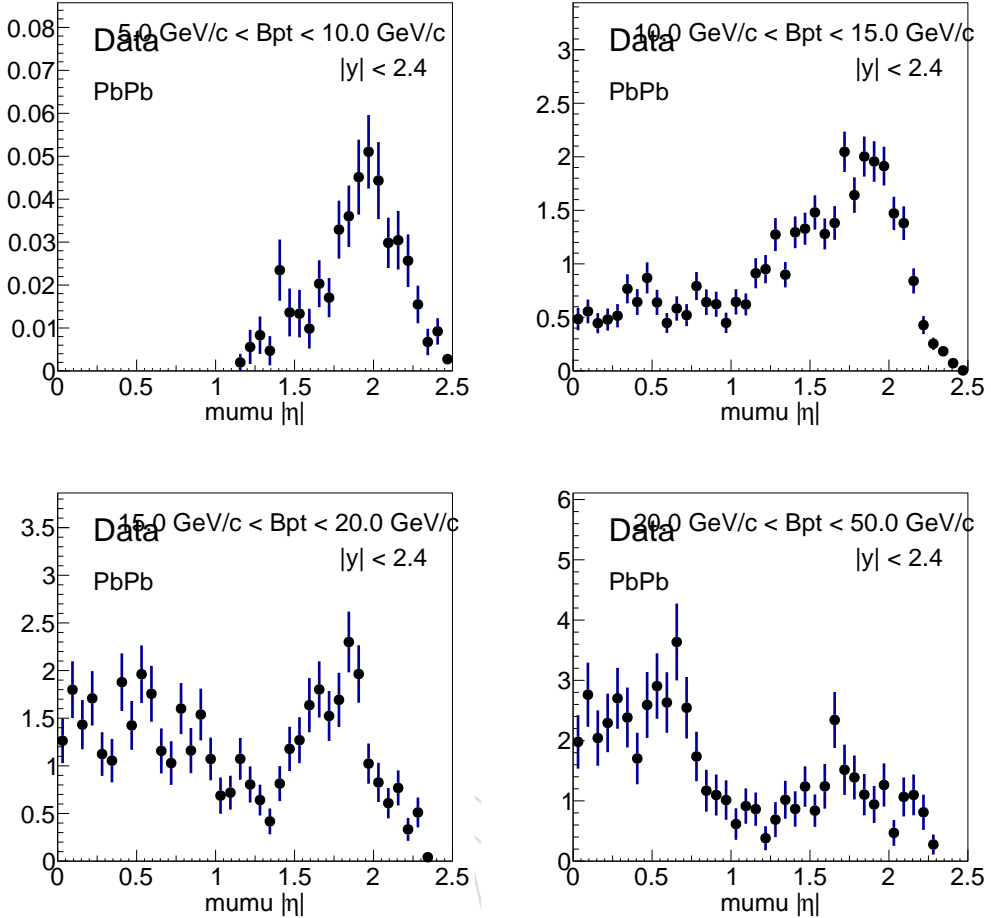


Figure 8: The $J/\psi \eta$ distributions in data for $5 \text{ GeV}/c < B_s p_T < 10 \text{ GeV}/c$, $10 \text{ GeV}/c < B_s p_T < 15 \text{ GeV}/c$, $15 \text{ GeV}/c < B_s p_T < 20 \text{ GeV}/c$, $20 \text{ GeV}/c < B_s p_T < 50 \text{ GeV}/c$ before BDT selections are all shown on the plots above from top left to bottom right. We can see very clear peaks for all p_T bins.

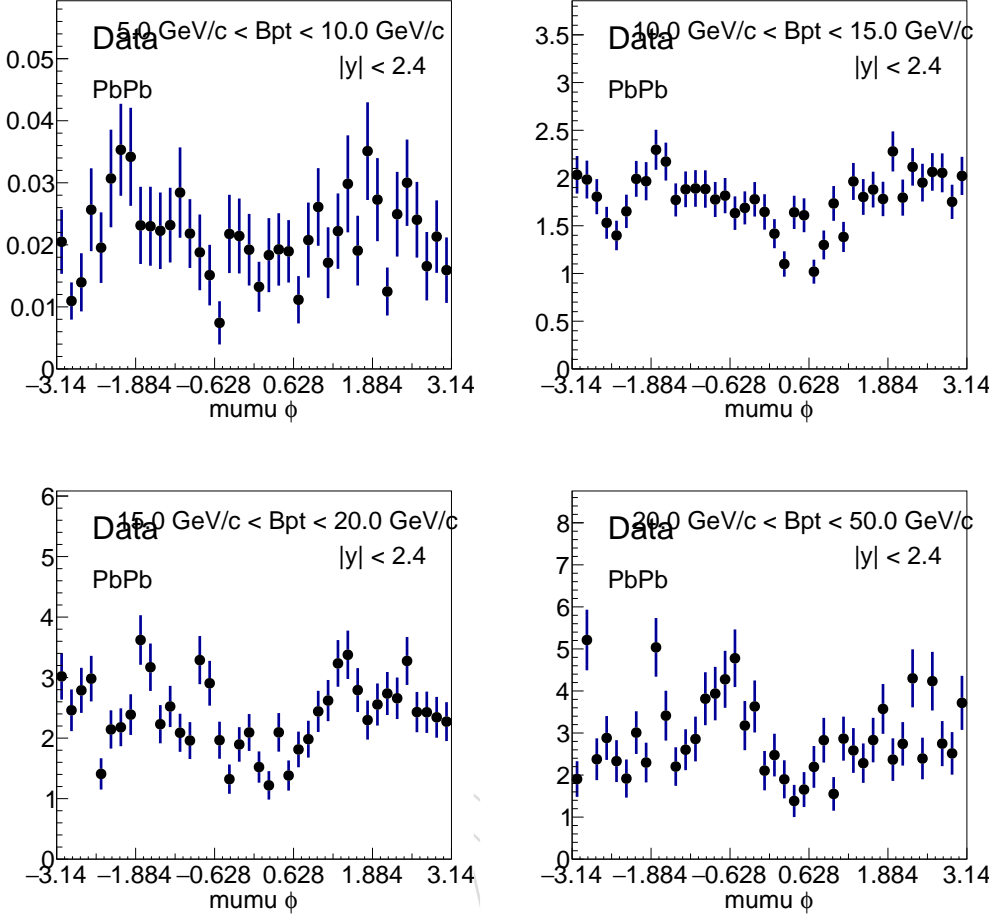


Figure 9: The J/ψ angle distributions in data for $5 \text{ GeV}/c < B_s p_T < 10 \text{ GeV}/c$, $10 \text{ GeV}/c < B_s p_T < 15 \text{ GeV}/c$, $15 \text{ GeV}/c < B_s p_T < 20 \text{ GeV}/c$, $20 \text{ GeV}/c < B_s p_T < 50 \text{ GeV}/c$ before BDT selections are all shown on the plots above from top left to bottom right. We can see very clear peaks for all p_T bins.

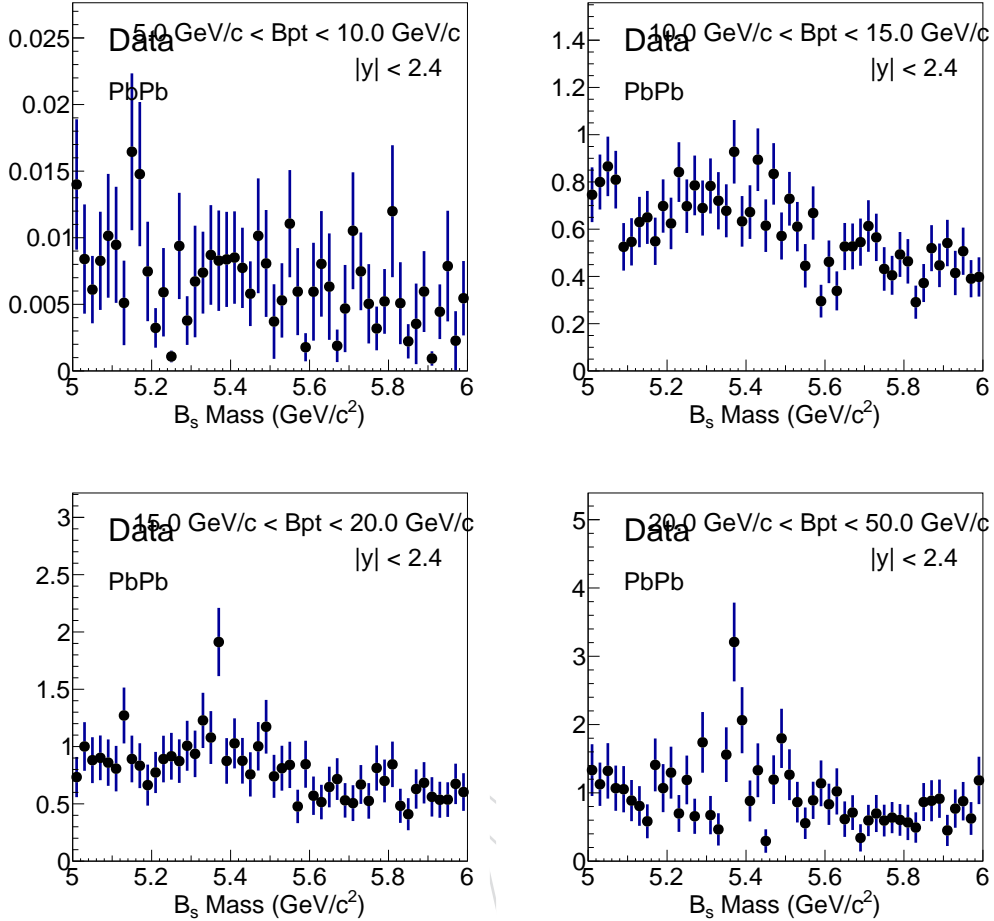


Figure 10: The B_s meson invariant mass distributions in data for $5 \text{ GeV}/c < B_s p_{\text{T}} < 10 \text{ GeV}/c$, $10 \text{ GeV}/c < B_s p_{\text{T}} < 15 \text{ GeV}/c$, $15 \text{ GeV}/c < B_s p_{\text{T}} < 20 \text{ GeV}/c$, $20 \text{ GeV}/c < B_s p_{\text{T}} < 50 \text{ GeV}/c$ before BDT selections are all shown on the plots above from top left to bottom right. We can see very clear peaks for all p_{T} bins.

291 3.3 Track and ϕ candidate selection

292 Tracks were selected according to the following criteria, as recommended by the HIN tracking
 293 group:

- 294 • GeneralTracks passing highPurity selection;
- 295 • $\eta < 2.4$ and $p_T > 1.0 \text{ GeV}/c$;
- 296 • Total hits on the silicon pixel + stripe > 10
- 297 • $\frac{\Delta p_T}{p_T} < 0.1$
- 298 • (track χ^2/ndf)/hits on pixel and stripe > 0.18 .
- 299 • vertex probability > 0.05

300 In addition, it was required that the track pair invariant mass be within $0.015 \text{ GeV}/c^2$ around
 301 the ϕ meson PDG mass [12]. The ϕ invariant mass spectra, after all the selection applied in the
 302 analysis (even the part described in the next section), observed in data and MC can be seen in
 303 Figure 11.

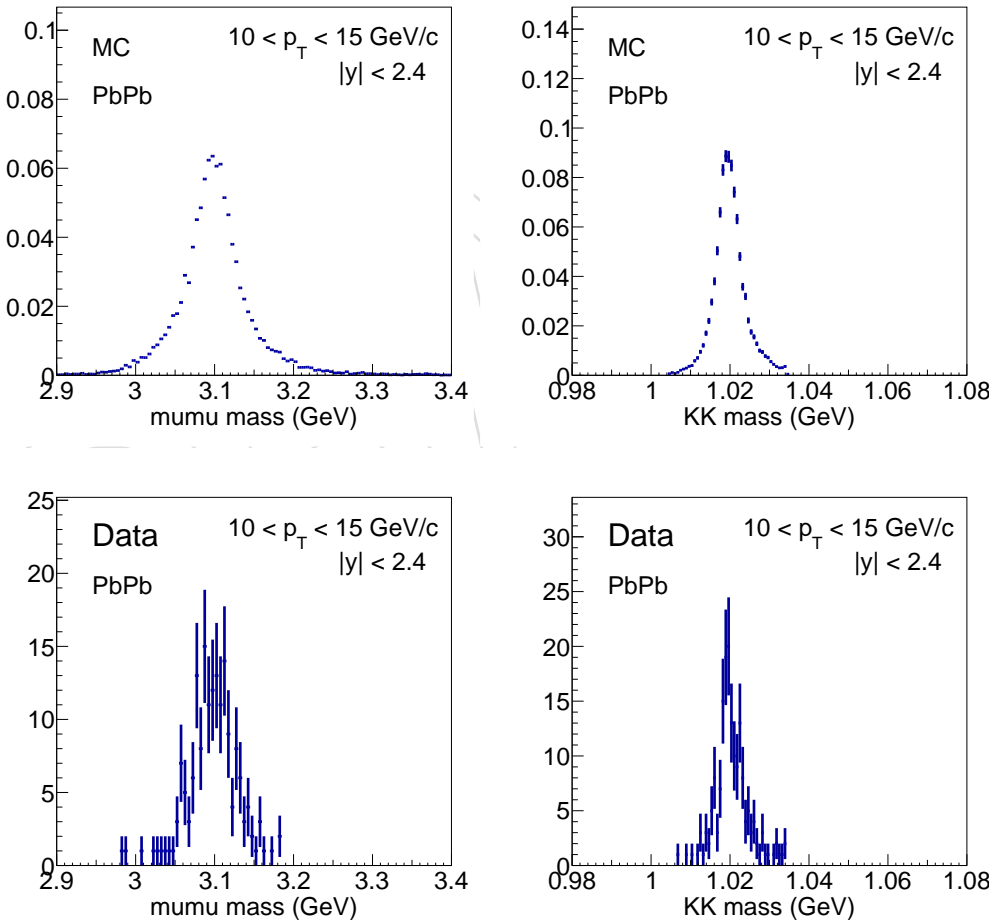


Figure 11: The J/ψ (left) and ϕ (right) meson mass spectra (after all the analysis selections discussed in the next section) for MC (top) and data (low) in PbPb analysis

304 **3.4 ϕ and J/ψ candidates studies vs rapidity**

305 We also carry out the studies of ϕ and J/ψ candidates. We perform Gaussian fits on their
 306 invariant mass distribution and study its width and mass vs rapidity at bins $|y| < 0.5$, $0.5 <$
 307 $|y| < 1.0$, $1.0 < |y| < 1.5$, and $1.5 < |y| < 2.4$ with our preselections and BDT ≥ 0 for all p_T to
 308 make sure that we have more statistics to perform the fits. Our results are shown as follows on
 309 Figure 12 and Figure 13:

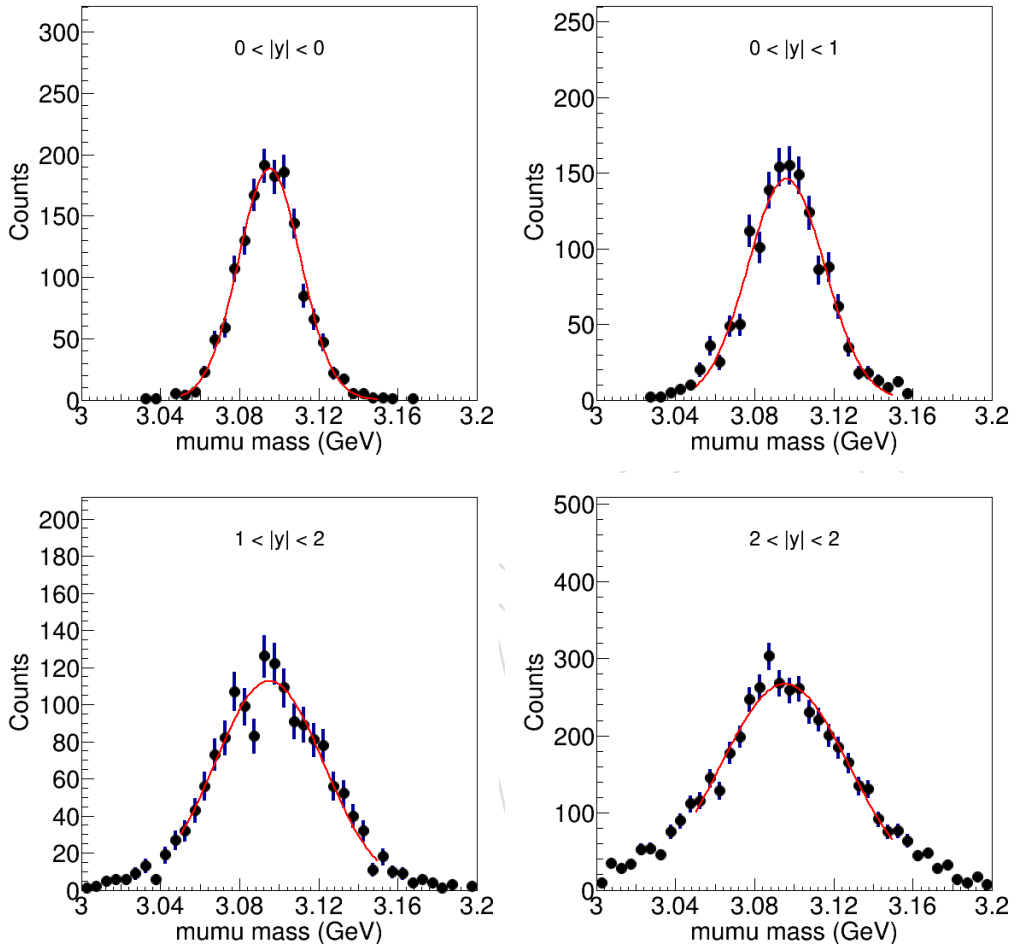


Figure 12: The J/ψ meson mass spectra and the Gaussian fits for $|y| < 0.5$, $0.5 < |y| < 1.0$,
 $1.0 < |y| < 1.5$, and $1.5 < |y| < 2.4$ are show above from top left to bottom right.

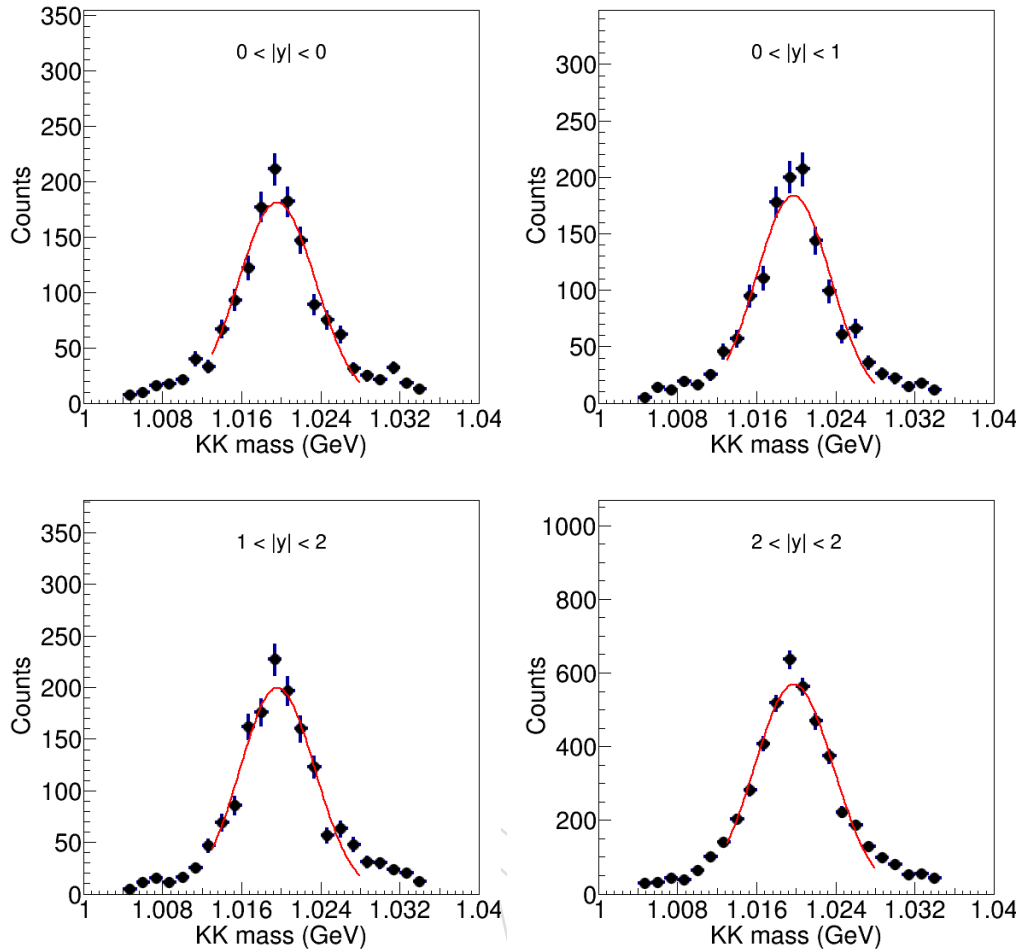


Figure 13: The ϕ meson mass spectra and the Gaussian fits for $|y| < 0.5$, $0.5 < |y| < 1.0$, $1.0 < |y| < 1.5$, and $1.5 < |y| < 2.4$ are shown above from top left to bottom right.

- 310 We extract the width and peak mass of the ϕ and J/ψ mesons and plot them vs the rapidity $|y|$.
 311 Figure 14 below shows our results:

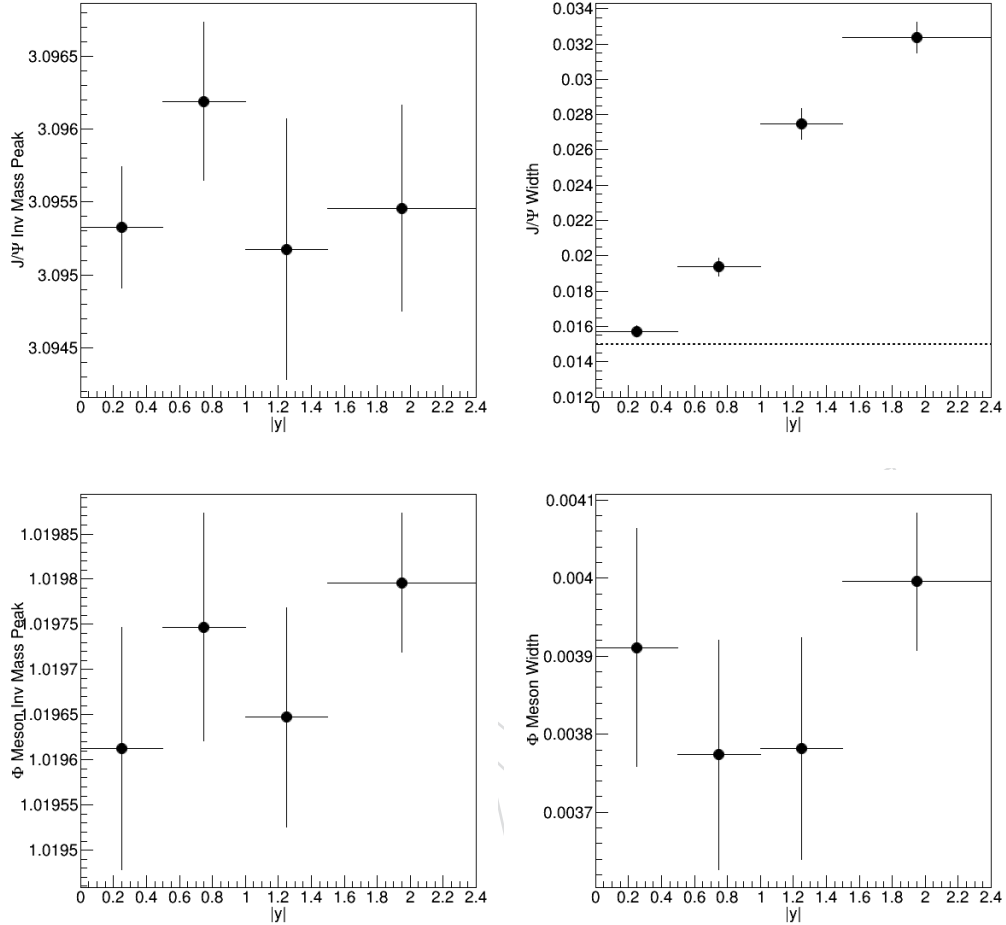


Figure 14: The J/ψ mass (upper left) and width (upper right) and ϕ mass (lower left) and width (lower right) in PbPb data are shown above. The dash line shown for J/ψ width = 0.015 GeV/c is the J/ψ width cut in our analysis.

- ³¹² As we can see from Figure 14, we see no dependence of the ϕ and mass vs $|y|$ within statistical uncertainty. In addition, there is no dependence of ϕ width vs $|y|$ after kinematic fitting.
³¹³ However, we do see that the width of J/ψ increases as $|y|$ increases.

DRAFT

315 4 B_s^0 meson selection optimization

316 Given the high combinatorial background, it is not possible to observe a B_s^0 resonance by just
 317 applying the preselection presented in the previous section. A multivariate analysis (MVA)
 318 was thus conducted in order to device a B_s^0 candidate selection to separate signal B_s^0 from back-
 319 ground and reconstruct an observable resonance in the mass spectrum in the data. The fitting
 320 performance is further related to both the amount of signal and background presented in the
 321 mass spectrum. By a MVA analysis, one can then find the proper selection criteria which is
 322 optimized for this purpose. Several variables related to tracks (K^+ and K^- track) and B_s^0
 323 decay topology were applied in order to reduce the combinatorial background that arises from
 324 random combination of tracks and muons.

325 4.1 Cut optimization

326 The goal of the optimization procedure is to maximize the statistical significance of the signal
 327 while keeping reasonably high signal efficiency. The optimal cut which minimizes the back-
 328 ground efficiency for a given signal efficiency is obtained by the TMVA (Toolkit for Multivari-
 329 ate Data Analysis with ROOT) [14]. BDT (Boosted Decision Trees) method is chosen for this
 330 analysis which was shown to have the highest signal to background efficiency by comparing
 331 the ROC curve with other method including Multilayer perceptron (MLP) method and Artifi-
 332 cial neural network (ANN). The reconstructed candidates matched to generated signal in MC
 333 sample are used as signal during training, while the reconstructed candidates in the sideband
 334 ($0.2 \text{ GeV}/c^2 < |M_{B_s} - M_{B_s}^{PDG}| < 0.3 \text{ GeV}/c^2$ for $5 \text{ GeV}/c < p_T < 10 \text{ GeV}/c$, $10 \text{ GeV}/c < p_T <$
 335 $15 \text{ GeV}/c$, and $15 \text{ GeV}/c < p_T < 20 \text{ GeV}/c$ and $0.18 \text{ GeV}/c^2 < |M_{B_s} - M_{B_s}^{PDG}| < 0.36 \text{ GeV}/c^2$
 336 for $20 \text{ GeV}/c < p_T < 50 \text{ GeV}/c$) of data sample are used as background. The choice of the side-
 337 band range is driven by the statistics of the background. At $20 \text{ GeV}/c < p_T < 50 \text{ GeV}/c$, the
 338 background level is relatively low and thus we choose a wider sideband in our TMVA training.

339 There are twelve variables considered in the BDT training.

- 340 • track p_T (Btrk1Pt and Btrk2Pt): the transverse momentum of the K^+ and K^- track
- 341 • track Dxy significance (Trk1DCAxy and Trk2DCAxy): the transverse distance be-
342 tween the K^+ and K^- track to primary vertex, divided by its error
- 343 • track Dz significance (Trk1DCAz and Trk2DCAz): the longitudinal distance between
344 the K^+ and K^- track to primary vertex, divided by its error
- 345 • track pair invariant mass (MassDis): the absolute difference between the invariant
346 mass of the track pair (which form ϕ meson candidate) and PDG mass of a ϕ meson
- 347 • normalized SV PV distance (dls): the distance between primary and B_s^0 vertex nor-
348 malized by its uncertainty
- 349 • α_B angle (Balpah): the angle between B_s^0 meson displacement and B_s^0 meson momen-
350 tum
- 351 • cosine θ_B angle (cos(Bdtheta)): the cosine value of the angle between B_s^0 meson dis-
352 placement and B_s^0 meson momentum in the transverse direction
- 353 • vertex fitting probability (Bchi2cl): the χ^2 value of the vertex fitting

354 We look at the invariant mass distribution with the preselection only. Figure 15 shows the B_s
 355 invariant mass at 4 p_T bins: [5, 10], [10, 15], [15, 20] and [20, 50] as well as 3 centrality bins [0,
 356 90], [0, 30], and [30, 90] with only preselections applied.

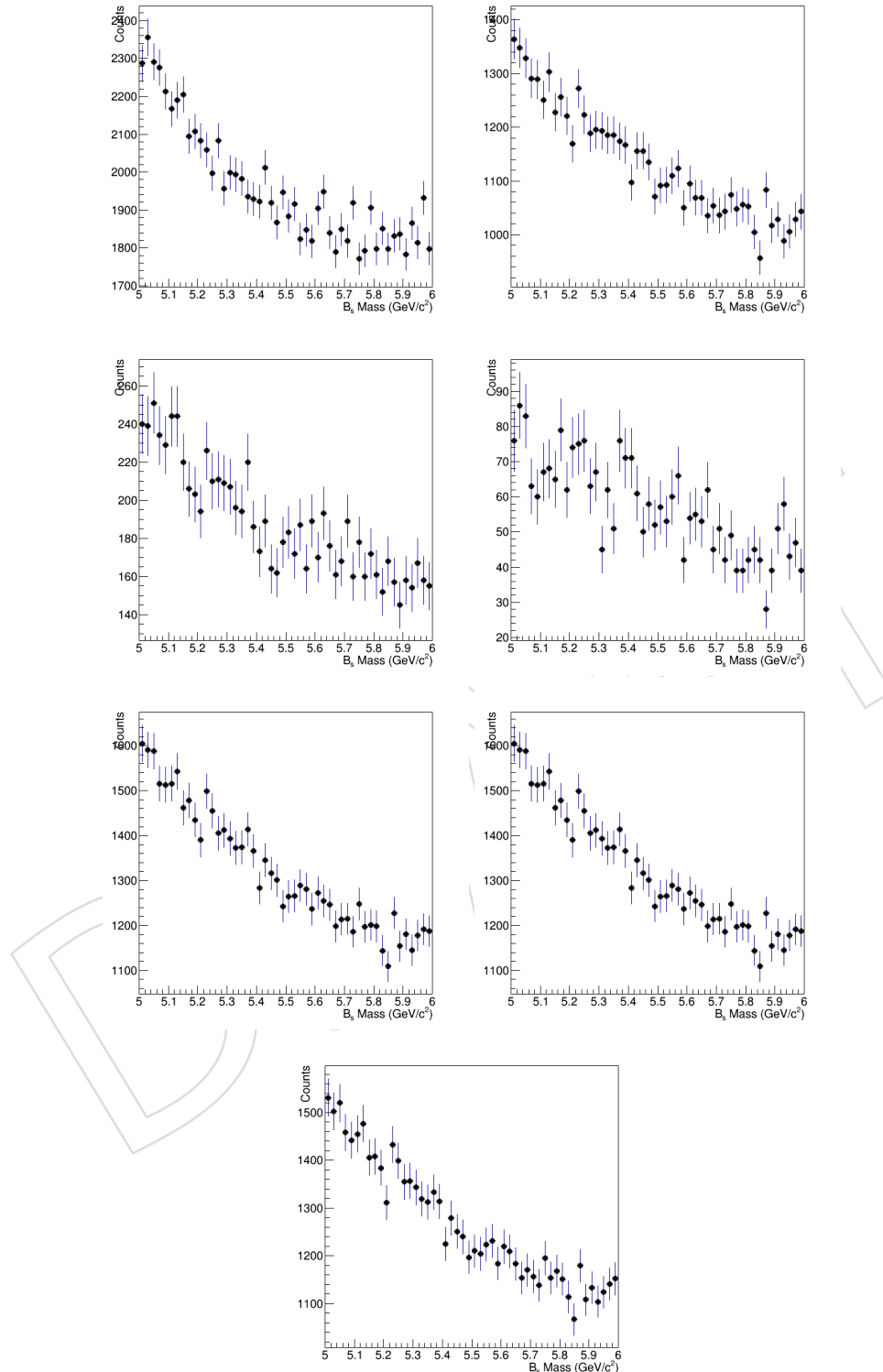


Figure 15: The B_s^0 invariant mass distributions for p_T at 5 - 10, 10 - 15, 15 - 20, and 20 - 50 GeV/c at centrality 0 - 90% as well as 0 - 90%, 0 - 30%, and 30 - 90% for p_T at 10 - 50 GeV/c .

- 357 We can see that there is no B_s signal from its invariant mass distribution when we only apply
358 the preselections. We need to optimally select its decay kinematic variables in order to find B_s^0
359 signal. We propose to use TMVA BDT machine learning algorithm to search for B_s^0 signal.
- 360 The TMVA optimization procedure is performed separately and independently for 4 p_T bins:
361 [5, 10], [10, 15], [15, 20] and [20, 50].
- 362 Fig. 16 and Fig. 17 shows some of the correlation matrices between the variables used in MVA
363 training. The correlation matrices relating to the other two B_s^0 p_T bins, can be found in Ap-
364 pendix A.

The watermark consists of the word "DRAFT" in a bold, sans-serif font. It is rendered in a light gray color and is rotated approximately 45 degrees clockwise. The letters are slightly overlapping, creating a sense of depth. The watermark is centered on the page and spans most of the vertical space.

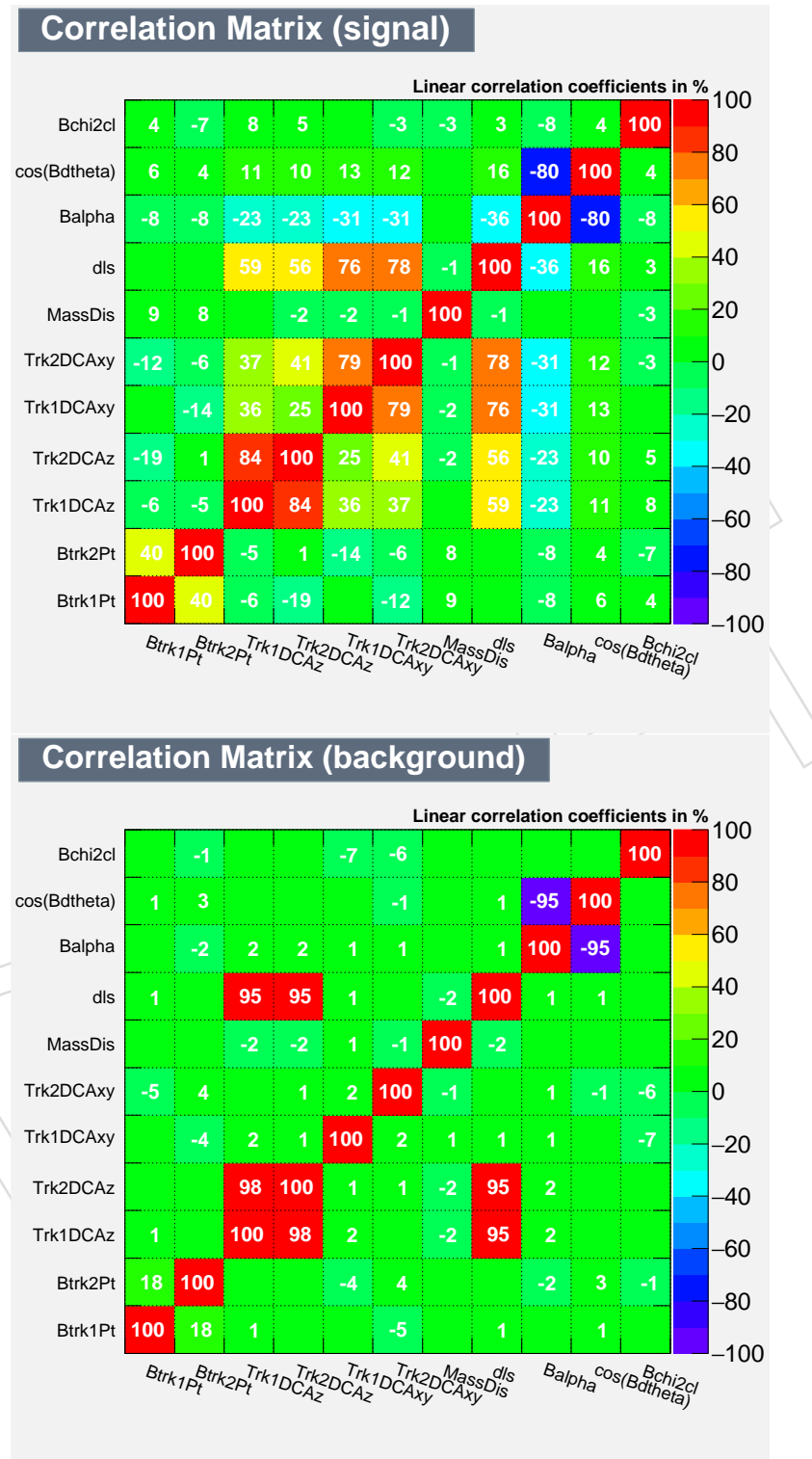


Figure 16: Correlation matrix between the variables used in MVA training for signal and background $B_s^0 p_T$ 5 to 10 GeV/c

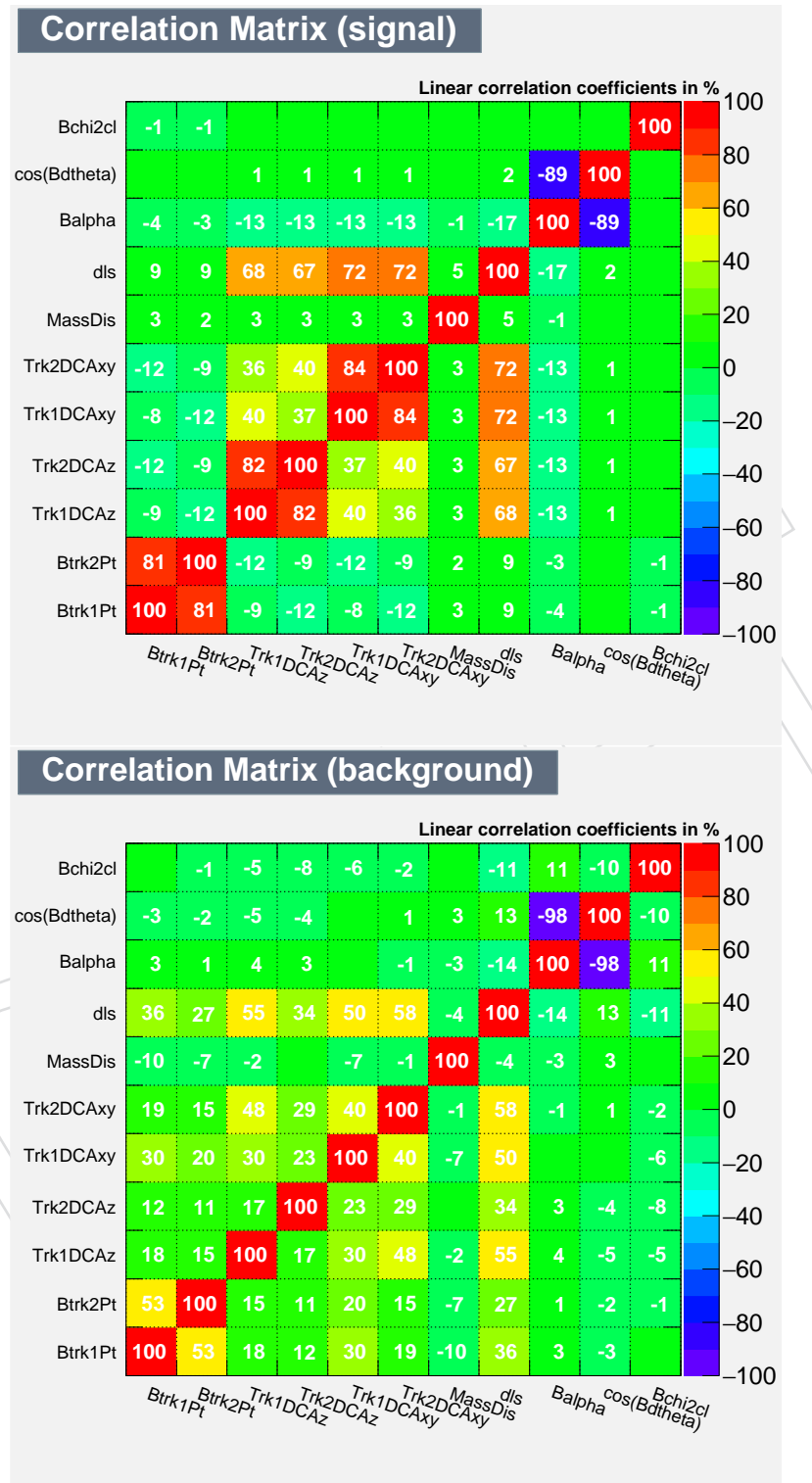


Figure 17: Correlation matrix between the variables used in MVA training for signal and background $B_s^0 p_T$ 20 to 50 GeV/c

365 The optimal cut values are defined as the value that maximize the statistical significance $S / \sqrt{S + B}$.
 366 S is the number of signal in signal region after applying optimal cuts, while B is the num-
 367 ber of background in signal region after applying optimal cuts. Signal region is defined as
 368 $|M_{B_s} - M_{B_s}^{PDG}| < 0.08 \text{ GeV}/c^2$.

- 369 • $S = S' \times (\text{signal optimal cut efficiency})$, where S' is the number of signal in signal
 370 region before applying optimal cuts.
- 371 • $B = B' \times (\text{background optimal cut efficiency})$, where B' is the number of background
 372 in signal region before applying optimal cuts.

373 S' is calculated by the expected number of signal from FONLL calculation multiplied by pre-
 374 filters efficiency and acceptance from MC. B is estimated by a linear interpolation using the
 375 number of candidates in sideband.

376 Fig.18 and Fig.19 show the input variables distribution in two of the MVA trainings. The other
 377 two can be found in Appendix A. Fig. 20 and Fig. 21 show $S / \sqrt{S + B}$ as a function of BDT,
 378 as well as the signal efficiencies and the BDT distributions for both signal and background, for
 379 the lowest and highest $B_s^0 p_T$ bins. Again, the distributions for the $B_s^0 p_T$ bins of [10, 15] and [15,
 380 20] GeV/c can be found in Appendix A.

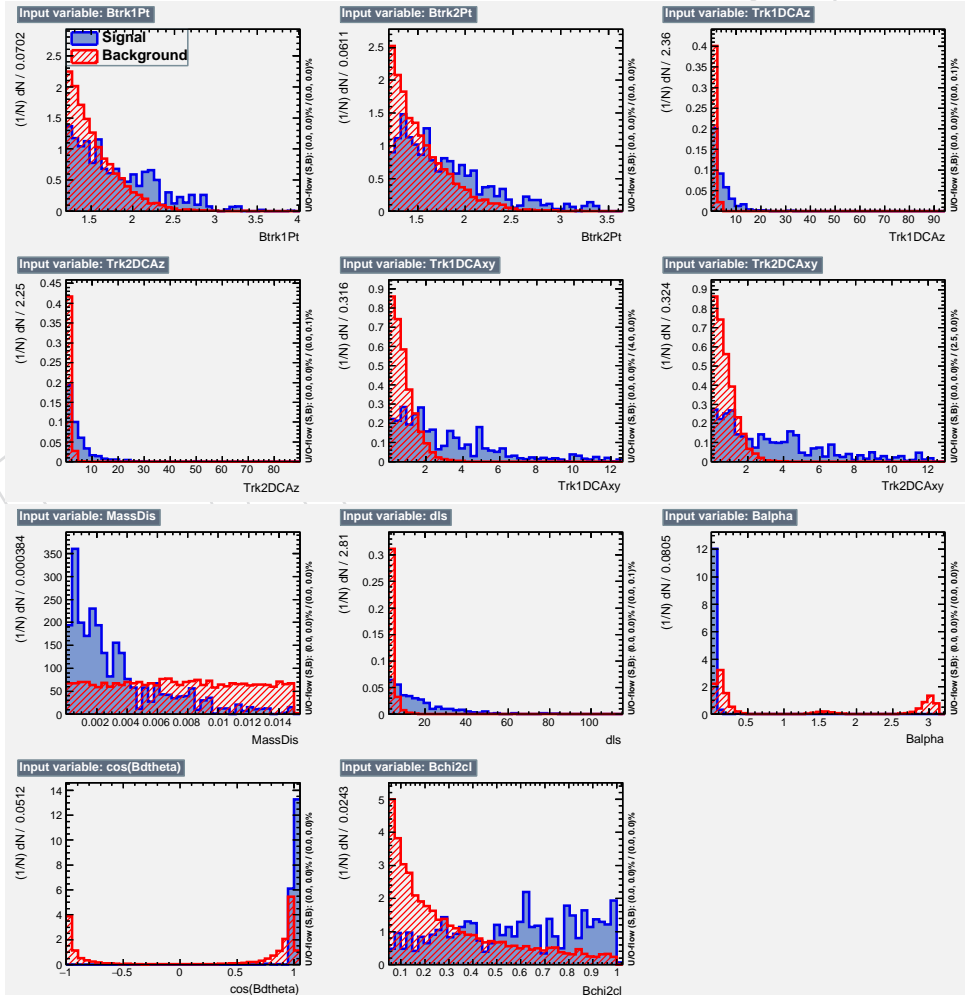


Figure 18: Input variables distributions for training used in PbPb $B_s^0 p_T$ 5-10 GeV/c .

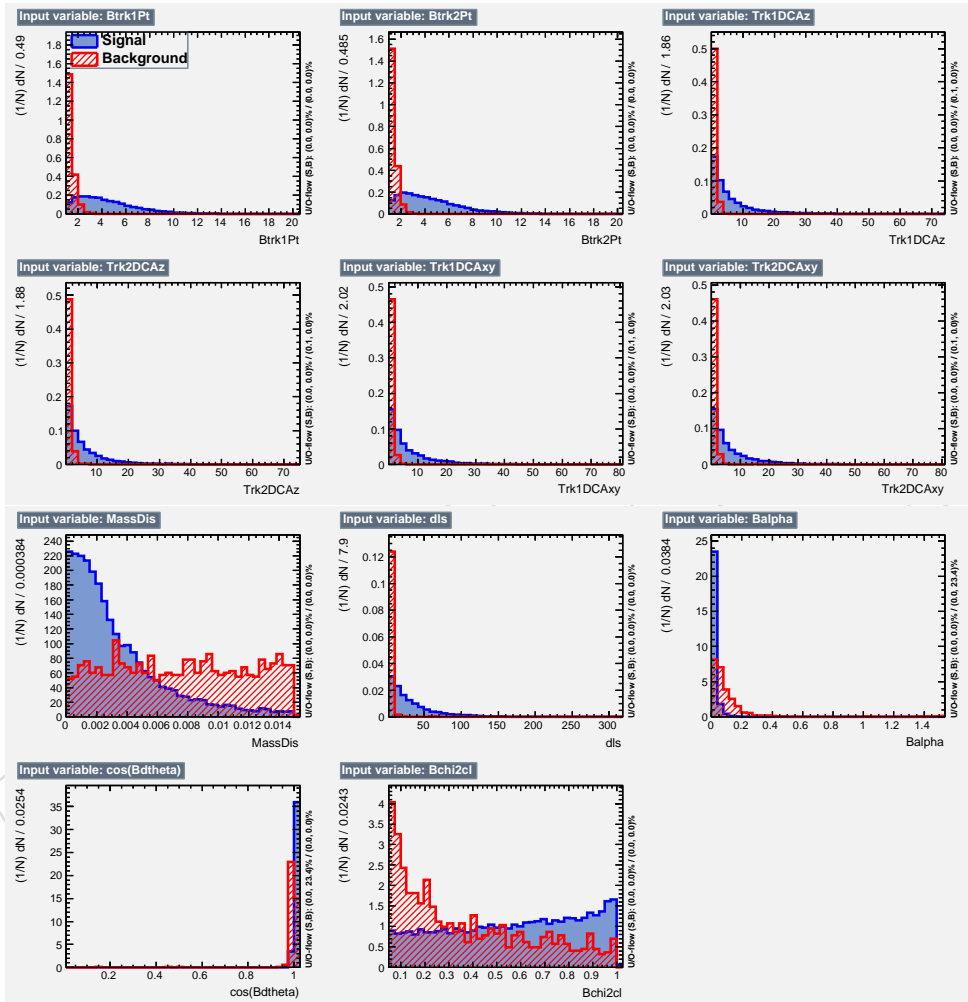


Figure 19: Input variables distributions for training used in PbPb B_s^0 p_T 20-50 GeV/c.

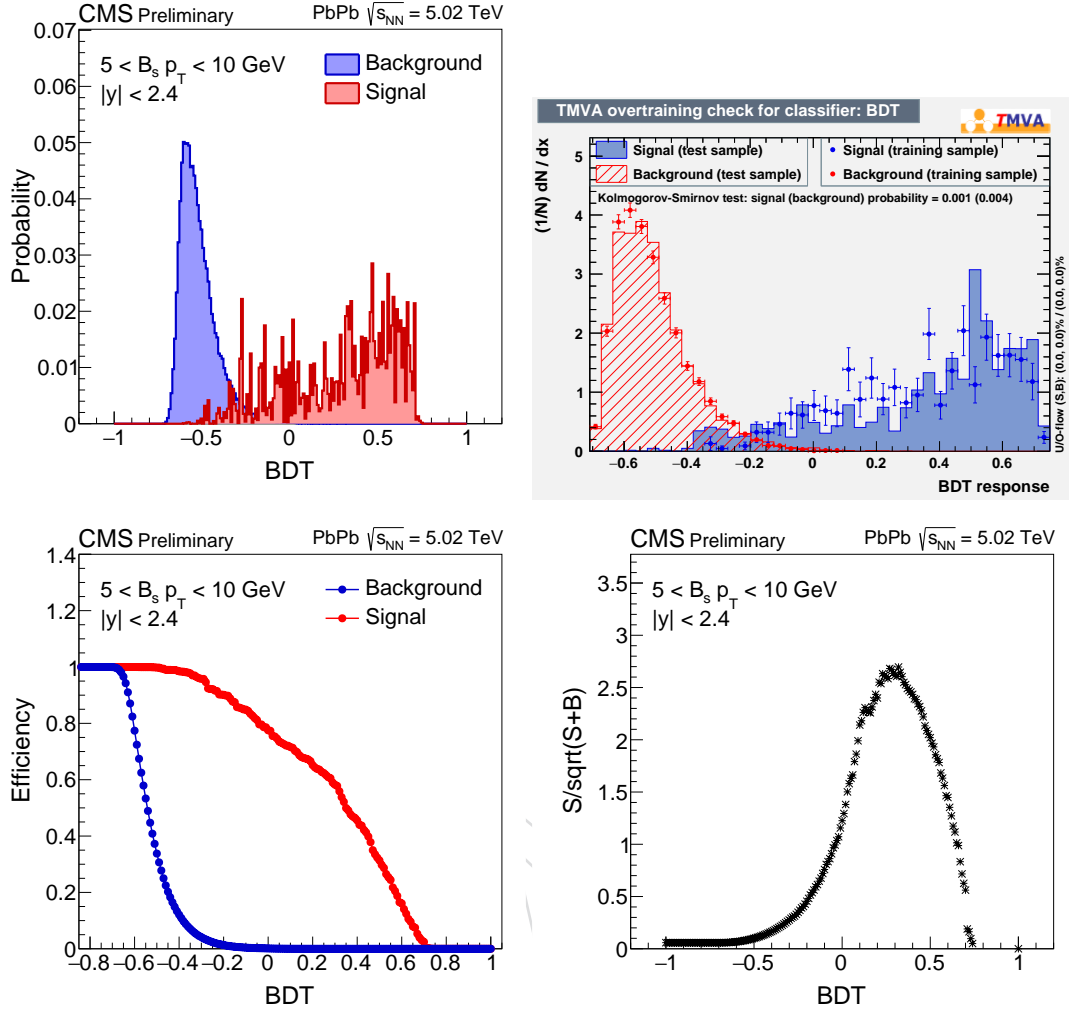


Figure 20: BDT distribution of signal and background from training sample (upper left) and the over train test (upper right). Efficiency as a function of BDT for training and testing samples (lower left). $S/\sqrt{S+B}$ as a function of BDT for 5-10 GeV/c in PbPb collisions (lower right).

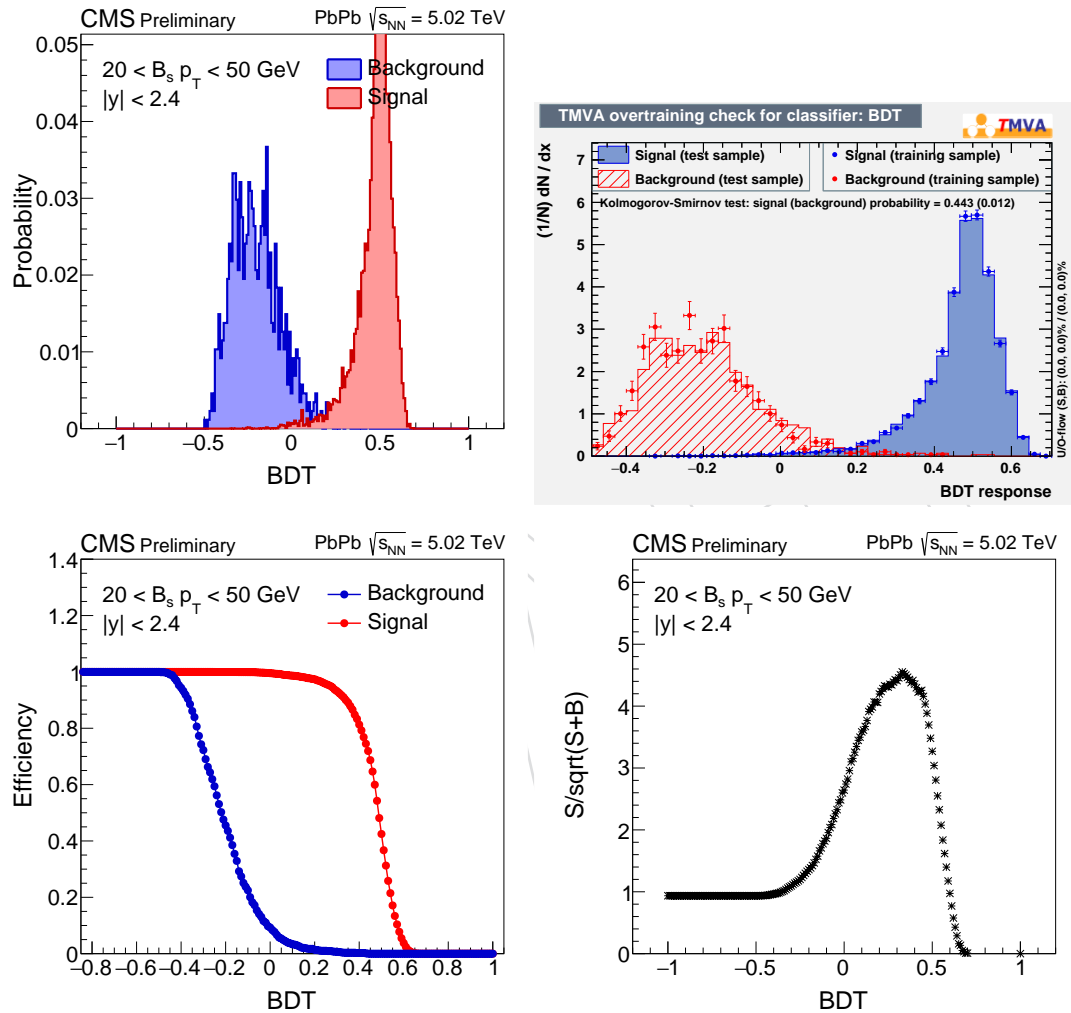


Figure 21: BDT distribution of signal and background from training sample (upper left) and the over train test (upper right). Efficiency as a function of BDT for training and testing samples (lower left). $S/\sqrt{S+B}$ as a function of BDT for $20-50 \text{ GeV}/c$ in PbPb collisions (lower right).

³⁸¹ Tab. 3 is a summary of final selection criteria.

p_T (GeV/c)	5-10	10-15	15-20	20-50
BDT	> 0.32	0.29	0.35	0.33

Table 3: Selection criteria in PbPb analysis

³⁸² In addition, we have also tested the other expressions of the signal significance that replace the
³⁸³ \sqrt{N} uncertainties with the asymmetric Poisson uncertainties. According to <https://twiki.cern.ch/twiki/bin/viewauth/CMS/PoissonErrorBars>, the definition of new signifi-
³⁸⁴ cance is as follows:
³⁸⁵

$$Z = \frac{S}{\sqrt{GR(\frac{\alpha}{2}, S + B, 1)}} \quad (2)$$

³⁸⁶ "GR" stands for the gamma distribution quantile function. $\alpha = 1 - 0.6827 = 0.3173$. 0.6827
³⁸⁷ is 1 - sigma integral of the Gaussian region. S stands for signal. B stands for background.
³⁸⁸ Again, we maximize the new definition of significance Z to find the optimal working point.
³⁸⁹ The significance value vs BDT cut for the new definition is shown as follows on figure 22

³⁹⁰ The working points for the new definition of significance are show as follows on Table 4

p_T (GeV/c)	5-10	10-15	15-20	20-50
BDT	> 0.32	0.26	0.35	0.33

Table 4: Selection criteria in PbPb analysis

³⁹¹ We can see that the working point are very identical, except at $10 \text{ GeV}/c < p_T < 15 \text{ GeV}/c$
³⁹² where the working point change from $0.29 \rightarrow 0.26$, to the working point with our statistical
³⁹³ significance $\frac{S}{\sqrt{S+B}}$. Therefore, we still choose the working point derived from the statistical
³⁹⁴ significance $\frac{S}{\sqrt{S+B}}$.

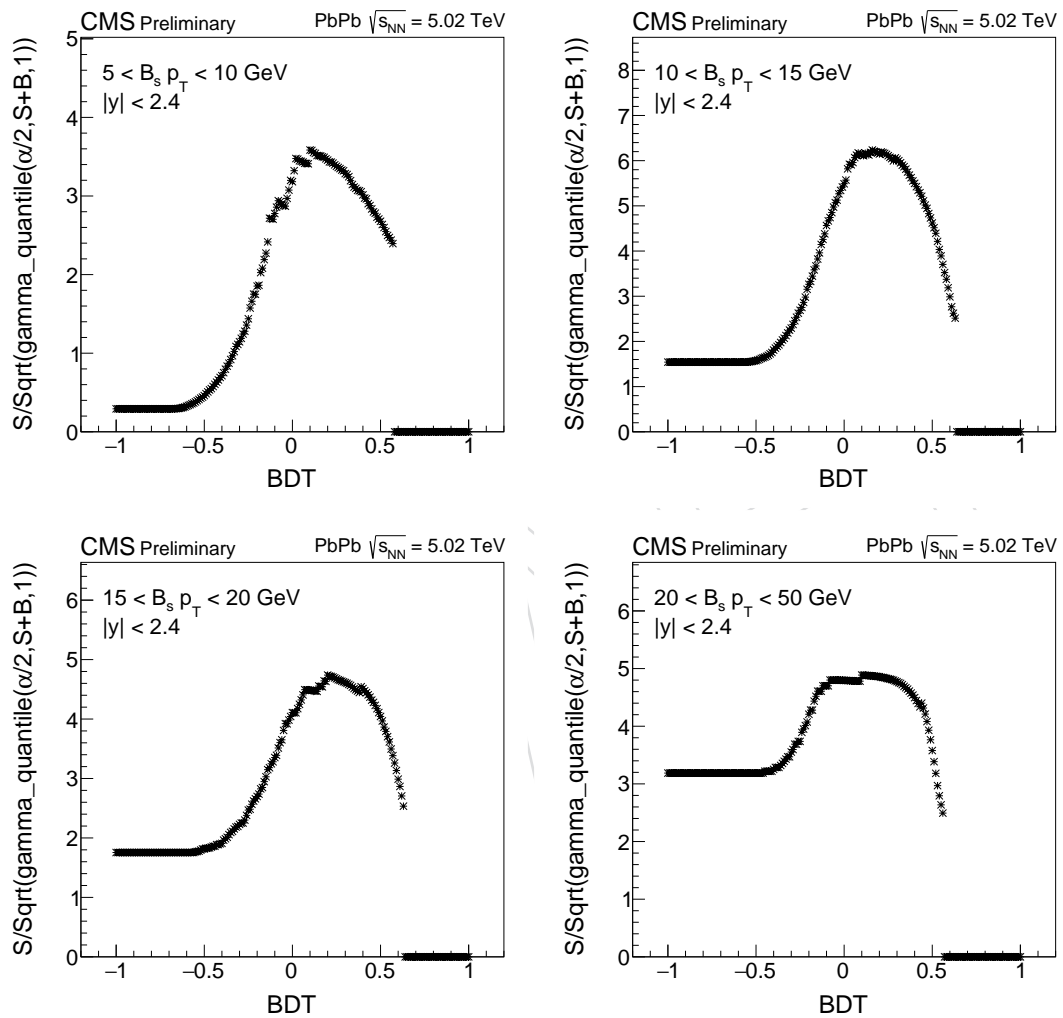


Figure 22: The new definition of significance based on the model $Z = \frac{S}{\sqrt{\text{GR}(\frac{\alpha}{2}, S+B, 1)}}$ for all four p_T bins are shown above.

395 5 B_s^0 candidate properties comparison between data and MC

396 Before validating the MC-Data consistency, we first show the BDT and training variables are all
397 uncorrelated to the invariant mass of the B_s^0 meson. The correlation matrices for the inclusive 7
398 - 50 GeV/c p_T bin in data and MC are shown as follows:

DRAFT

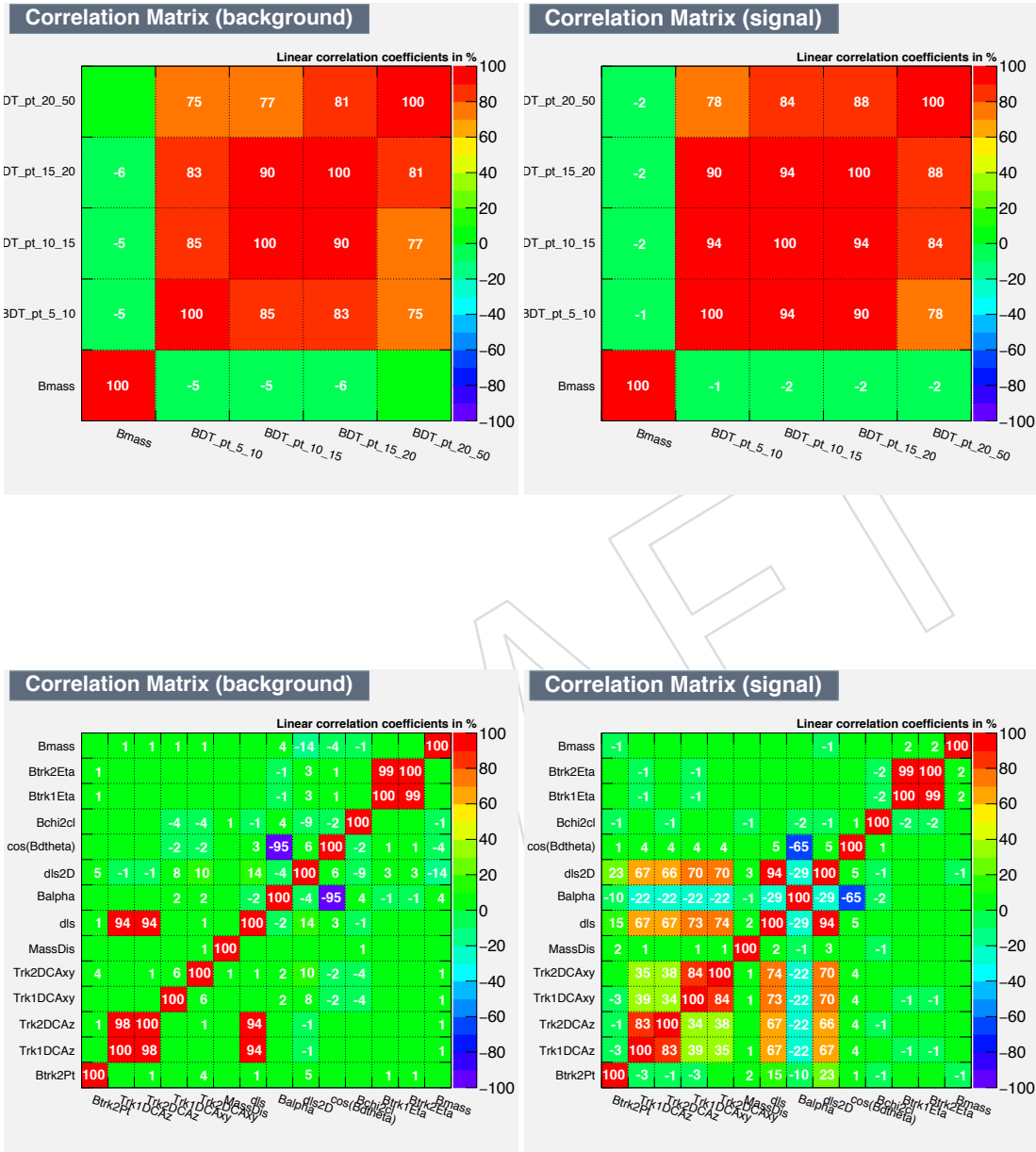


Figure 23: B_s^0 the correlations matrices of the BDT variables (Up) and training variables (Down) to the invariant mass of B_s^0 Bmass in data (left) and MC (right) for p_T at 7 - 50 GeV/c are shown above

399 We can see that the BDT and training variables are essentially uncorrelated to the Bmass. This
 400 allows us to use sPLOT to validate the data and MC. To validate the signal MC samples being
 401 used against the data, we employ the sPlot method [15] to extract the signal distribution. The
 402 procedure was already documented in the sPLOT techniques for B mesons AN [16].
 403 We present the results of the sideband subtraction and the comparison with signal MC for the
 404 BDT distributions in all four p_T bins in Fig. 24.

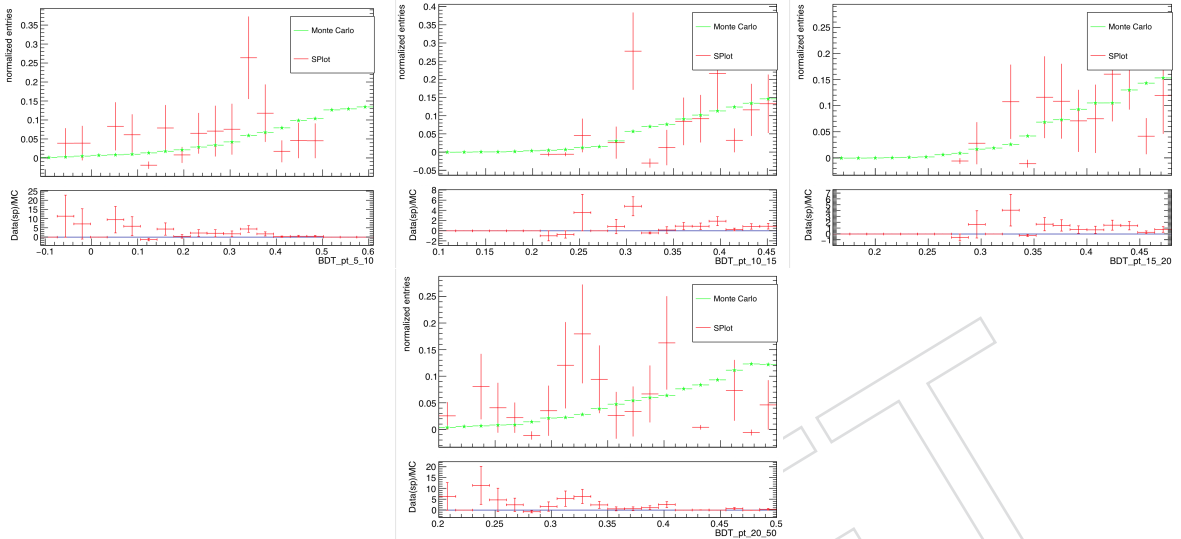


Figure 24: Comparison of the BDT distribution between data and MC. From left to right, the comparisons refer to B_s^0 p_T bins of [5, 10], [10, 15], [15, 20] and [20, 50] GeV/ c .

405 From Figure 24 above, we can see that the B_s^0 statistics is very low and the fluctuation of Data-
406 to-MC is large but overall near unity. We will use B^+ kinematic variables instead to compare
407 the data and MC and quote their deviation as the systematic uncertainties for selections.

DRAFT

408 6 Signal Extraction

409 Raw yields are extracted through extended unbinned maximum likelihood fits to the invariant
 410 mass of reconstructed B_s^0 meson candidates, performed using the RooFit package. The fit is first
 411 performed to the MC invariant mass distribution of genuine B_s^0 signal, and the signal shape is
 412 extracted to then fit the data mass spectrum. The chosen PDF (probability density function),
 413 describing the signal component was a sum of two gaussian functions, that better modelled
 414 the signal shape of the MC simulations. Then, the fit is performed to the reconstructed B_s^0
 415 invariant mass distribution in data, fixing the values of the widths and the relative proportion
 416 between the two gaussians to the value obtained from the MC fit. The mean was let as a floating
 417 parameter. To describe the combinatorial background produced by the random combination of
 418 a J/ψ candidate with tracks that are not coming from the same B_s^0 decay, an exponential function
 419 was chosen.

420 The generic event likelihood in data, is described by

$$\mathcal{L}(m; N_S) = N_S \cdot (\alpha G(m; M, \sigma_1) + (1 - \alpha)G(m; M, \sigma_2)) + N_B \cdot E(m; \lambda_m), \quad (3)$$

421 where m is the candidate mass (input); M and σ_i are the signal mass mean and widths (res-
 422 olution); G and E denote respectively Gaussian and Exponential functions, normalized in the
 423 fitting mass window; N_S denotes the signal yield (the parameter of interest), N_B is the back-
 424 ground yield, while α and λ_m are nuisance parameters (describing the signal fractions and
 425 exponential decay slope). As mentioned already, α , σ_1 and σ_2 are fixed from the MC fit.

426 Unlike the B^+ analysis [11], non-prompt J/ψ background component is not considered in the
 427 mass fitting in this analysis, since a tight selection on the mass pf the ϕ candidate make it negli-
 428 gible. Studies done using non-prompt J/ψ MC samples show that the contribution is negligible
 429 comparing to the B_s^0 signal after applying the optimal cut.

430 Relevant detailed information can be found in App. C.

The invariant mass range considered for the fits goes from 5 to 6 GeV/c^2 . The fits were per-
 formed in different p_T and centrality bins, and can be found in Figures 25 and 27, each one
 displaying underneath its respective pull distribution. The fits to the MC signal invariant
 mass distribution can be also seen in Figures 26 and 28. The parameters displayed in each
 case are the ones let free during the fitting. The fits obtained for the entire B_s^0 invariant mass
 distributions for both data and MC, can be found in Figures 29 and 30. For each fit the signifi-
 cance and χ^2_{nDof} are also shown. The significance (Z) is calculated through a likelihood method,
 following the formula:

$$Z = \sqrt{2 \log \frac{L_{S+B}}{L_B}}$$

431 where L_{S+B} is the likelihood of each fit, and L_B is the likelihood when the number of signal
 432 events is fixed to 0.

433 The signal yields were also obtained for different p_T bins within centrality bins. Those results
 434 are documented in Appendix B.

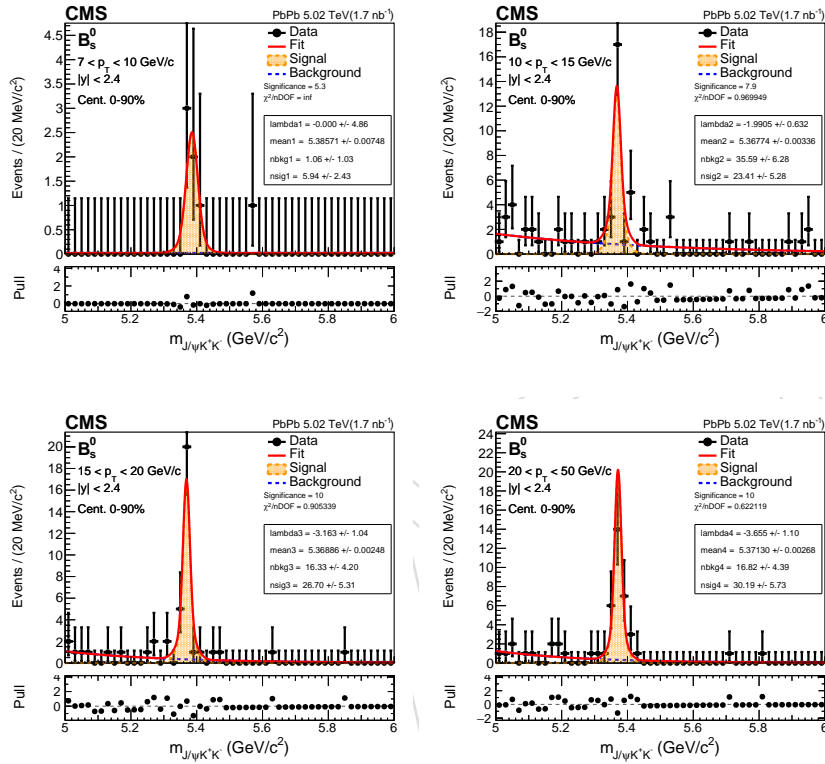


Figure 25: Invariant mass distribution and the corresponding pull between data and fit of B_s^0 candidates obtained in PbPb collisions in the p_T interval between 7 to 10 GeV/c , 10 to 15 GeV/c , 15 to 20 GeV/c and 20 to 50 GeV/c . The parameters presented are the ones allowed to float during the fit: lambda is the parameter from the exponential background function, nback the number of background events, mean is the mean for both gaussians, and nsig is the number of signal events.

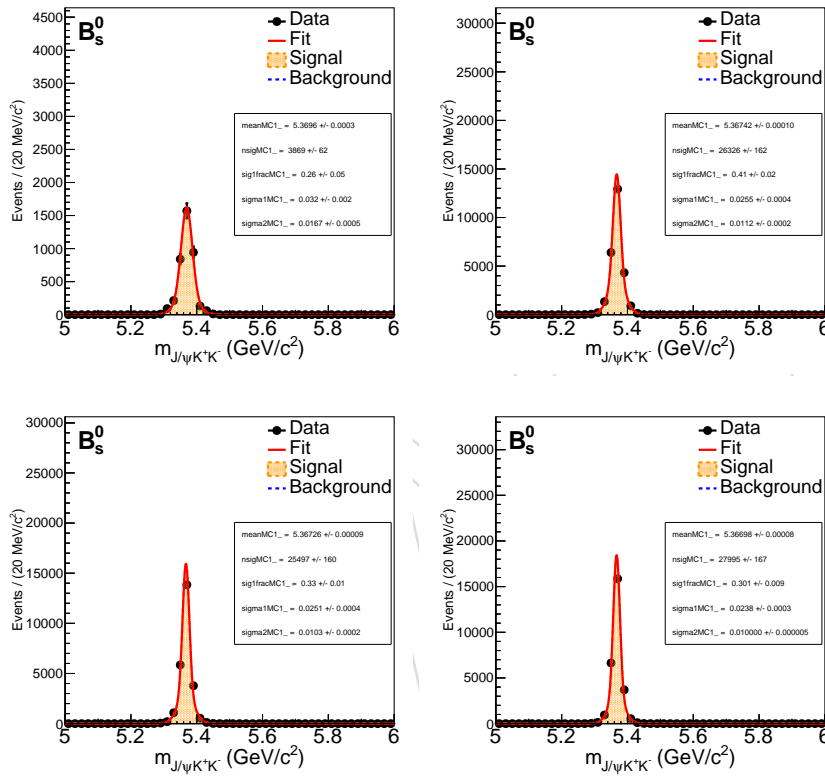


Figure 26: B_s^0 invariant mass distributions in MC simulations and the respective fit obtained in PbPb collisions in the p_T interval between 7 to 10 GeV/ c , 10 to 15 GeV/ c , 15 to 20 GeV/ c and 20 to 50 GeV/ c . The parameters presented are the ones allowed to float during the fit: meanMC is the mean for both gaussians, nsigMC is the number of signal events, sig1fracMC is the relative proportion of the gaussians and sigma1MC and sigma2MC are the widths of the gaussians.

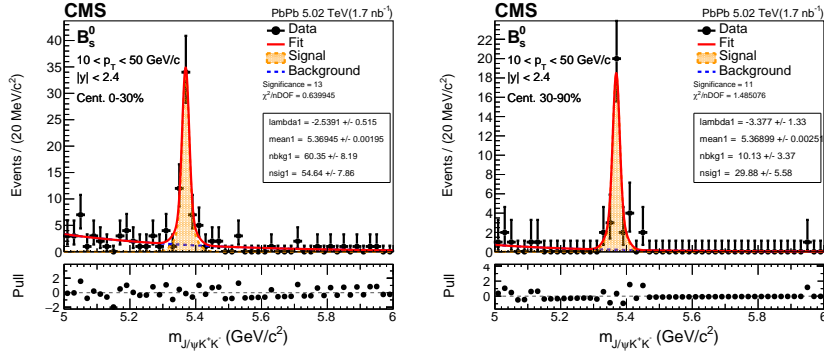


Figure 27: Invariant mass distribution and the corresponding pull between data and fit of B_s^0 candidates obtained in PbPb collisions in the centrality interval between 0% to 30% and 30 % to 90 %. The parameters presented are the ones allowed to float during the fit: λ is the parameter from the exponential background function, $n\text{back}$ the number of background events, mean is the mean for both gaussians, and $n\text{sig}$ is the number of signal events.

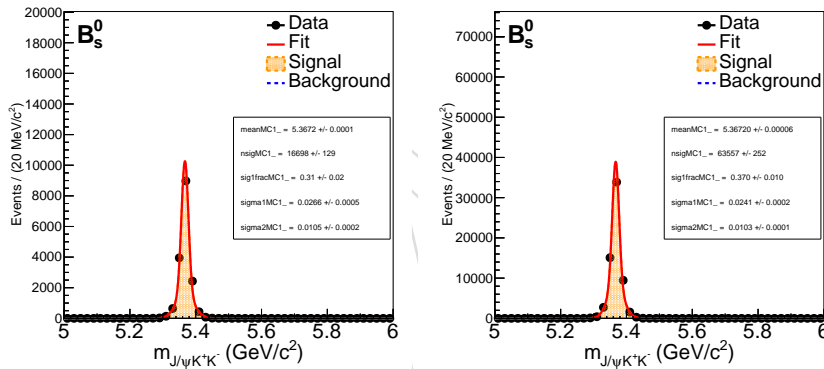


Figure 28: B_s^0 invariant mass distributions in MC simulations and the respective fit obtained in PbPb collisions in the centrality ranges of 0% to 30% and 30 % to 90 %. The parameters presented are the ones allowed to float during the fit: meanMC is the mean for both gaussians, $n\text{sigMC}$ is the number of signal events, sig1fracMC is the relative proportion of the gaussians and $\sigma\text{igma1MC}$ and $\sigma\text{igma2MC}$ are the widths of the gaussians.

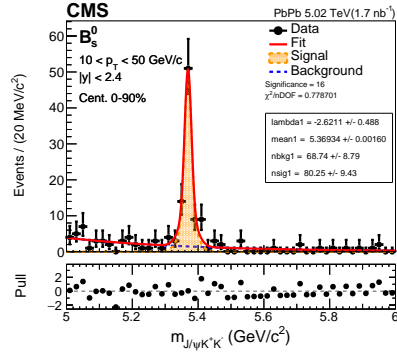


Figure 29: Invariant mass distribution and the corresponding pull between data and fit of B_s^0 candidates obtained in PbPb collisions in the centrality interval between 0 to 90 %.

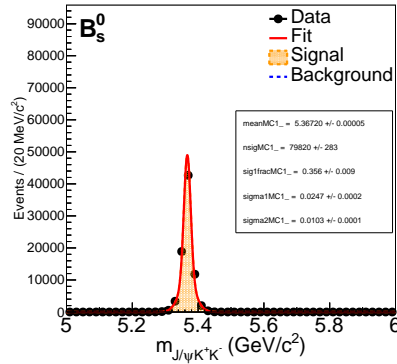


Figure 30: B_s^0 invariant mass distributions in MC simulations and the respective fit obtained in PbPb collisions in the centrality interval between 0 to 90 %.

⁴³⁵ We have also performed a significance scan on the signal yield parameter and made the plot.
⁴³⁶ Figure 31 and 32 show the p_T and centrality bins results respectfully.

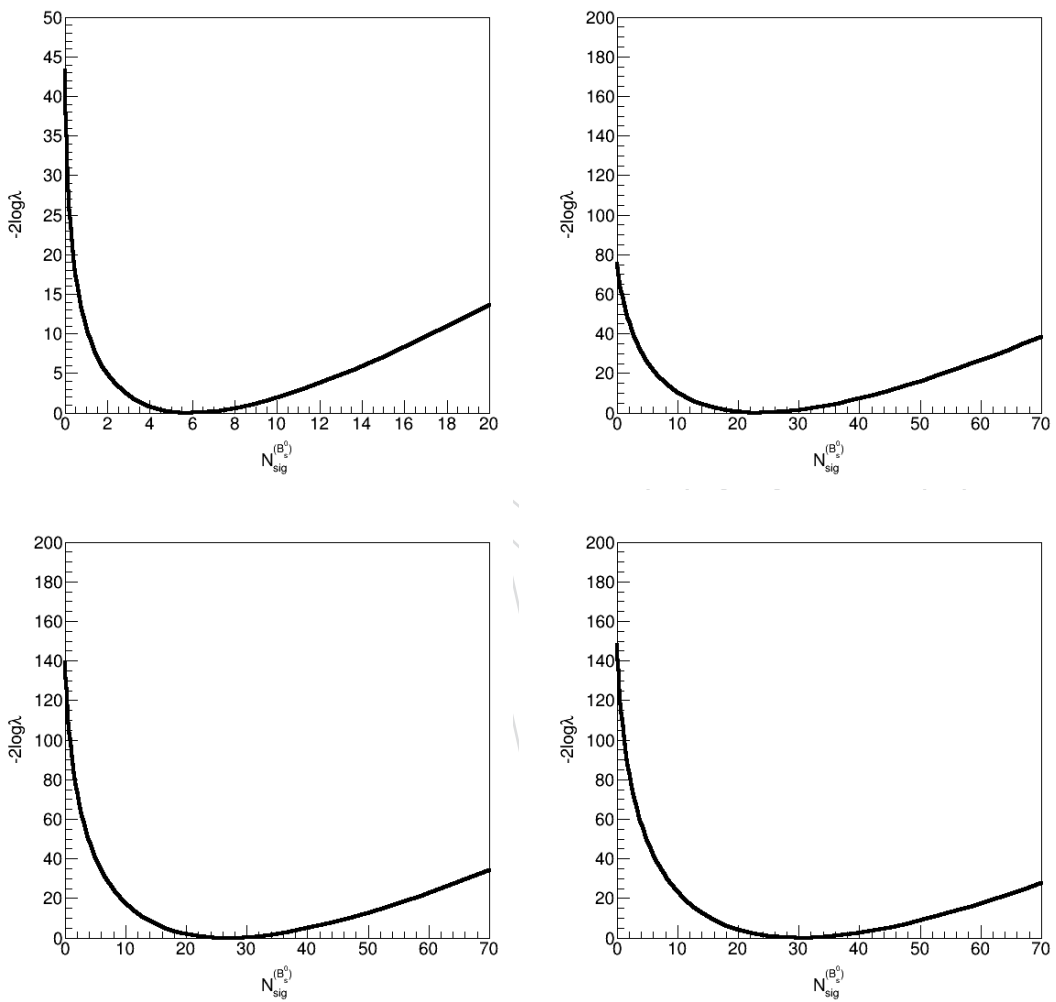


Figure 31: The significance vs signal yield for p_T bins at 7 - 10, 10 - 15, 15 - 20, and 20 - 50 GeV/c in 0 - 90% centrality are shown above

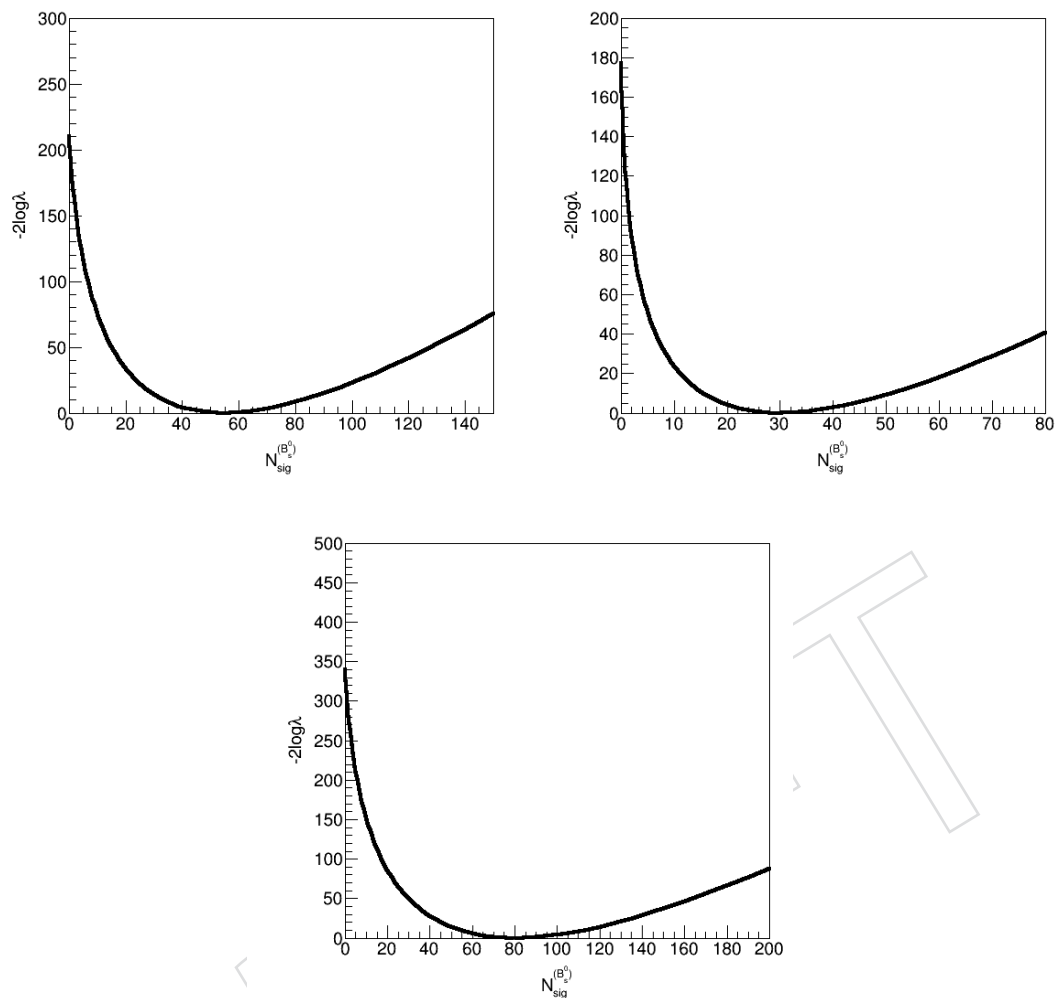


Figure 32: The significance vs signal yield for centrality bins in 0 - 30%, 30% - 90% 0 - 90% for p_T in 10 - 50 GeV/c are shown above

⁴³⁷ We can see that all significance have higher than 5 statistical significance at 0 signal, which
⁴³⁸ suggests that we have discovered B_s^0 particles in all p_T and centrality bins presented in our
⁴³⁹ analysis.

⁴⁴⁰ Tables 5 and 6 summarise the obtained significance and extracted yield values in differential
⁴⁴¹ p_T and centrality bins. Tables 7 and 8 summarize the signal model parameters for each fit.

Table 5: Summary table of Significance and fitted yield for each B_s^0 p_T bins

	(7,10)	(10,15)	(15,20)	(20,50)
Significance	5.3	7.9	10	10
Yield	5.94 ± 2.43	23.41 ± 5.28	26.70 ± 5.31	30.19 ± 5.73

Table 6: Summary table of Significance and fitted yield for each centrality bin

	0 - 30%	30 - 90%	0 - 90%
Significance	14	11	16
Yield	54.64 ± 7.86	29.88 ± 5.58	80.25 ± 9.43

Table 7: Summary table of fitted mean, number of signal and number of backgrounds used for unbinned fit for each p_T bin

	(7,10)	(10,20)	(15,20)	(20,50)
Mean	5.386 ± 0.007	5.368 ± 0.003	5.369 ± 0.002	5.371 ± 0.003
Number of signal	5.94 ± 2.43	23.41 ± 5.28	26.70 ± 5.31	30.19 ± 5.73
Number of background	1.06 ± 1.03	35.59 ± 6.28	16.33 ± 4.20	16.82 ± 4.39

⁴⁴² We also make the comparison between the symmetric raw yield error and their asymmetric
⁴⁴³ upper and lower yield error using the RooFit framework on the unbinned fit. The table is
⁴⁴⁴ shown below in Table 9:

⁴⁴⁵ We have also perform the closure test for the fits using toy MC studies and fit the pull distribution
⁴⁴⁶ of the toy MC with a Guassian functions to check if they will return us zero mean and unit
⁴⁴⁷ pull. The details of tour studies are shown on Section 8.1 “Closure Test on the Raw Yield Fits”.

Table 8: Summary table of fitted mean, number of signal and number of backgrounds used for unbinned fit for each centrality bin

	0 - 30%	30 - 90%	0 - 90%
Mean	5.369 ± 0.002	5.370 ± 0.003	5.369 ± 0.002
Number of signal	54.64 ± 7.86	29.88 ± 5.58	80.25 ± 9.43
Number of background	60.35 ± 8.19	10.13 ± 3.37	68.74 ± 8.79

Table 9: The comparison between RooFit and unbinned fit framework.

Centrality	p_T (GeV/c)	Raw Yield Error	Raw Yield Error Up	Raw Yield Error Down
0 - 90%	7 - 10	2.681	3.040	2.391
0 - 90%	10 - 15	5.656	6.005	5.327
0 - 90%	15 - 20	5.310	5.464	4.997
0 - 90%	20 - 50	5.813	6.153	5.498
0 - 30%	10 - 50	8.185	8.541	7.846
30 - 90%	10 - 50	5.583	5.923	5.271
0 - 90%	10 - 50	9.704	9.364	10.06

448 7 Acceptance and Efficiency

449 7.1 Overview

450 To obtain the B_s^0 corrected yield, we need to correct its acceptance and selection efficiency. We
 451 calculate the following quantities:

452 We count the total number of generated B meson candidates reweighted by the centrality, PVz,
 453 and \hat{p}_T as NBGen within the given fiducial region as follows.

454 B meson rapidity $|y| < 2.4$ for $p_T > 10 \text{ GeV}/c$ and $1.5 < |y| < 2.4$ for $5 < p_T < 10 \text{ GeV}/c$

455 Next, we count the number of generated B meson candidates passing the follow selection

456 Again the fiducial region: B meson rapidity $|y| < 2.4$ for $p_T > 10 \text{ GeV}/c$ and $1.5 < |y| < 2.4$
 457 for $5 < p_T < 10 \text{ GeV}/c$

458 Muon track selections:

$$\begin{aligned} p_T^\mu &> 3.5 \text{ GeV}/c \\ p_T^\mu &> (5.47 - 1.89 \times |\eta^\mu|) \text{ GeV}/c \\ p_T^\mu &> 1.5 \text{ GeV}/c \end{aligned} \quad \begin{aligned} \text{for } |\eta^\mu| &< 1.2 \\ \text{for } 1.2 \leq |\eta^\mu| &< 2.1 \\ \text{for } 2.1 \leq |\eta^\mu| &< 2.4 \end{aligned} \quad (4)$$

Kaon tracks selections:

$$\begin{aligned} p_T^K &> 0.9 \text{ GeV}/c \\ |\eta^K| &< 2.4 \end{aligned} \quad (5)$$

459 to the generated B meson candidates denoted as NPassAcc.

460 Finally, we apply all the selections on the gen matched reconstructed B mesons. We count the
 461 reconstructed B meson candidates passing the selections mentioned in Section 3.2 “Muon and
 462 J/ψ candidates selections” and the optimal BDT selections in Table 3 in Section 4.1 and denote
 463 the number as NSelPass.

464 The acceptance is defined by: **acceptance = NPassAcc/NBGen**.

465 The selection efficiency is defined by: **selection efficiency = NSelPass/NPassAcc**.

466 Here, we denote α as the acceptance and ϵ as the selection efficiency.

467 However, we see from the B p_T shape systematics studies. There is a very high systematic
 468 uncertainty due to our little knowledge about the B_s^0 p_T shape. Therefore we use the following
 469 event by event weighting strategies to calculate the **efficiency correction factor**: $\frac{1}{\alpha \times \epsilon}$.

470 7.2 2D $\frac{1}{\alpha \times \epsilon}$ vs B p_T and B $|y|$ Map

471 We know that, the $B_s^0 \frac{1}{\alpha \times \epsilon}$ factor has not only p_T dependence, but also rapidity dependence.
 472 Therefore, first we create 2D maps of $\frac{1}{\alpha \times \epsilon}$ vs B p_T and B $|y|$. The binning is fine: 10 B p_T bins
 473 in 5 - 10 GeV/c and 40 bins at 10 - 50 GeV/c. The B $|y|$ bin is 0.0 - 0.5 - 1.0 - 1.5 - 2.0 - 2.4. In
 474 addition, we apply the Tag and Probe scale factor correction to the 2D $\frac{1}{\alpha \times \epsilon}$ map. Our TnP 2D
 475 maps are shown on Figure 33 and number of MC RECO level signal distributions Figure 35.

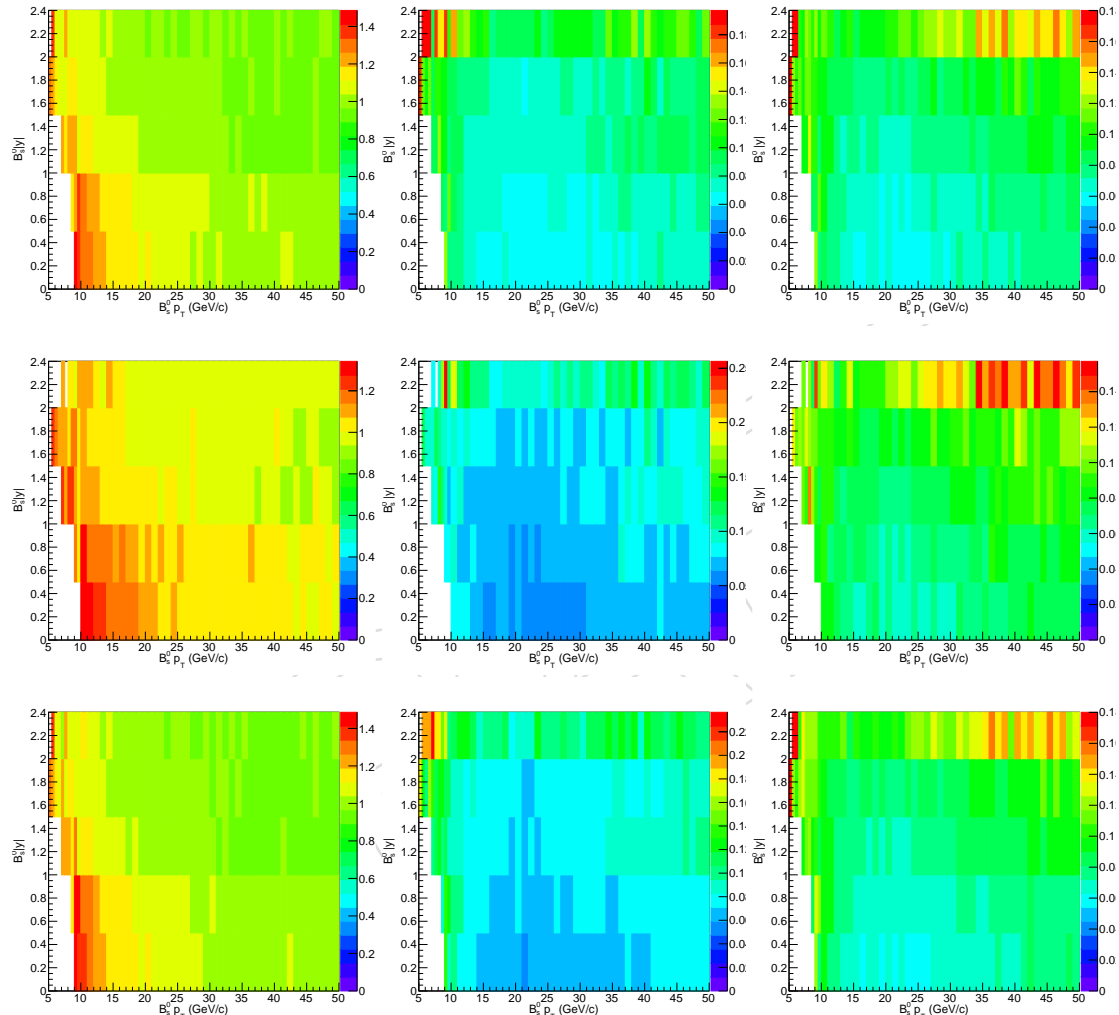


Figure 33: The finely binned 2D tag and probe scaling factor vs B p_T and B $|y|$ and their upper and lower uncertainties are for 0 - 90% (top), 0 - 30% (middle), and 30% - 90% (bottom) are shown respectfully above.

476 In fact, there is no significant centrality dependence on the B_s^0 tag and probe scale factors. We
 477 can take the ratio of 0 - 30% and 30% - 90% to the inclusive 0 - 90%. Figure 34 shows the 2D
 478 map ratios:

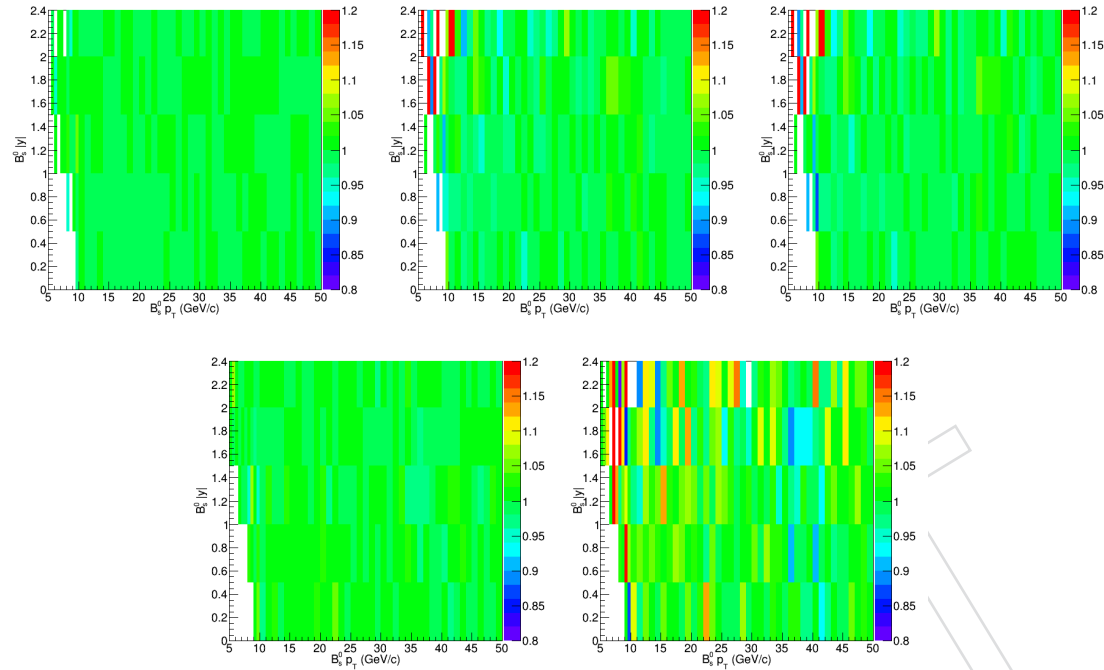


Figure 34: The finely binned 2D tag and probe scaling factor ratio to the inclusive 0 - 90% vs B p_T and B $|y|$ and their upper and lower uncertainties are for 0 - 30% (up) and 30% - 90% (down) are shown respectfully above.

479 Again, we have explicitly shown that their ratio is consistent with unity within uncertainties
 480 and thus no significant centrality is observed for the tag and probe scale factors.

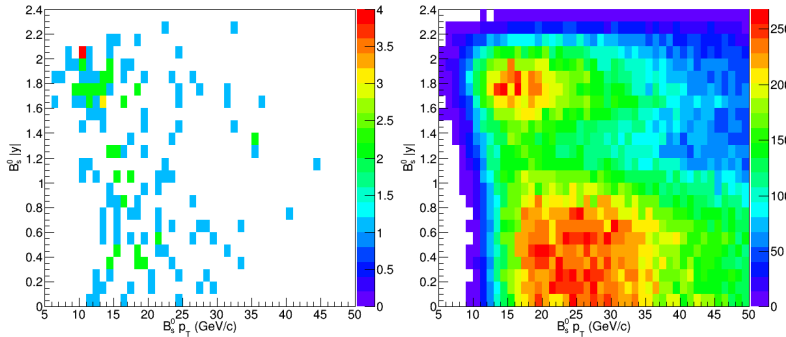


Figure 35: The finely binned 2D candidates distribution vs $B_s^0 p_T$ and $B_s^0 |y|$ for data and MC at centrality 0 - 90% are shown respectfully above.

481 7.3 MC RECO and GEN Statistics

482 To generate the 2D efficiency map vs $B_s^0 p_T$ and $|y|$, we first generate the 2D map of RECO
 483 and GEN distribution from the official MC. Figure 36 shows the 2D maps of RECO and GEN
 484 statistics for the $B_s^0 p_T$ and $|y|$ binning used in the analysis

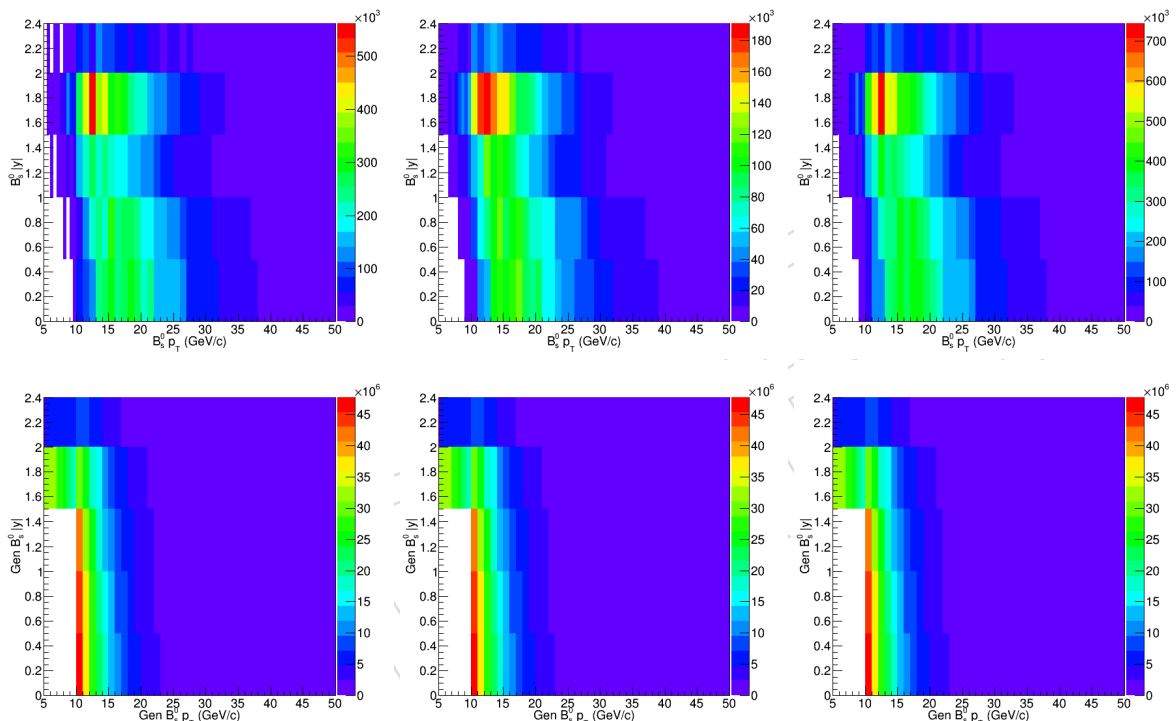


Figure 36: The finely binned 2D statistics distributions vs $B p_T$ and $B |y|$ for RECO (top) and GEN (bottom) levels in the MC at 0 - 30%, 30% - 90%, and 0 - 90% centrality are shown above.

⁴⁸⁵ In our event-by-event efficiency correction scheme, we correct the efficiency according to the
⁴⁸⁶ data candidates kinematics in the 2D maps. The minimum number of RECO B_s^0 candidates for
⁴⁸⁷ all p_T and centrality bins are shown on Table 10

Table 10: The minimum RECO statistics for each p_T and centrality bins used in our efficiency correction factor $\langle \frac{1}{\alpha \times \epsilon} \rangle$ are shown above.

Centrality	p_T (GeV/c)	Minimum RECO Statistics
0 - 90%	7 - 10	24625
0 - 90%	10 - 15	106014
0 - 90%	15 - 20	68216
0 - 90%	20 - 50	7789
0 - 30%	10 - 50	18679
30 - 90%	10 - 50	2186
0 - 90%	10 - 50	7789

⁴⁸⁸ Therefore, we can see that we have enough statistics to calculate our efficiency correction factor
⁴⁸⁹ $\langle \frac{1}{\alpha \times \epsilon} \rangle$ based on the data candidate kinematics.

⁴⁹⁰ 7.4 Efficiency Correction Over Fiducial Region

⁴⁹¹ As we can see, from Fig 35 and 37, that the acceptance at the low B p_T region: B $p_T < 10$ GeV/c
⁴⁹² and $B |y| < 1.5$ basically has 0 acceptance and no B_s^0 candidate is found. This means that our
⁴⁹³ detector cannot measure B mesons with that kinematic range. Therefore, we will exclude to
⁴⁹⁴ correction of B $p_T < 10$ GeV/c and $B |y| < 1.5$ region. This means that the kinematic phase
⁴⁹⁵ space of our measurement will be fiducial. Its range will be 7 GeV/c $< B_s^0 p_T < 10$ GeV/c with
⁴⁹⁶ $1.5 < B_s^0 |y| < 2.4$ and 10 GeV/c $< B_s^0 p_T < 50$ GeV/c with $B_s^0 |y| < 2.4$. The TnP scaling factor
⁴⁹⁷ corrected $\frac{1}{\alpha}$, $\frac{1}{\epsilon}$, and $\frac{1}{\alpha \times \epsilon}$ vs B p_T and $B |y|$ 2D map within our fiducial region are shown as Figure
⁴⁹⁸ 37 below:

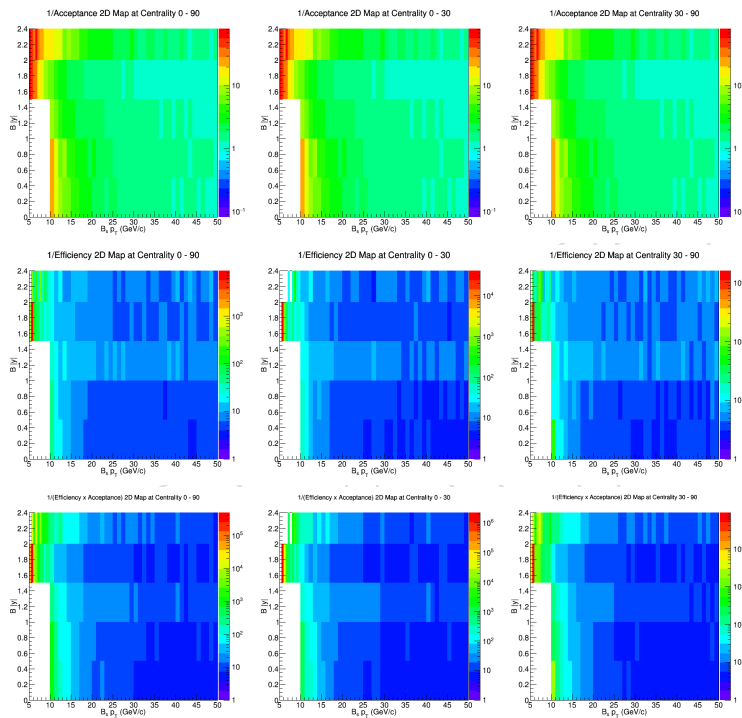


Figure 37: The finely binned 2D distribution $\frac{1}{\alpha}$ (top), $\frac{1}{\epsilon}$ (middle), and $\frac{1}{\alpha \times \epsilon}$ (bottom) vs $B p_T$ and $B |y|$ at 0 - 90% (left), 0 - 30% (middle), and 30% - 90% (right) are shown respectfully above.

499 **7.5 Event-By-Event Reweighting Techniques**

500 We loop through our B_s^0 candidates and apply analysis selections to the candidates. Then we
 501 loop through the candidates that pass our analysis cuts. We readout their $\frac{1}{\alpha \times \epsilon}$ according to
 502 their kinematics and store in a tree. Our candidates in general contain not only signal but also
 503 background. In order to ensure we use most signal candidates to perform the $\frac{1}{\alpha \times \epsilon}$ correction,
 504 we then apply a mass restriction cut of $0.09 \text{ GeV}/c^2$ for $7 \text{ GeV}/c < B_s^0 p_T < 10 \text{ GeV}/c$ and 0.08
 505 GeV/c^2 for $10 \text{ GeV}/c < B_s^0 p_T < 50 \text{ GeV}/c$ near the B_s^0 PDG peak mass to reject background
 506 candidates. For B_s^0 , we have 104 candidates in the signal region. Our signal yield in Section
 507 6 shows that we have about 90 signals candidates. Therefore, the signal to background ratio
 508 is 90:14. The effect of background candidate here is negligible and can be ignored. But we
 509 could improve with sPLOT techniques to assign weight to the candidates when we do the $\frac{1}{\alpha \times \epsilon}$
 510 correction. We have created a dedicated section: 7.3 “sPLOT Weight Techniques Studies” to
 511 evaluate the size of the effect of background contamination in the signal region.

512 Next, we compute the average correction factor $\langle \frac{1}{\alpha \times \epsilon} \rangle$ according to the formula below

$$\langle \frac{1}{\alpha \times \epsilon} \rangle_i = \frac{1}{n_i} \sum_j^{n_i} \frac{1}{\alpha \times \epsilon_j} \quad (6)$$

513 Here i means the i th p_T bin and j is the j th candidate inside the p_T bin. Basically, we average
 514 the $\frac{1}{\alpha \times \epsilon}$ by each signal region candidate for each p_T bin and use the averaged $\langle \frac{1}{\alpha \times \epsilon} \rangle$ as the
 515 event by event weighted correction factor for our corrected yield calculation. We expect this
 516 event by event weighting method to eliminate the B p_T shape systematics. We will perform the
 517 systematics studies of this technique in the systematics uncertainties 10

518 **7.6 Final Results**

519 Finally, after TnP and event by event weighted, we have the $\langle \frac{1}{\alpha \times \epsilon} \rangle$ vs p_T for 0 - 90% and inclu-
 520 sive p_T for 0 - 90%, 0 - 30%, 30% - 90% shown on Figure 38 and Figure 39.

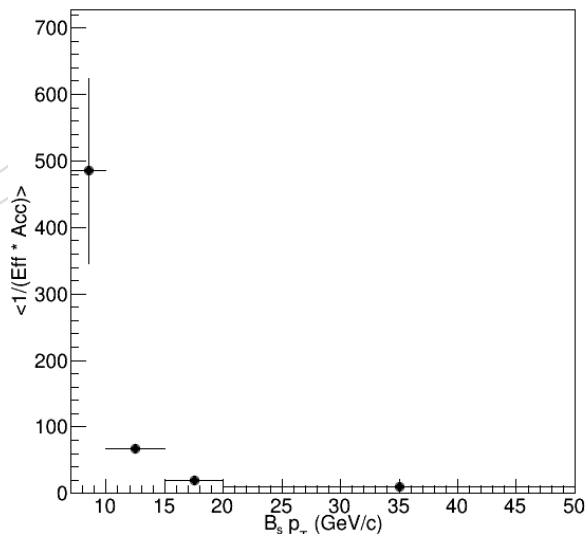


Figure 38: The p_T differential $\langle \frac{1}{\alpha \times \epsilon} \rangle$ for centrality 0 - 90% is shown above.

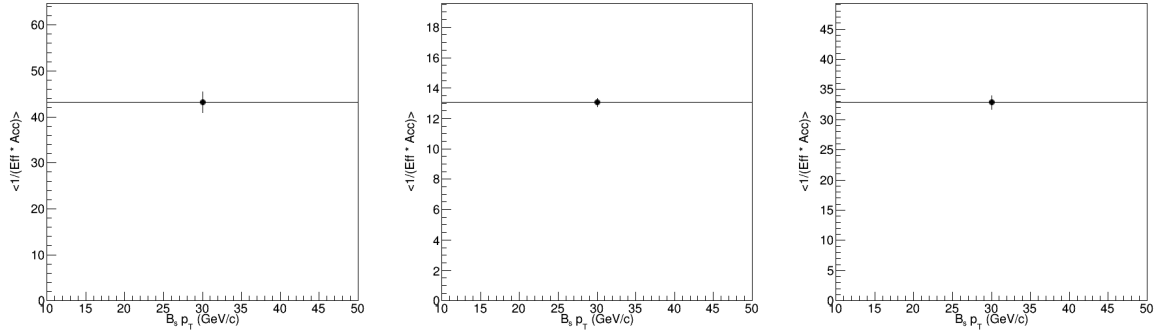


Figure 39: The p_T inclusive $\langle \frac{1}{\alpha \times \epsilon} \rangle$ for centrality 0 - 30% (left), 30% - 90% (middle), 0 - 90% (right) are shown above.

521 The precise central values and uncertainties of the $\langle \frac{1}{\alpha \times \epsilon} \rangle$ are also summarized in Table 11 below

Table 11: The precise central values and uncertainties of the efficiency correction factors $\langle \frac{1}{\alpha \times \epsilon} \rangle$ are summarized below.

Centrality	p_T (GeV/c)	$\langle \frac{1}{\alpha \times \epsilon} \rangle$ Central Value	$\langle \frac{1}{\alpha \times \epsilon} \rangle$ Propagated Error
0 - 90%	7 - 10	485.2	139.1
0 - 90%	10 - 15	67.9	3.3
0 - 90%	15 - 20	20.04	0.50
0 - 90%	20 - 50	10.42	0.32
0 - 30%	10 - 50	43.16	2.28
30 - 90%	10 - 50	13.06	0.28
0 - 90%	10 - 50	32.86	1.14

522 7.7 sPlot Weight Techniques Studies

523 Again, to understand the effects of the possible contamination in the signal region on the ef-
 524 ficiency factor $\langle \frac{1}{\alpha \times \epsilon} \rangle$, we apply sPlot techniques [16] to separate the signal and background in
 525 the data. We assign a weight to each candidates and recompute the weighted average $\langle \frac{1}{\alpha \times \epsilon} \rangle$
 526 defined as follows:

$$\langle \frac{1}{\alpha \times \epsilon} \rangle_i = \frac{\sum_j^{n_i} w_j \frac{1}{\alpha \times \epsilon_j}}{\sum_j^{n_i} w_j} \quad (7)$$

527 First, we perform the fits on the discriminating variables, the invariant mass of B_s^0 , to obtain
 528 the sPlot weights. The fits on the inclusive 5 - 50 GeV/c B_s^0 invariant mass distribution and the
 529 pull distribution are shown below

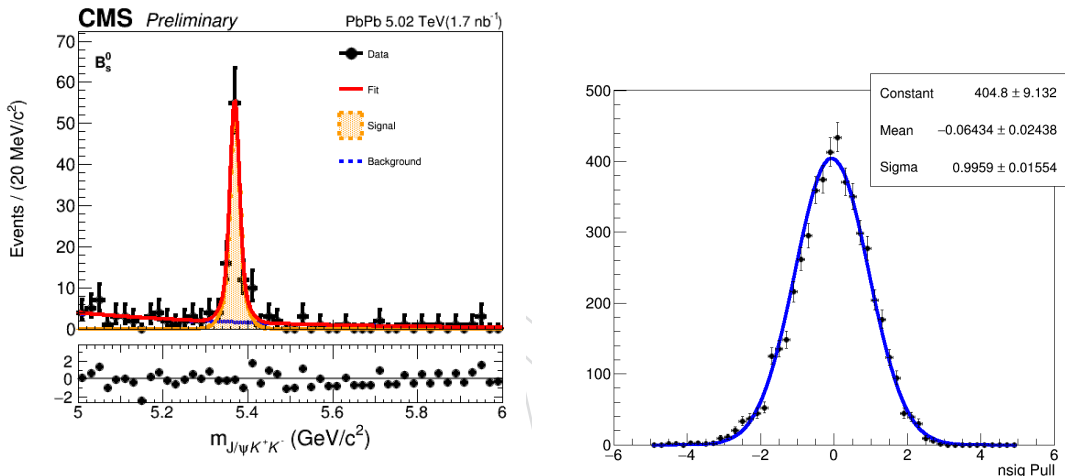


Figure 40: The 5 - 50 GeV/c B_s^0 invariant mass distribution and the raw yield fits are shown on the left. The pull distribution from the invariant mass fits is shown on the right.

530 As we can see from Figure 40, we have a good closure on the fit on all B_s^0 candidates to obtain
 531 the sPlot weights. The sPlot weight distribution of the B^+ candidates in the data passing the
 532 analysis selection is shown below in Figure 41 . Note that the weight can be negative or greater
 533 than 1 just as a normal sPlot weight applied in data-MC comparison studies.
 534 The sPlot weight distribution of the B_s^0 candidates in the data passing the analysis selection is
 535 shown below in Figure 41 . Note that the weight can be negative or greater than 1 just as a
 536 normal sPlot weight applied in data-MC comparison studies.

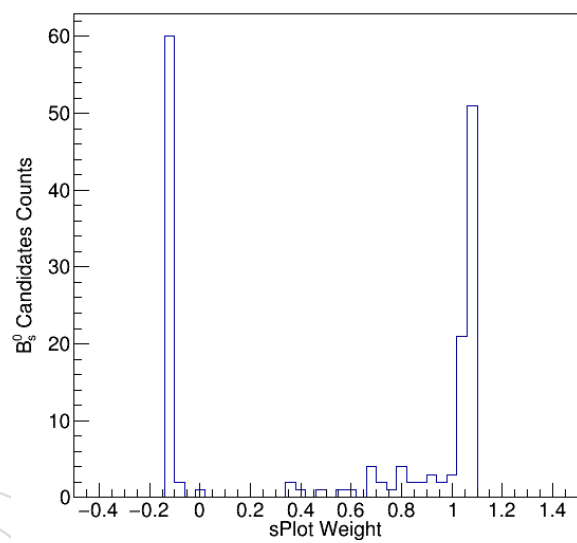


Figure 41: The sPlot weight distribution for B_s^0 candidates. They will be used to compute the sPlot weighted efficiency.

With the weights, we then recompute the efficiency correction factor $\langle \frac{1}{\alpha \times \epsilon} \rangle$ for each p_T and centrality bin. Our sPlot weighted results and the comparison with the nominal efficiency correction factor $\langle \frac{1}{\alpha \times \epsilon} \rangle$ for p_T and centrality bins are shown below in Figure 42 and Figure 43

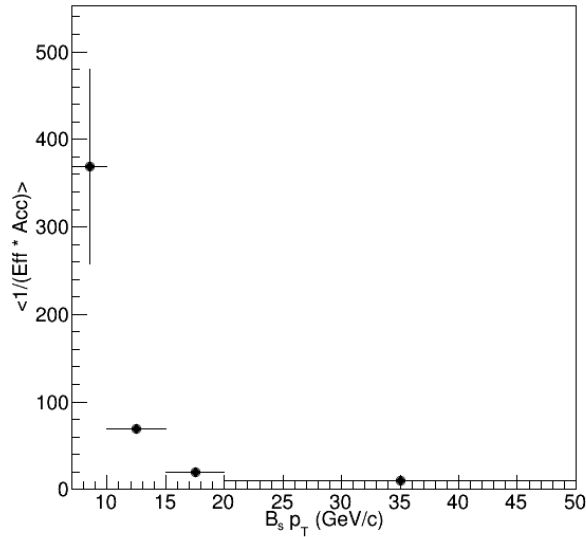


Figure 42: The p_T differential $\langle \frac{1}{\alpha \times \epsilon} \rangle$ for centrality 0 - 90% is shown above.

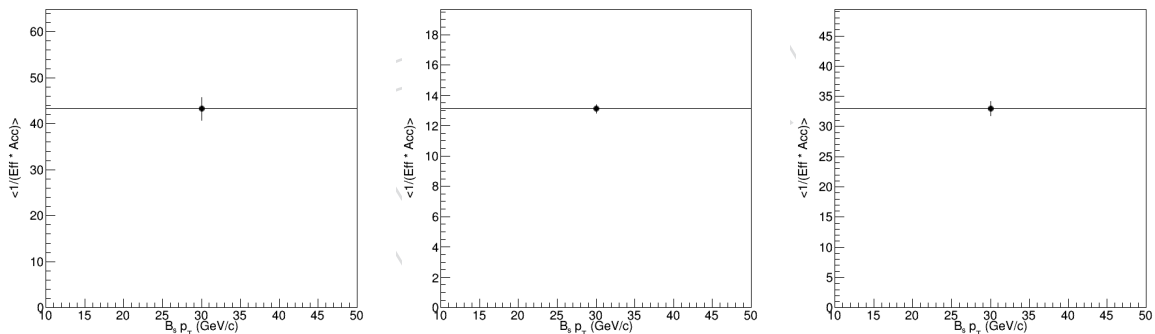


Figure 43: The p_T inclusive $\langle \frac{1}{\alpha \times \epsilon} \rangle$ for centrality 0 - 30% (left), 30% - 90% (middle), 0 - 90% (right) are shown above.

540 We compare numerically the value of $\langle \frac{1}{\alpha \times \epsilon} \rangle$ with and without sPlot weight. The results are
 541 summarized below on Table 12

Table 12: The precise central values and uncertainties of the efficiency correction factors $\langle \frac{1}{\alpha \times \epsilon} \rangle$ are summarized below.

Centrality	p_T (GeV/c)	$\langle \frac{1}{\alpha \times \epsilon} \rangle$ Weighted	$\langle \frac{1}{\alpha \times \epsilon} \rangle$ Unweighted	Percent Deviation
0 - 90%	7 - 10	383.3	485.2	21.0%
0 - 90%	10 - 15	69.0	67.9	1.62%
0 - 90%	15 - 20	19.8	20.04	1.12%
0 - 90%	20 - 50	10.50	10.42	0.77%
0 - 30%	10 - 50	43.26	43.16	0.22%
30 - 90%	10 - 50	13.11	13.06	0.38%
0 - 90%	10 - 50	32.94	32.86	0.24%

542 As we can see, the sPlot weight effect is negligible and will not change our efficiency correction
 543 factor $\langle \frac{1}{\alpha \times \epsilon} \rangle$ significantly. Except the lowest p_T bin, they are well with 2%. For the first p_T bin
 544 from 7 - 10 GeV/c, although it is 24.0%, which appears to be big, indeed, it is still negligible
 545 compared to its systematic errors. According to section 10 Systematics, we have a total system-
 546 atic uncertainties of +51.08% and -49.10%. Therefore, adding this systematic uncertainties to
 547 the total systematics, we will have +55.2% -53.4%, which is only a 5% change and it is not really
 548 significant.

549 Therefore, we will stick to use the nominal one without applying the sPlot weight as our nom-
 550 inal values in the final results.

551 8 Closure Test of the B_s Corrected Yield

552 In order to confirm that our final results are close, we perform a comprehensive closure test
 553 on the corrected yield, which is defined by the first equation in 9. Basically, we need to verify
 554 two components: the raw yield, which is obtain from the unbinned fit on the B_s invariant mass
 555 distribution and the efficiency correction factor $\langle \frac{1}{\alpha \times \epsilon} \rangle$, which obtain from the data weighted
 556 average of the efficiencies from the 2D map. We first validate the fit functions to see if they
 557 properly describe the data. Then, we create the pull distribution made by different data-like
 558 MC samples to see if the fits properly calculated the raw yields and their uncertainties. Sub-
 559 sequently, we move on to verify the efficiency correction in the limit of high statistics. Finally,
 560 we perform the closure test on the efficiency of different data-like MC samples to estimate the
 561 potential bias and quote the percentage deviation as the systematic uncertainties.

562 8.1 Closure Test on the Raw Yield Fits

563 We use double Gaussian function, which is the same as the B-meson analysis in CADI HIN-18-
 564 007, to model the signal and use exponential function to model the background. We validate
 565 the fits on the data by generating 5000 toy MC based on the parameters of the fitting function
 566 using the ROOFit framework as follows

567

```
568 RooMCStudy* mcstudy = new RooMCStudy(*model, Bmass, Extended(), FitOptions(Save(kTRUE),  

  569 PrintEvalErrors(0)));  

  570  

  571 mcstudy->generateAndFit(5000);
```

573 We perform the fits of each generated toy and create the distribution of mean, error, pull of the
 574 mean and the nsig parameter, which physically stand for the B_s mass peak value and the raw
 575 yield of the fit. We perform Gaussian fits on the pull distributions to test if we are able to get a
 576 fit with mean 0 and width 1. Figure 44 shows the fits closure of the mean parameter for all p_T
 577 bins.

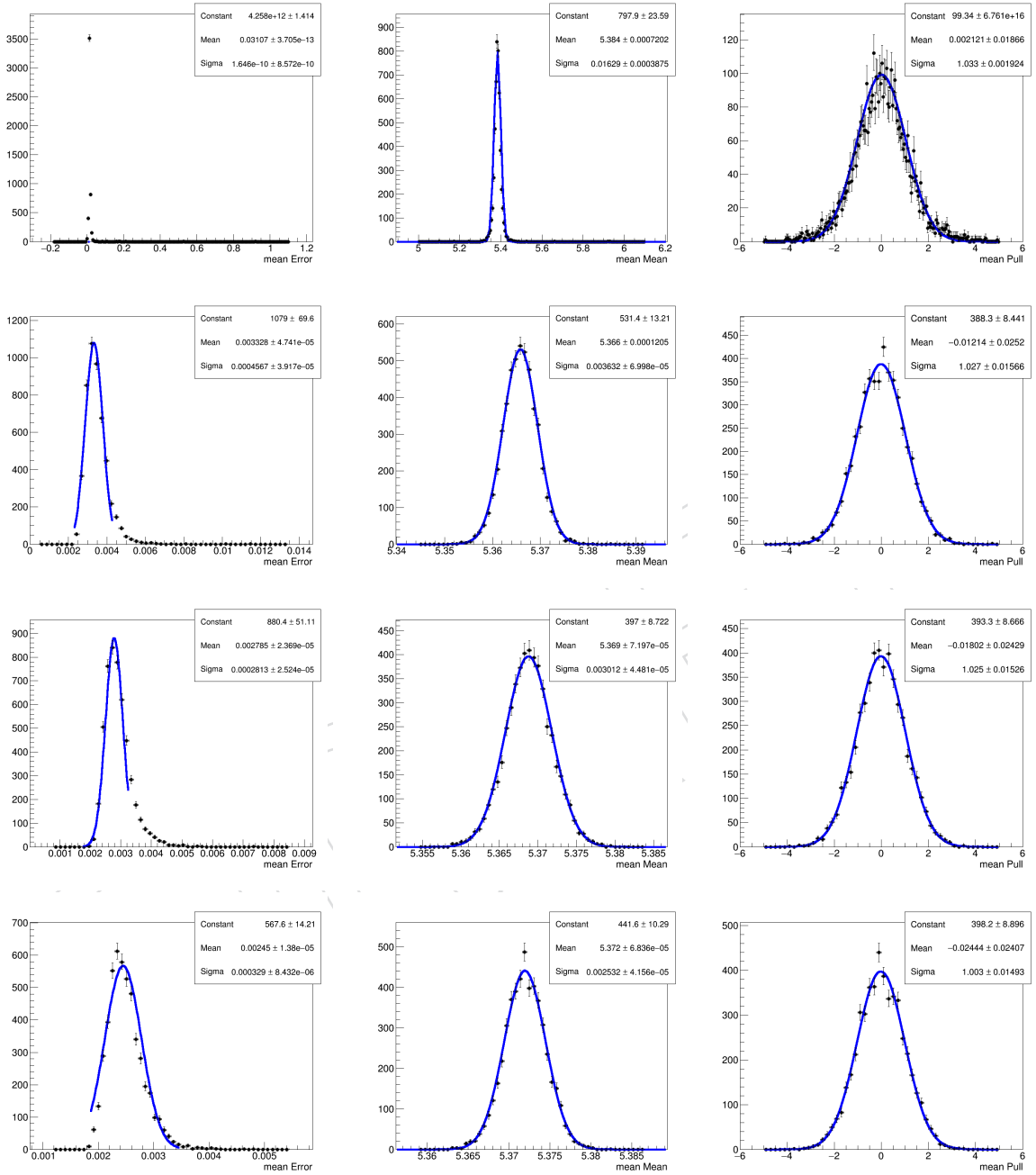


Figure 44: The mean (left), error (middle), pull (right) of the B_s n_{sig} parameter are shown as above. We can see that the B_s n_{sig} parameter have a perfect closure with pull distributions centered at 0 with unit width according to the Gaussian fits. From top to bottom: 7 - 10, 10 - 15, 15 - 20, and 20 - 50 GeV/c. Therefore, we have confirmed that the fitting functions are valid.

578 Figure 45 shows the fits closure of the mean parameter for all centrality bins and Figure 46
 579 shows the fits closure of the raw yield parameter for all p_T bins.

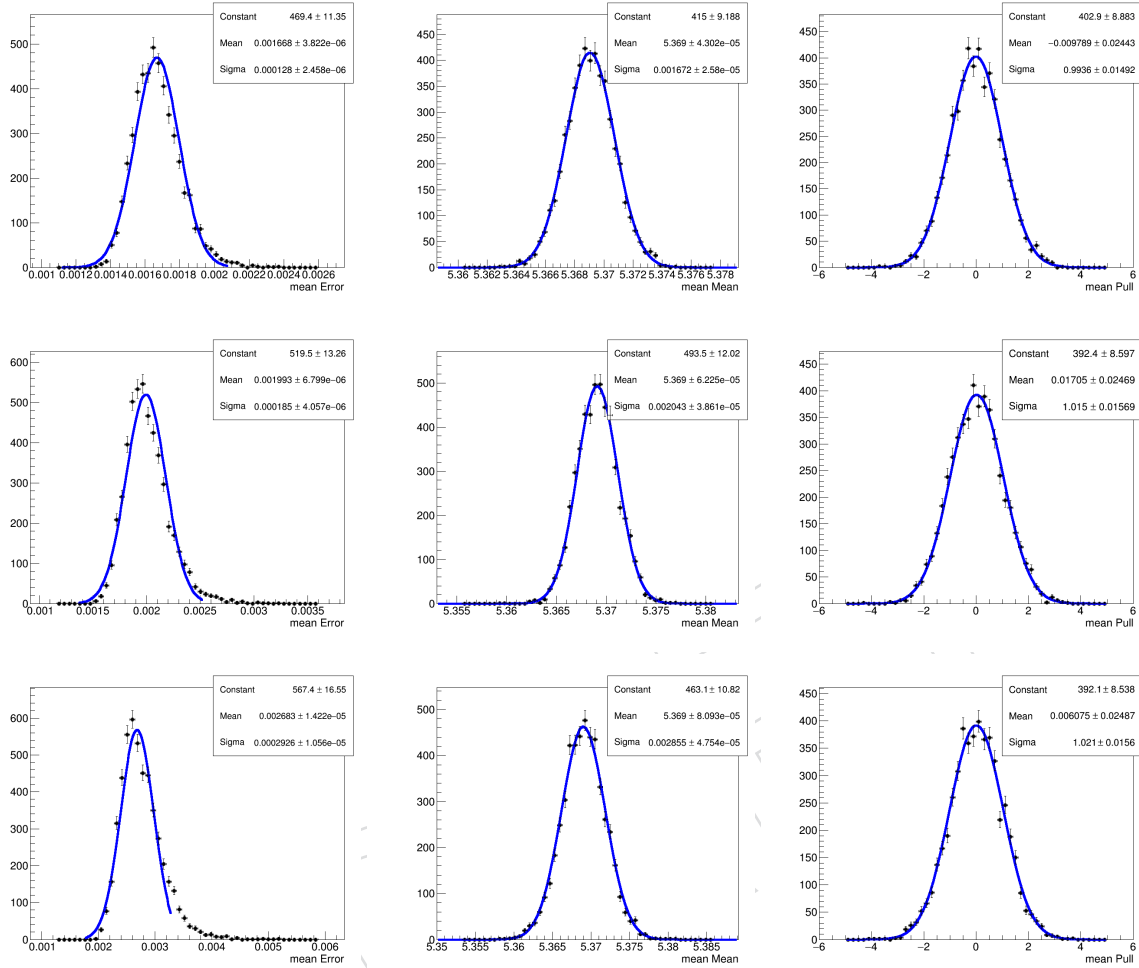


Figure 45: The mean (left), error (middle), pull (right) of the B_s are shown as above. We can see that the B_s have a perfect closure with pull distributions centered at 0 with unit width according to the Gaussian fits. From top to bottom: 0 - 90%, 0 - 30%, and 30 - 90%. Therefore, we have confirmed that the fitting functions are valid.

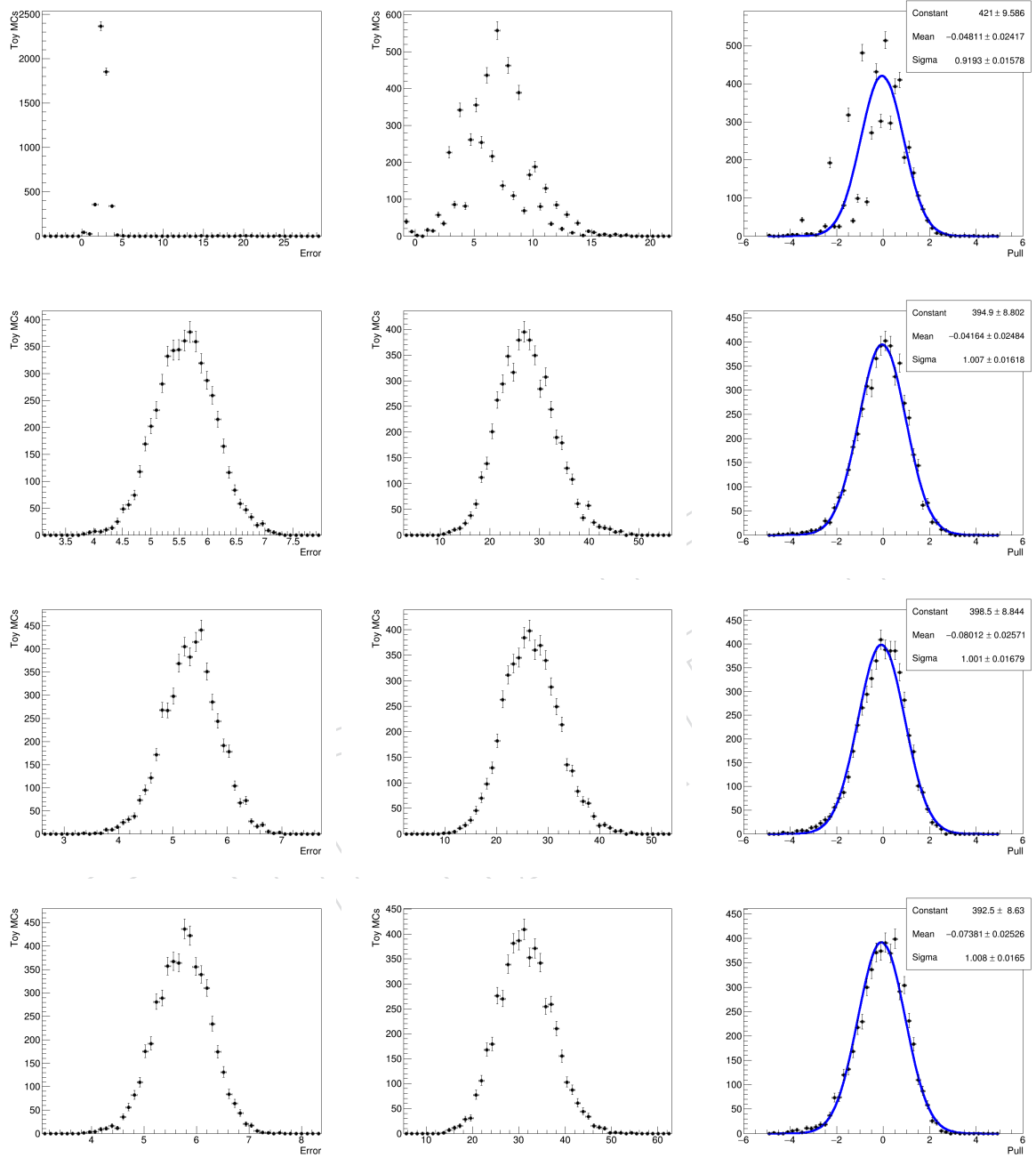


Figure 46: The mean (left), error (middle), pull (right) of the B_s raw yield parameter are shown as above. We can see that the B_s have a perfect closure with pull distributions centered at 0 with unit width according to the Gaussian fits. From top to bottom: 7 - 10, 10 - 15, 15 - 20, and 20 - 50 GeV/c. Therefore, we have confirmed that the fitting functions are valid and give us correct raw yield to calculate the corrected yield.

580 Figure 47 shows the fits closure of the raw yield parameter for all centrality bins.

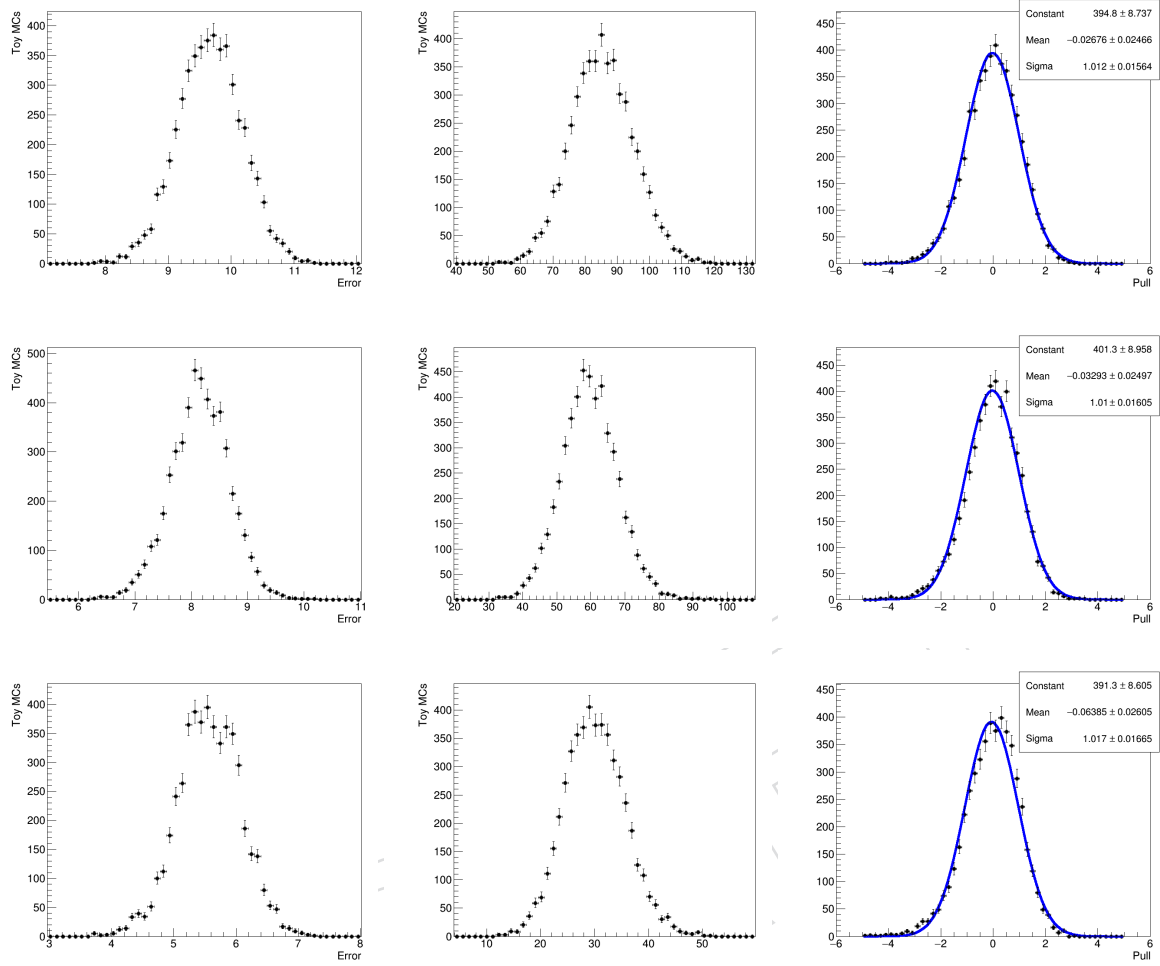


Figure 47: The mean (left), error (middle), pull (right) of the B_s raw yield parameter are shown as above. We can see that the B_s have a perfect closure with pull distributions centered at 0 with unit width according to the Gaussian fits. From top to bottom: 0 - 90%, 0 - 30%, and 30 - 90%. Therefore, we have confirmed that the fitting functions are valid and give us correct raw yield to calculate the corrected yield.

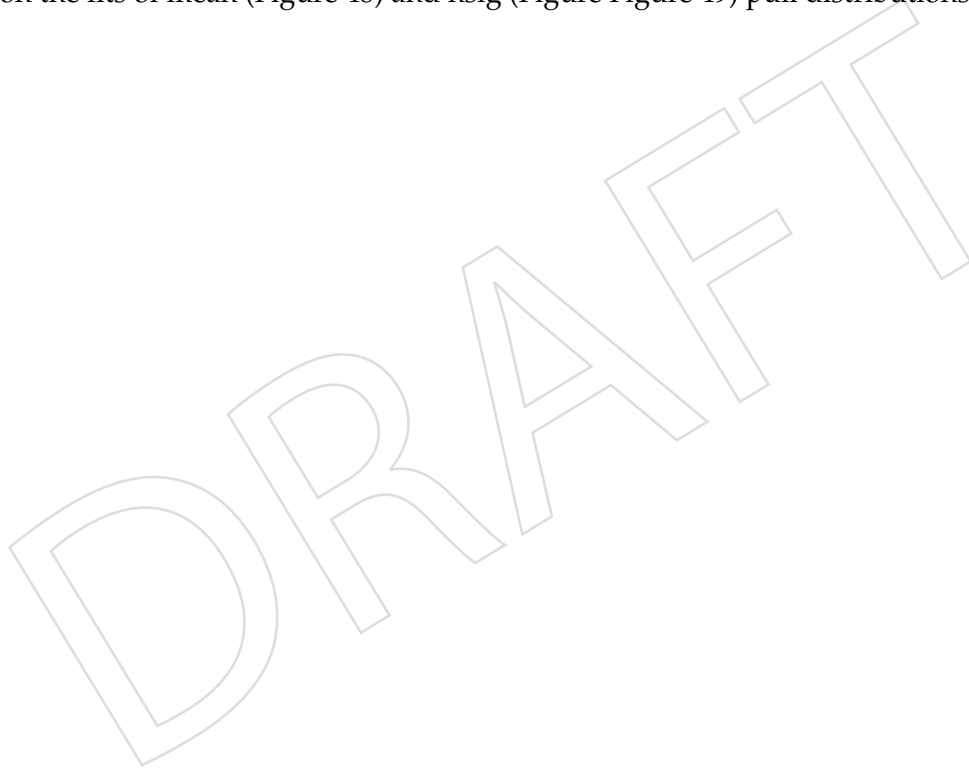
581 The results from Figure 44, Figure 45, Figure 46, and Figure 47 confirm the validity of our fits
582 on the B_s Invariant mass distribution to extract the raw yield.

583 **8.1.1 Validation of Raw Yield and Raw Yield Error from the Fits**

584 Next, we construct the data-like MC samples. We take the full one \hat{p}_T MC and randomly sample
585 a fixed number of generated candidates according to the statistics of the actual data. We let the
586 reconstructed candidates vary according to the randomness of the efficiency. We will perform
587 the fits on all data-like MC samples to extract the mean and error of the raw yield. Then we
588 will make the pull distribution from the mean and error of the raw yield. The pull is defined as
589 follows:

$$Pull = \frac{Y_i - Y_{exp}}{\sqrt{Y_i}} \quad (8)$$

590 Here Y_{exp} is the number of the expected yield scaled down according to the fixed number of
591 generated B_s candidates. The reconstructed B_s candidates will vary by the randomness of the
592 efficiency of each data-like MC samples. Likewise, we plot the pull distribution of the mean
593 and nsig, perform Gaussian fits on them, and check if the fits give us unit pulls. Below are our
594 results on the fits of mean (Figure 48) and nsig (Figure Figure 49) pull distributions



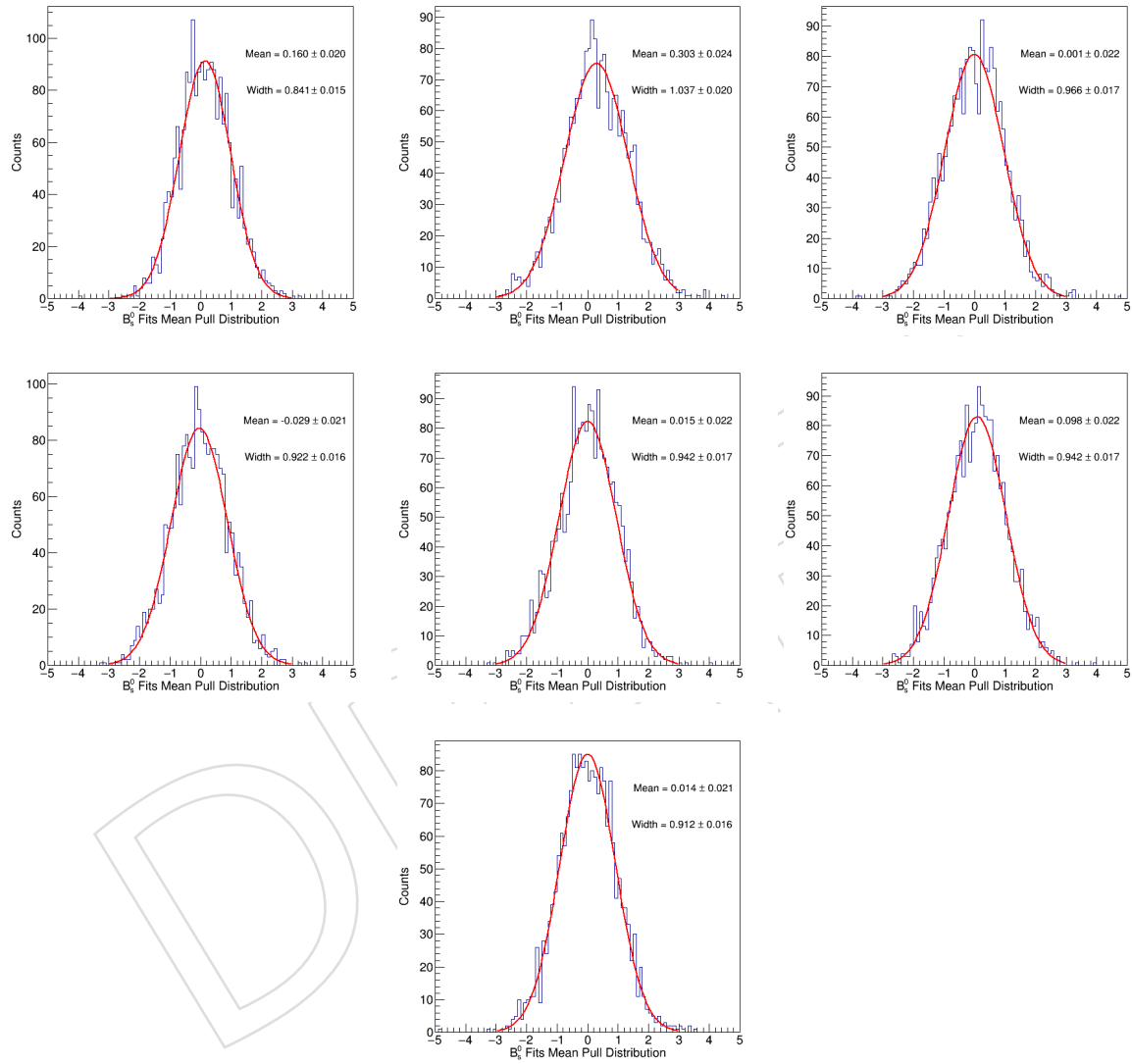


Figure 48: The pull distributions of mean parameter for the data-like randomly sampled MC samples for 0 - 90% at 7 - 10, 10 - 15, 15 - 20, and 20 - 50 GeV/c as well as 0 - 90%, 0 - 30%, and 30 - 90% from left to right and up to down are shown respectfully above.

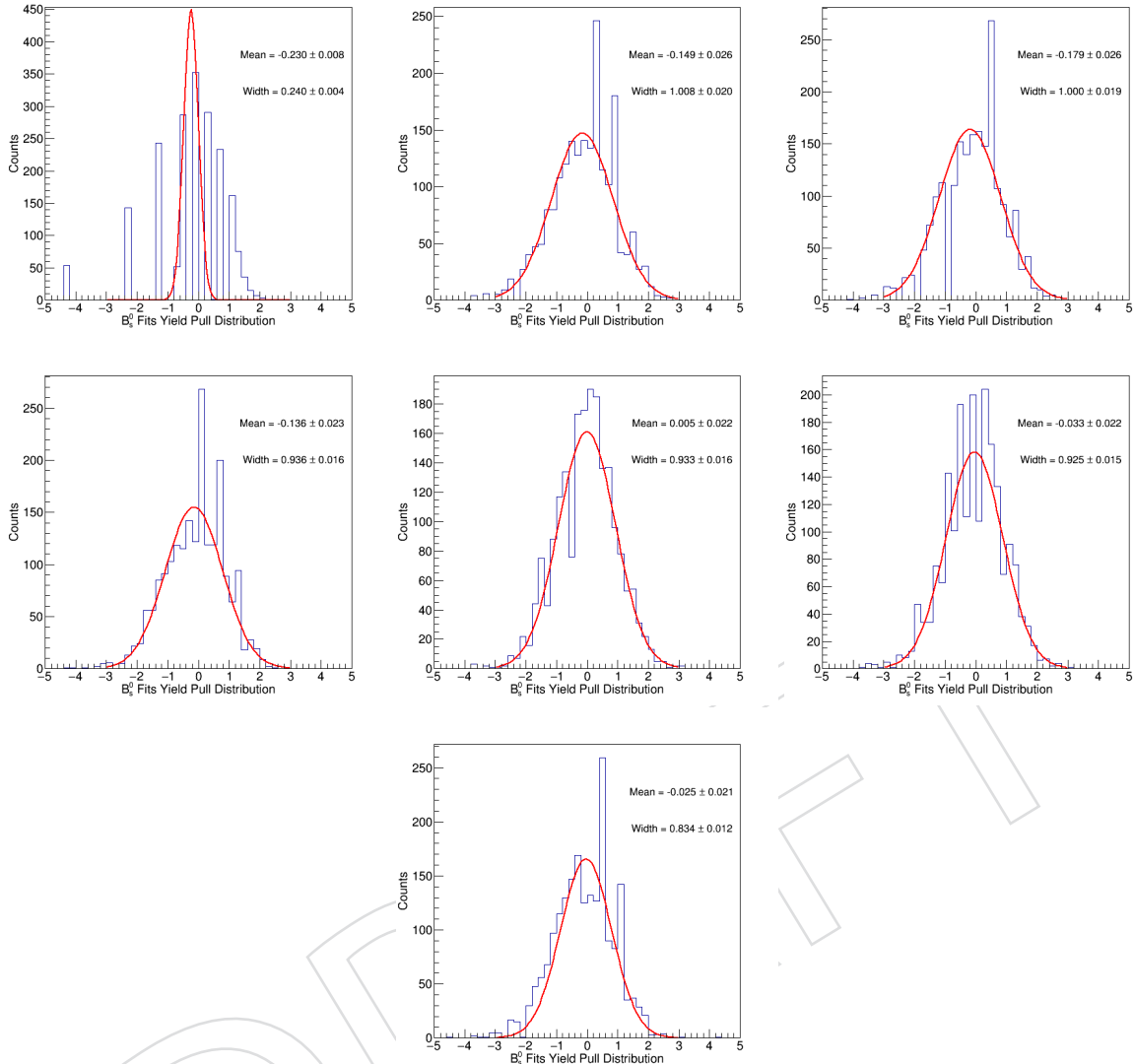


Figure 49: The pull distributions of raw yield parameter for the data-like randomly sampled MC samples for 0 - 90% at 7 - 10, 10 - 15, 15 - 20, and 20 - 50 GeV/c as well as 0 - 90%, 0 - 30%, and 30 - 90% are shown

595 From Figure 48 and Figure 49, we can see that the closure of the both mean and nsig have
 596 good closure, which show a Gaussian pull distribution with mean at 0 and width about 1. This
 597 validate the raw yield and the raw yield error from our fits.

598 8.2 Closure Test on Efficiency Correction

599 Since we have already verify that the fits work, the next step is to validate the closure of the
 600 efficiency correct to avoid potential bias using the $\langle \frac{1}{\alpha \times \epsilon} \rangle$ as the overall efficiency correction
 601 factor. For here, we try both case. The high statistics case: one entire pthat MC sample. The
 602 low statistics case: 2000 spilt data-like MC samples same as the raw yield fit studies. Both
 603 cases use the same unweighted 2D $\langle \frac{1}{\alpha \times \epsilon} \rangle$ correction map from the input MC sample. In both
 604 cases, we compare the $\langle \frac{1}{\alpha \times \epsilon} \rangle$ to the expected value, which is the total number of generated
 605 B_s /total number of reconstructed B_s and quote the **percentage deviation = ($\langle \frac{1}{\alpha \times \epsilon} \rangle$ - expected
 606 value)/expected value** as the systematic uncertainties.

607 8.2.1 High Statistics Limit

608 We perform the analysis to calculate the efficiency factors $\langle \frac{1}{\alpha \times \epsilon} \rangle$ and $\frac{1}{\langle \alpha \times \epsilon \rangle}$ cases for one entire
 609 pthat MC sample and compare to its expected values of efficiency correction for each p_T and
 610 centrality bin. The results can be summarized in table 13 below

Table 13: The results of the efficiency factors $\langle \frac{1}{\alpha \times \epsilon} \rangle$ and $\frac{1}{\langle \alpha \times \epsilon \rangle}$ and their percentage deviation are shown above.

Centrality	p_T (GeV/c)	NRECO	GEN/RECO	$\langle \frac{1}{\alpha \times \epsilon} \rangle$	% Dev	$\frac{1}{\langle \alpha \times \epsilon \rangle}$	% Dev
0 - 90%	7 - 10	12102	117.495	112.958	-3.4%	80.5755	-30.6%
0 - 90%	10 - 15	1788	43.3865	43.1728	-0.493%	27.6409	-36.3%
0 - 90%	15 - 20	4577	13.7835	13.639	-1.05%	12.6465	-8.25%
0 - 90%	20 - 50	35980	6.38043	6.36748	-0.203%	5.9658	-6.50%
0 - 90%	10 - 50	9522	12.2694	12.2668	-0.0212%	6.5642	-28.3%
0 - 30%	10 - 50	33143	7.70383	7.70087	-0.0384%	8.79954	-24.2%
30 - 90%	10 - 50	42453	8.72094	8.71793	-0.0345%	5.8419	-24.7%

611 In conclusion, we can see that the biases of the $\langle \frac{1}{\alpha \times \epsilon} \rangle$, which are all below 3.5%, are negligible
 612 compared other sources of uncertainties. On the contrary, the efficiency correction factor $\frac{1}{\langle \alpha \times \epsilon \rangle}$
 613 has a large bias. That also explains why we use $\langle \frac{1}{\alpha \times \epsilon} \rangle$ instead of $\frac{1}{\langle \alpha \times \epsilon \rangle}$ in our data analysis

614 8.2.2 Low Statistics Limit

615 Since we have validate the $\langle \frac{1}{\alpha \times \epsilon} \rangle$ correction is close at the limit of high statistics, next we are
 616 going to verify it in the limit of data-like statistics that is similar to our statistics in the data
 617 analysis. First, we sample a fixed amount of B_s generated particles and let the reconstructed
 618 candidates vary according to the variation of the efficiency. The randomly split MC data-like
 619 sample statistics for each p_T and centrality bins are shown below in Figure 50

620 Table 14 shows the mean statistics of the samples in our MC pseudo-data and comparison with
 621 the statistics from the data analysis

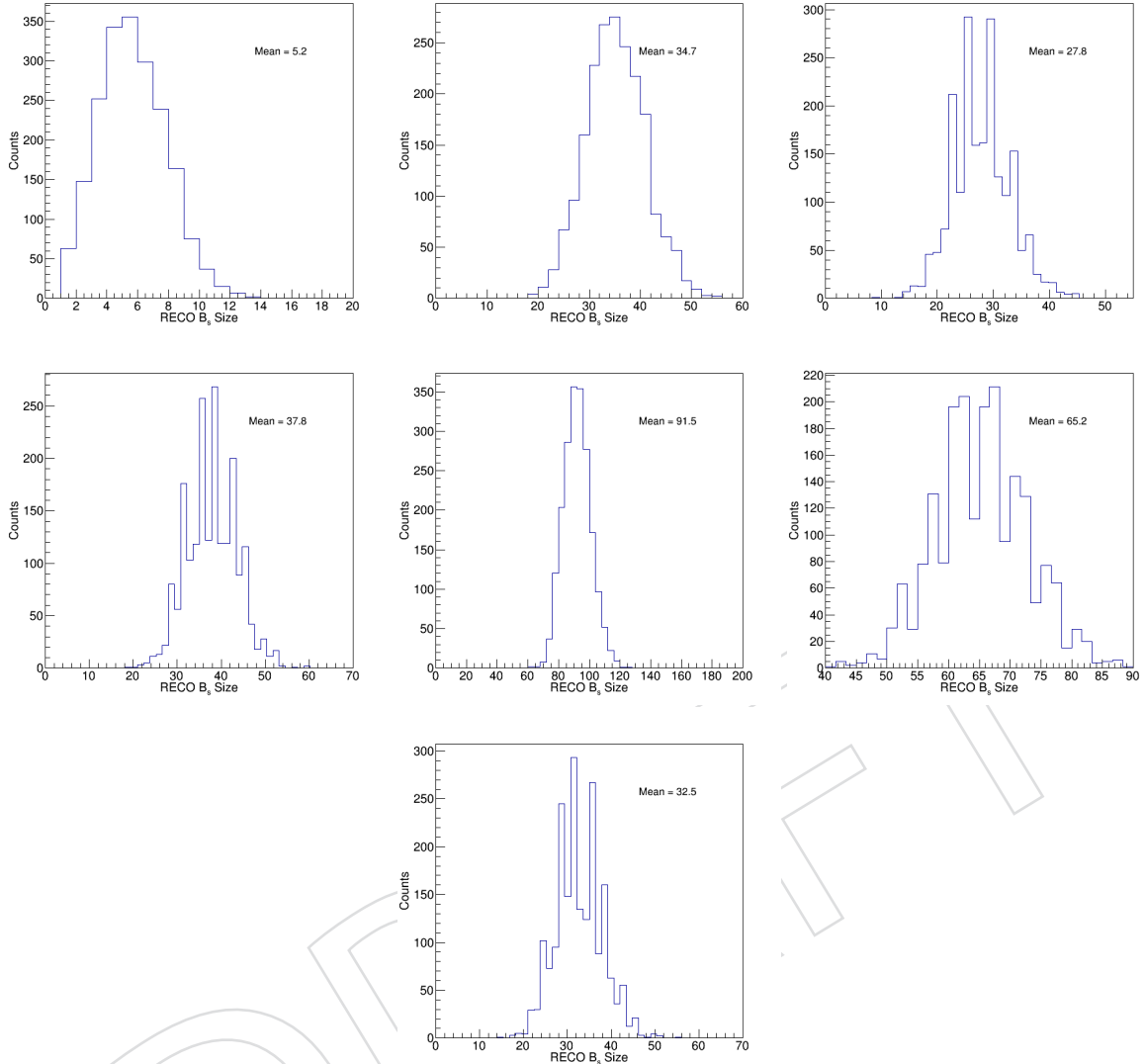


Figure 50: The number of reconstructed B_s distributions per sample for the data-like randomly sampled MC samples for 0 - 90% at 7 - 10, 10 - 15, 15 - 20, and 20 - 50 GeV/c as well as 0 - 90%, 0 - 30%, and 30 - 90%, respectively above.

Table 14: The comparison of the statistics of the Poisson resample dataset to the actual data in our analysis

Centrality	p_T (GeV/c)	Pseudo MC Samples	Actual Data
0 - 90%	7 - 10	5.2	5.92
0 - 90%	10 - 15	34.7	27.0
0 - 90%	15 - 20	27.8	26.6
0 - 90%	20 - 50	37.8	31.3
0 - 90%	10 - 50	91.5	84.9
0 - 30%	10 - 50	65.2	55.1
30 - 90%	10 - 50	32.5	29.9

622 We can see that the statistics is roughly centered at the statistics of the our data analysis. Subse-
 623 quently, we plot the percentage deviation for all p_T and centrality bins and compute their mean
 624 values. Our results are shown on Figure 51

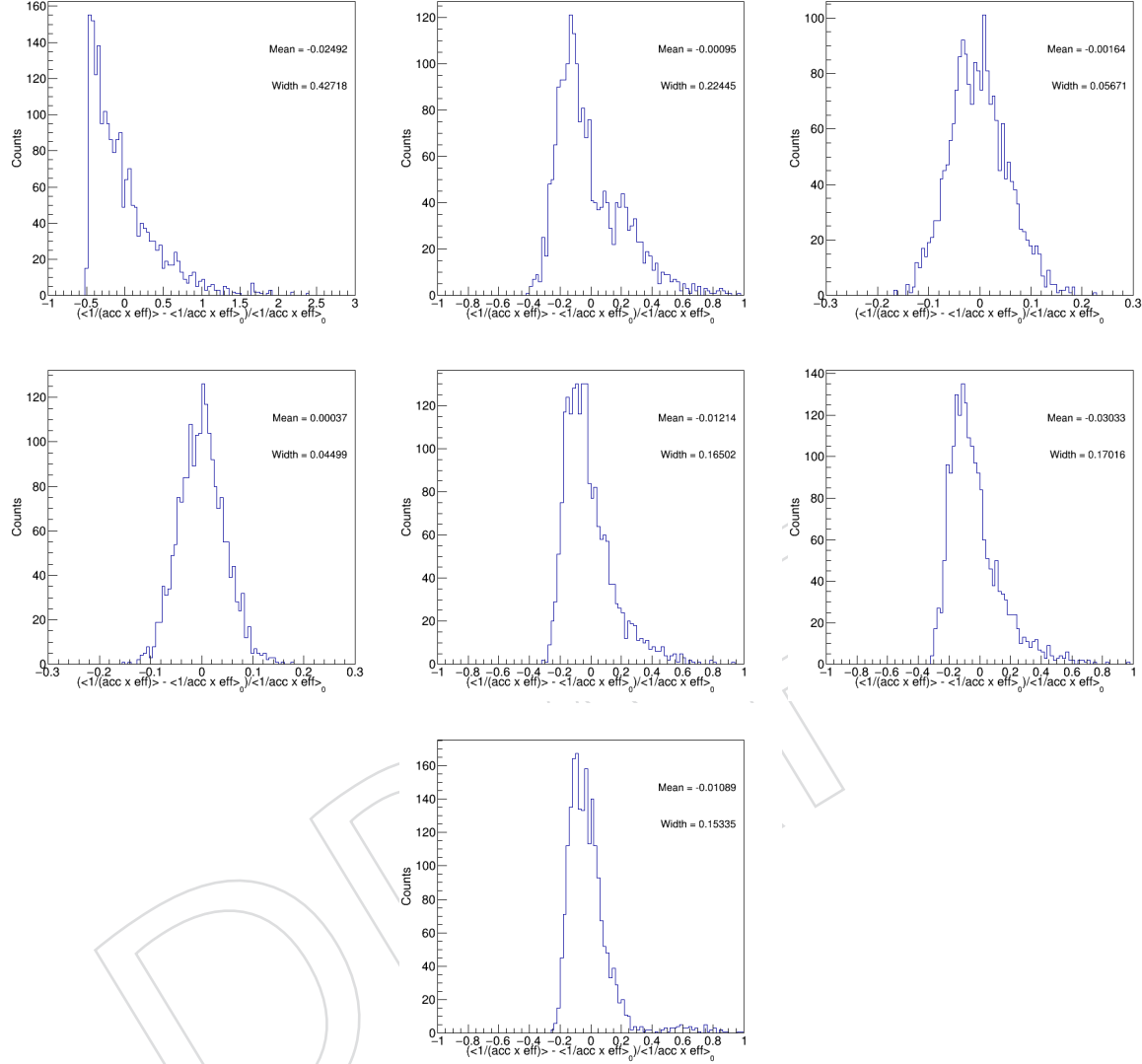


Figure 51: The percentage deviation distributions of $\langle \frac{1}{\text{acc} \times \text{eff}} \rangle$ to RECO/GEN for the data-like randomly sampled MC samples for 0 - 90% at 7 - 10, 10 - 15, 15 - 20, and 20 - 50 GeV/c as well as 0 - 90%, 0 - 30%, and 30 - 90% are shown respectfully above.

625 Finally, we quote the mean value as the systematic due to the non-closure of $\langle \frac{1}{\alpha \times \epsilon} \rangle$. The per-
 626 centage deviation is summarize in the table 15

Table 15: The percentage deviation of the efficiency factors from the expected value in the statistics similar to the data analysis are shown above.

Centrality	p_T (GeV/c)	% Dev
0 - 90%	7 - 10	-2.49%
0 - 90%	10 - 15	-0.10%
0 - 90%	15 - 20	-0.16%
0 - 90%	20 - 50	+0.03%
0 - 90%	10 - 50	-1.09%
0 - 30%	10 - 50	-1.21%
30 - 90%	10 - 50	-3.03%

627 In conclusion, we can see that, even in the limit of low statistics, which is similar to the statistics
 628 in our data analysis, the $\langle \frac{1}{\alpha \times \epsilon} \rangle$ correction method still gives us satisfying closure with bias
 629 within 3%.

DRAFT

8.3 Conclusion

From the studies of yield and $\langle \frac{1}{\alpha \times \epsilon} \rangle$ correction studies above, we can see that they both have good closure. Therefore, our data analysis does not have a significant bias and the systematic uncertainties due to bias are negligible compared to other sources of systematic uncertainties. Next, we need to verify the statistical uncertainties on the corrected yield using the $\langle \frac{1}{\alpha \times \epsilon} \rangle$ correction method, which is comprehensively discussed in the next section.

8.4 Data Bootstrap to Estimate the Statistical Uncertainties

To estimate the statistical uncertainties due to the $\langle \frac{1}{\alpha \times \epsilon} \rangle$, we propose the following steps :

1. We randomly resample the data after passing the selections for each p_T and centrality bin.
2. Each resampled data has the number of B_s according to Poisson distribution with the mean the same as the data analysis.
3. We randomly sample the data events N times according to the Poisson distribution to construct 1000 resampled datasets. Here, we allow repeated events in the resampled dataset.
4. We perform fits on the invariant mass distribution of the 1000 resampled datasets to extract the raw yield and make distribution of pull, mean, and error distribution of the raw yield.
5. We compare the raw yield from data bootstrap with pull distribution from the data fit to validate our data resampling machinery
6. We perform $\langle \frac{1}{\alpha \times \epsilon} \rangle$ corrections on the 1000 resampled datasets
7. We calculate the corrected yield of each resampled dataset by multiplying the raw yield to the efficiency correction factor $\langle \frac{1}{\alpha \times \epsilon} \rangle$ and plot the corrected yield distribution

First, we validate the size of the resampled datasets. The distribution are shown as follows

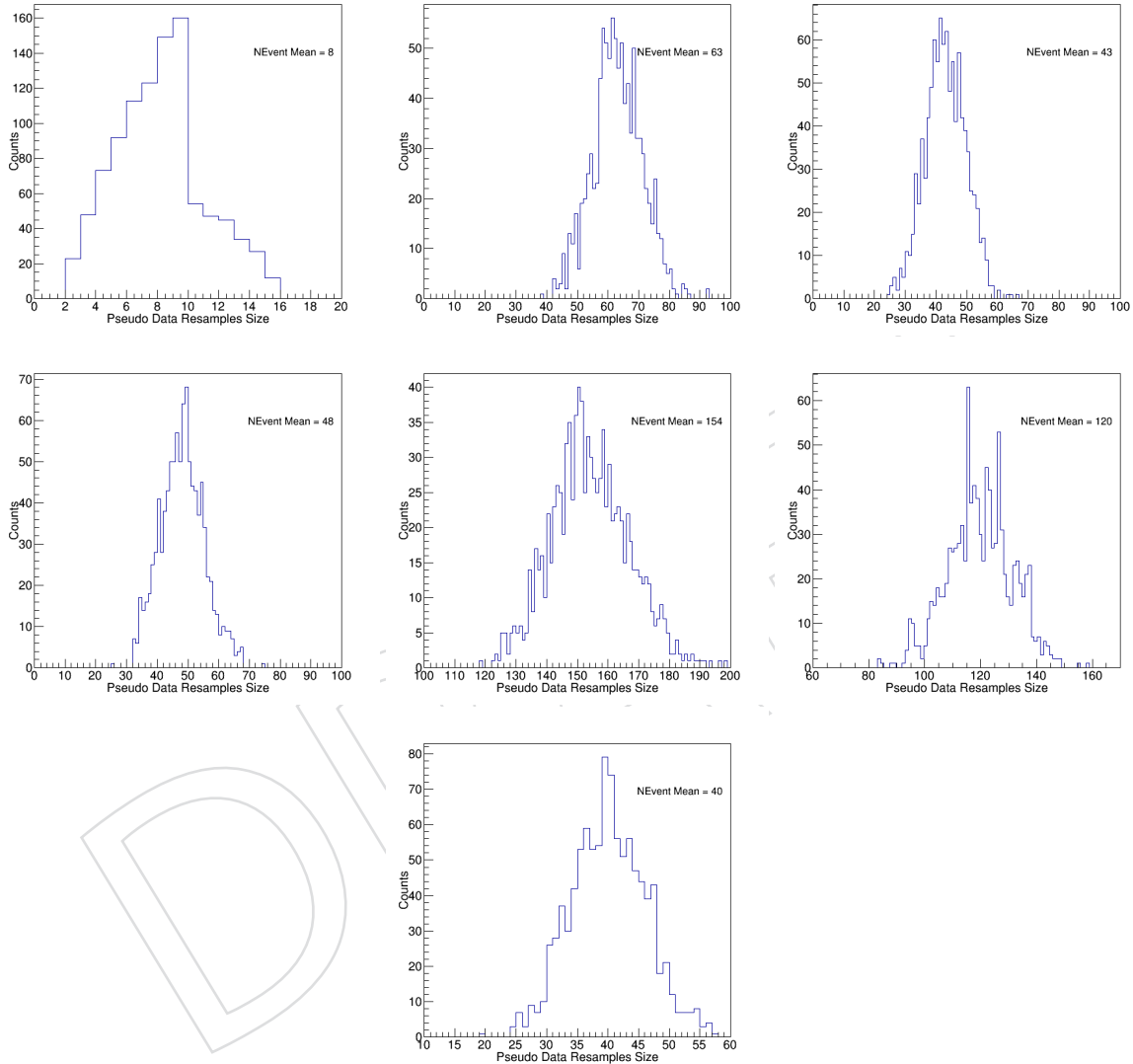


Figure 52: The number of reconstructed B_s candidates distributions of the data-like randomly resampled datasets for 0 - 90% at 7 - 10, 10 - 15, 15 - 20, and 20 - 50 GeV/c as well as 0 - 90%, 0 - 30%, and 30 - 90% are shown respectfully above.

654 We count the maximum percentage of reused events in each p_T and centrality bin resampled
 655 dataset as well as the maximum overall reused percentage among sum of the samples together.
 656 For maximum percentage of reused events, we count each reused events in each resample
 657 dataset and divide by the total event of that dataset. We select the largest number among all
 658 datasets. For the overall reused percentage among sum of the samples, we sum all the reused
 659 events as well as the total events for all 1000 samples, then we take the ratio between them and
 660 pick out the largest number. They are summarized on Table 16 below

Table 16: The maximum reused percentage for one single sample and all reused samples for all p_T and centrality bins are summarized below. The statistics for each bin is also reported.

Centrality	p_T (GeV/c)	Bin Statistics	Max Reused Percent (One)	Max Reused Percent (All)
0 - 90%	7 - 10	8	75%	9.46%
0 - 90%	10 - 15	63	12.5%	1.56%
0 - 90%	15 - 20	43	18.6%	2.14%
0 - 90%	20 - 50	48	17.6%	1.96%
0 - 90%	10 - 50	120	7.14%	0.88%
0 - 30%	10 - 50	40	18.8%	2.32%
30 - 90%	10 - 50	154	5.51%	0.67%

661 We can see that, the overall reused percentage is in general below 10% in all resampled datasets.
 662 For each event, it is possible to go up to 75% maximum among the total 1000 resampled
 663 datasets. But we know that this number will keep going up as we increase the total num-
 664 ber of resampled datasets. We believe that a better metric to quantify the reused percentage
 665 should be the overall reused percentage.

666 Next, we validate that our fits to extract the raw yield actually have good closure. The pull,
667 raw yield, raw yield error distribution are shown below in Figure 53 and Figure 54

DRAFT

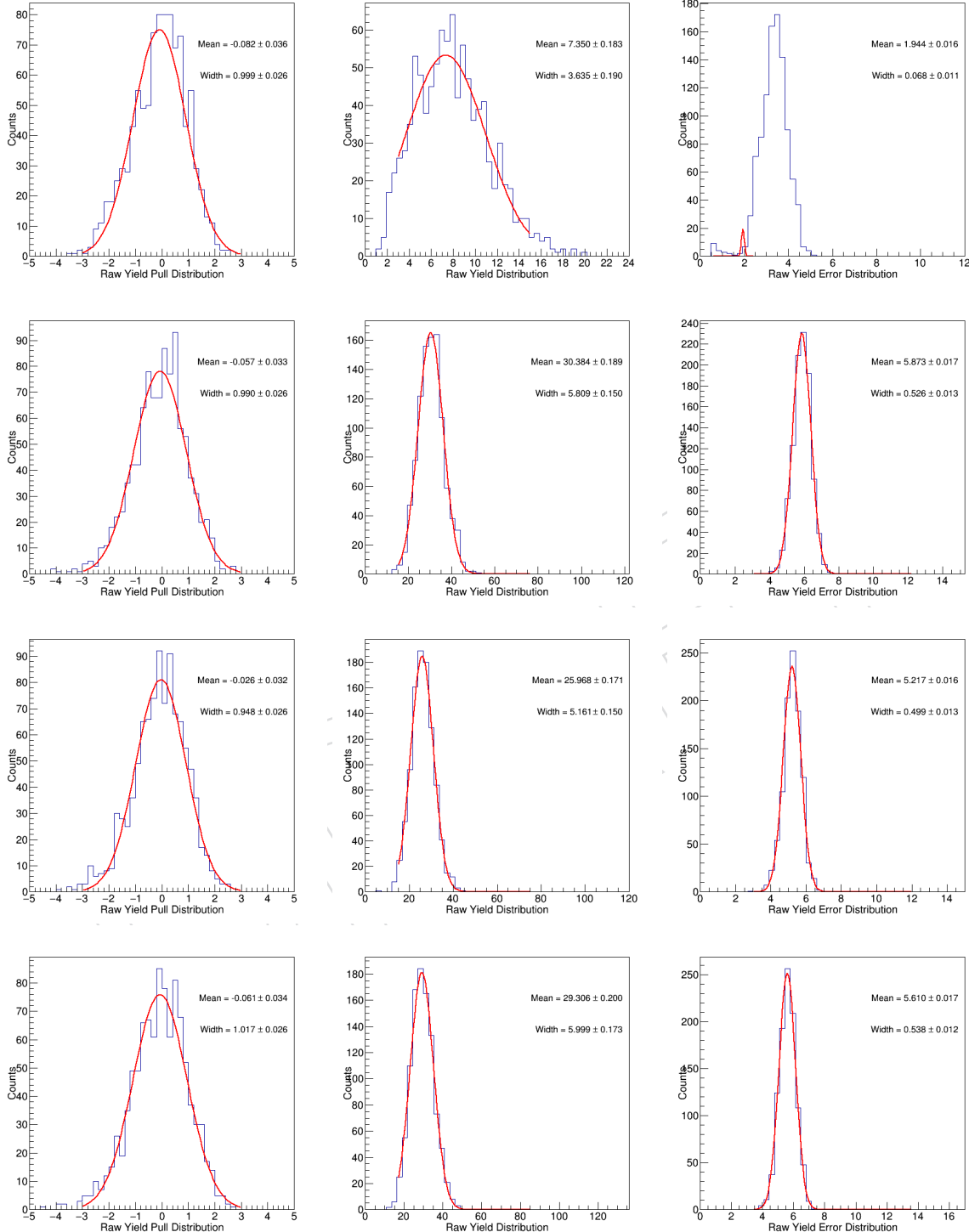


Figure 53: The raw yield pull, raw yield, and raw yield error distributions of the data-like randomly resampled datasets for 0 - 90% at 7 - 10, 10 - 15, 15 - 20, and 20 - 50 GeV/c are shown respectfully above.

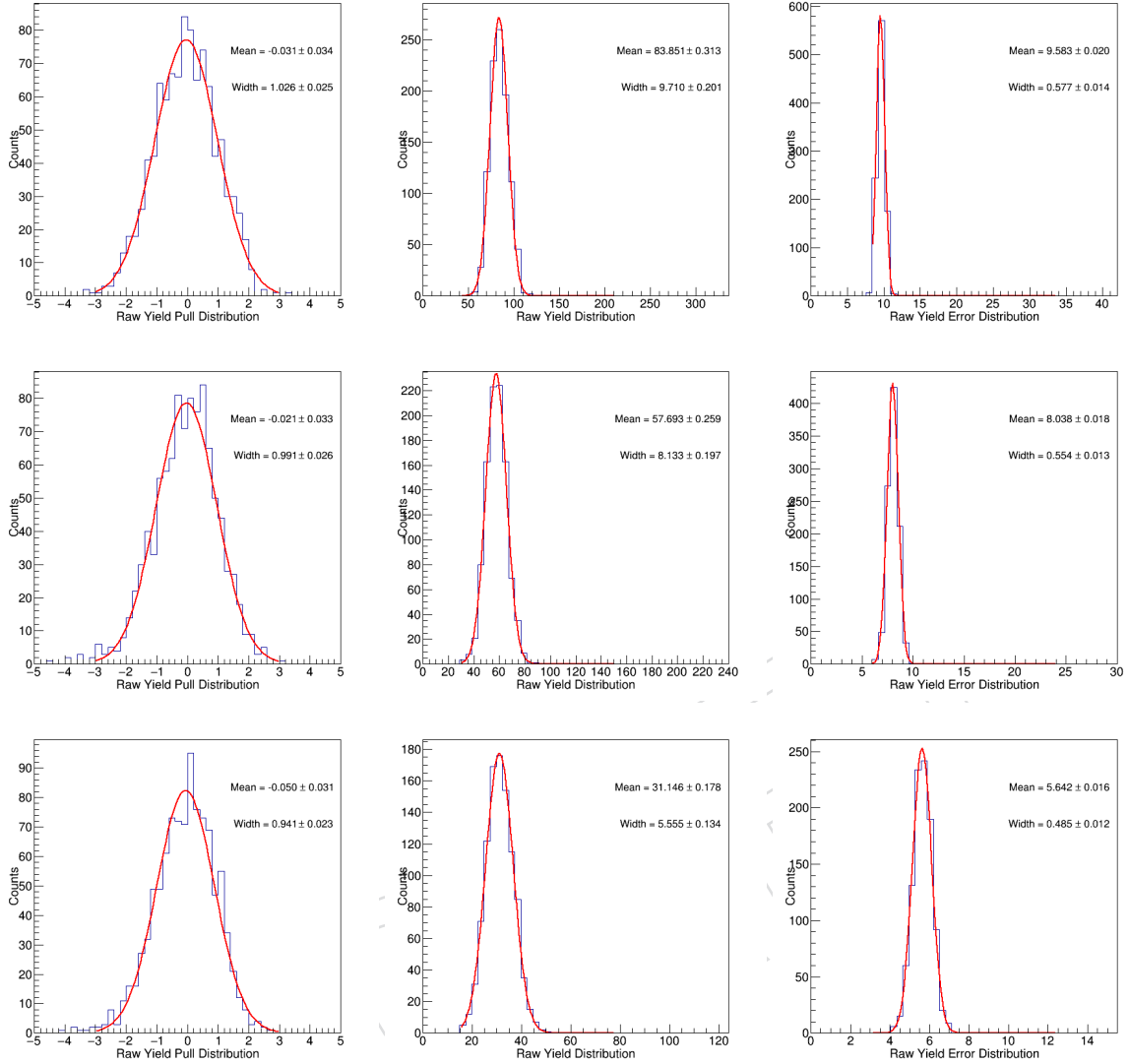


Figure 54: The raw yield pull, raw yield, and raw yield error distributions of the data-like randomly resampled datasets for 10 - 50 GeV/c at 0 - 90%, 0 - 30%, and 30 - 90% centrality are shown respectfully above.

668 Subsequently, we compare our raw yield results with the toy MC to see if they are consistent.
 669 We basically compare the raw yield and raw yield error in Figure 53 and Figure 54 to Figure 46
 670 and Figure 47. Table 17 shows the raw yield using this data resampling compared to the toy
 671 MC studies.

Table 17: The raw yields and their uncertainties using data resampling and toy MC studies are both summarized below.

Centrality	p_T (GeV/c)	Data Resampling Raw Yield	Toy MC Raw Yield
0 - 90%	7 - 10	8.6 ± 4.5	6.8 ± 4.0
0 - 90%	10 - 15	30.4 ± 5.8	26.9 ± 5.6
0 - 90%	15 - 20	26.0 ± 5.2	26.4 ± 5.2
0 - 90%	20 - 50	29.3 ± 6.0	31.0 ± 5.9
0 - 90%	10 - 50	83.9 ± 9.7	85.2 ± 9.8
0 - 30%	10 - 50	57.7 ± 8.1	59.4 ± 8.0
30 - 90%	10 - 50	31.1 ± 5.6	29.7 ± 5.6

672 From 17, we can see that the data resampling is consistent to the toy MC studies. We proceed to
 673 calculate the statistical uncertainties of the raw yield. Table 18 shows the statistical uncertain-
 674 ties from our calculations using data bootstrap method and compared it to the uncertainties to
 675 raw yield fit

Table 18: The RMS/Mean of the raw yield distribution are summarized above.

Centrality	p_T (GeV/c)	Raw Yield RMS/Mean Bootstrap	Raw Yield Error/Raw Yield from Fits
0 - 90%	7 - 10	52.3%	38.4%
0 - 90%	10 - 15	19.1%	20.8%
0 - 90%	15 - 20	20.0%	19.7%
0 - 90%	20 - 50	20.5%	18.4%
0 - 90%	10 - 50	11.6%	11.4%
0 - 30%	10 - 50	14.0%	14.3%
30 - 90%	10 - 50	18.0%	18.4%

676 Subsequently, we are able to get the efficiency correction factor $\langle \frac{1}{\alpha \times \epsilon} \rangle$ in Figure 55

Table 19: The RMS/Mean and the asymmetric up and down statistical uncertainties of the efficiency correction factor $\langle \frac{1}{\alpha \times \epsilon} \rangle$ distribution are summarized below.

Centrality	p_T (GeV/c)	RMS/Mean	Stat. Up (+)	Stat Down (-)
0 - 90%	7 - 10	32.8%	38.1%	33.5%
0 - 90%	10 - 15	12.2%	11.4%	12.1%
0 - 90%	15 - 20	6.7%	6.3%	6.9%
0 - 90%	20 - 50	6.1%	5.3%	5.5%
0 - 30%	10 - 50	14.6%	15.7%	12.8%
30 - 90%	10 - 50	10.5%	10.1%	9.70%
0 - 90%	10 - 50	12.8%	11.6%	12.4%

677 Then, our corrected yield distributions are shown in Figure 56 below

678 Finally, we calculate the RMS/Mean and the asymmetric up and down statistical uncertainties
 679 of the corrected yield distribution above for each p_T and centrality and quote them as our
 680 statistical uncertainties.

681 To calculate the asymmetric up and down statistical uncertainties, we first locate the bin of
 682 the mean of the corrected yield distribution. Then we integrate from the mean to up/down
 683 side by increasing/decreasing the bin number from the mean bin and take their ratio to the
 684 total up/down side counts from the mean until they reach one sigma, namely $34.14\% \times 2 =$
 685 68.28%. Then, we read out the corrected yield according to those bin number. Finally, we take
 686 the percentage uncertainties, which is defined as ratio of the deviation of one sigma corrected
 687 yield of up and down to the mean, and quote them as the asymmetric up and down statistical
 688 uncertainties.

689 Our results are summarized on the table 20 below:

690 We also compile the uncertainties on the raw yield, efficiency correction factor $\langle \frac{1}{\alpha \times \epsilon} \rangle$, and cor-
 691 rected yield of into Table 21 for cross check

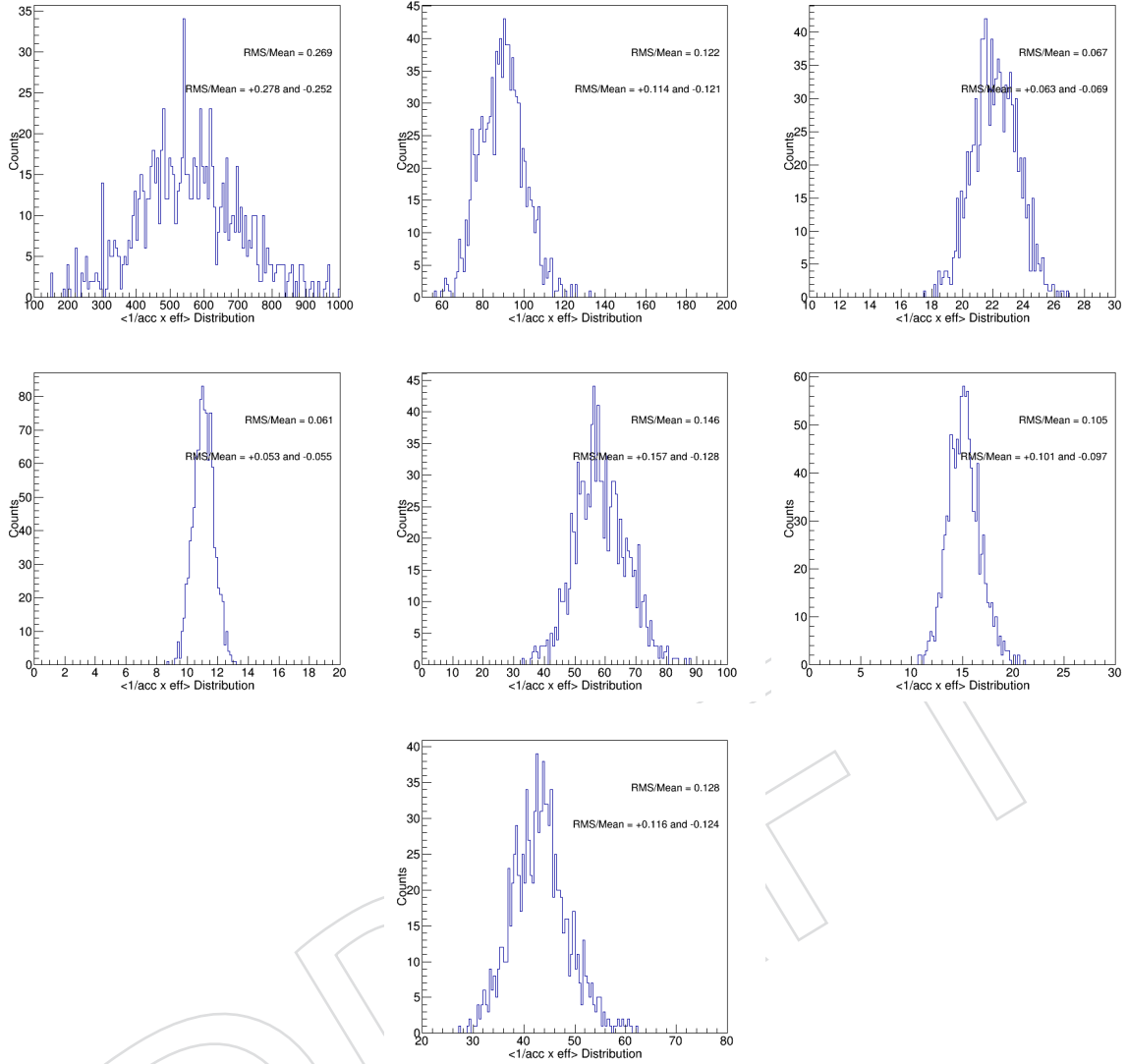


Figure 55: The efficiency correction factor $\langle \frac{1}{\alpha \times \epsilon} \rangle$ distributions of the data-like randomly resampled datasets for 0 - 90% at 7 - 10, 10 - 15, 15 - 20, and 20 - 50 GeV/c as well as 0 - 90%, 0 - 30%, and 30 - 90% are shown respectfully above.

692 Comparing the Table Tab. 20 with Table Tab. 18, we can see that the corrected yield has larger
 693 statistical uncertainties than the raw yield, which make sense since the efficiency correction
 694 also positively contribute to the statistical uncertainties to the corrected yield. Therefore, we
 695 hereby conclude our closure test. We will quote the results from Tab. 20 as the statistical uncer-
 696 tainties of our corrected yield and 15 as the systematic uncertainties due to the bias of efficiency
 697 correction for our data analysis. We have included them in our final results.

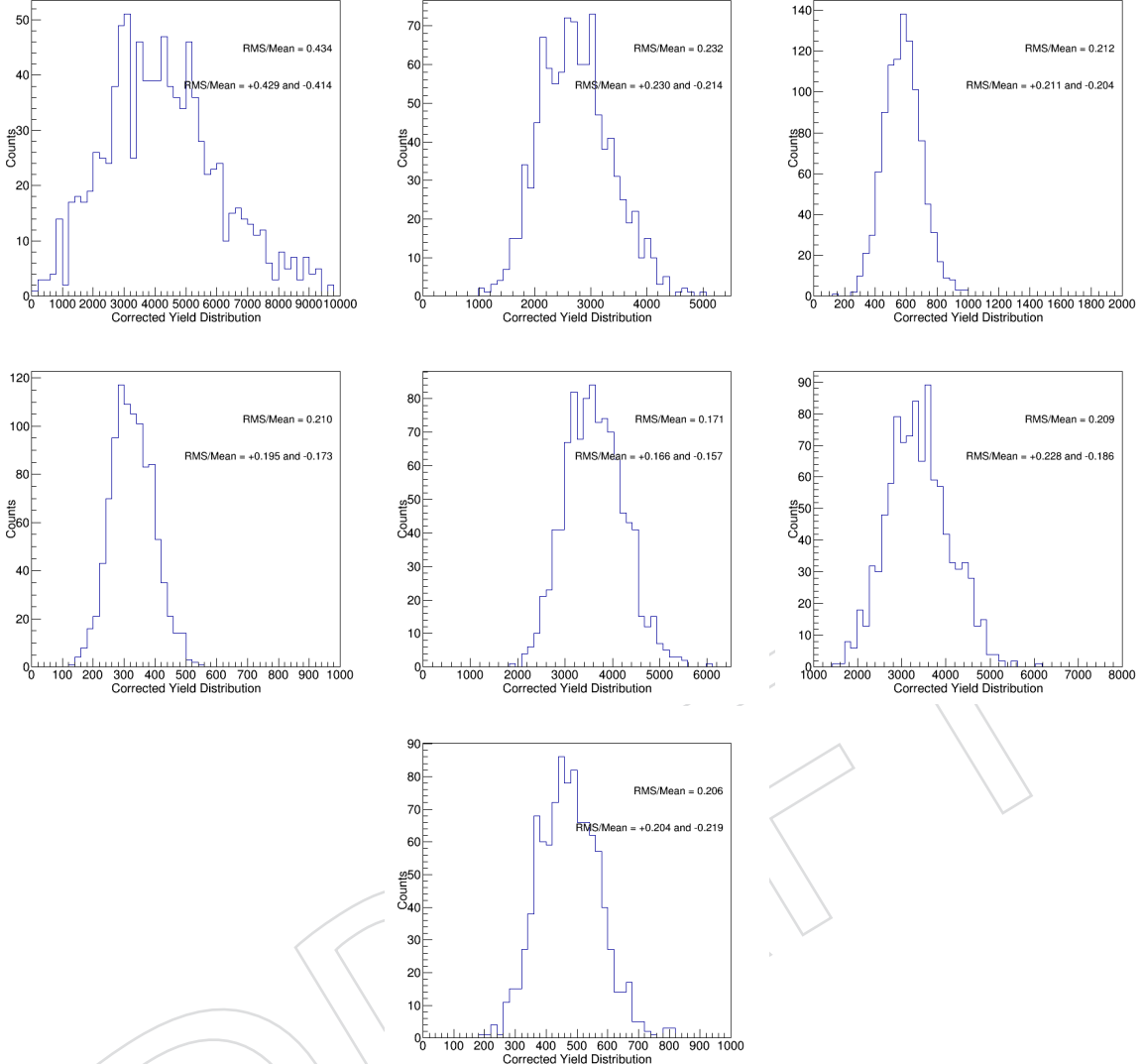


Figure 56: The corrected yield distributions of the data-like randomly resampled datasets for 0 - 90% at 7 - 10, 10 - 15, 15 - 20, and 20 - 50 GeV/c as well as 0 - 90%, 0 - 30%, and 30 - 90% are shown respectfully above.

Table 20: The RMS/Mean and the asymmetric up and down statistical uncertainties of the corrected yield distribution are summarized below.

Centrality	p_T (GeV/c)	RMS/Mean	Stat. Up (+)	Stat Down (-)
0 - 90%	7 - 10	43.4%	42.9%	41.4%
0 - 90%	10 - 15	23.2%	23.0%	21.4%
0 - 90%	15 - 20	21.2%	21.1%	20.4%
0 - 90%	20 - 50	21.0%	19.5%	17.3%
0 - 30%	10 - 50	20.9%	22.8%	18.6%
30 - 90%	10 - 50	20.6%	20.4%	21.9%
0 - 90%	10 - 50	17.1%	16.6%	15.7%

Table 21: The statistical uncertainties on raw yield, efficiency correction factor $\langle \frac{1}{\alpha \times \epsilon} \rangle$, and corrected yield distribution are summarized below for comparison.

Centrality	p_T (GeV/c)	Raw Yield	$\langle \frac{1}{\alpha \times \epsilon} \rangle$ Err (+)	$\langle \frac{1}{\alpha \times \epsilon} \rangle$ Err (-)	Corr. Err (+)	Corr. Yield Err (-)
0 - 90%	7 - 10	38.4%	27.7%	42.9%	25.2%	41.4%
0 - 90%	10 - 15	20.8%	11.4%	23.0%	12.1%	21.4%
0 - 90%	15 - 20	19.7%	6.3%	21.1%	6.9%	20.4%
0 - 90%	20 - 50	18.4%	5.3%	19.5%	5.5%	17.3%
0 - 30%	10 - 50	11.4%	15.7%	22.8%	12.8%	18.6%
30 - 90%	10 - 50	14.3%	10.1%	20.4%	9.70%	21.9%
0 - 90%	10 - 50	18.4%	11.6%	16.6%	12.4%	15.7%

698 9 Results

699 9.1 Number of minimum biased events evaluation

700 For the N_{events} which stands for the number of Minimum Biased events, and the same as number obtained in the B^+ corrected yield analysis in [17].

702 Since we are only using events centrality in 0 - 90% for our analysis, we will count total number
 703 of MB events within 0 - 90% centrality. The number of events we obtains is about $N_{events} = 11.1$
 704 billion for (0 - 90%) centrality from using the brilcal to evaluate the luminosity and process
 705 minimum bias PD0 with our muon JSON. We obtain the N_{MB} according to the formula below

$$706 N_{evt}^{MB} = \frac{N_{MB}^{\mu\mu json}}{\mathcal{L}_{MB trigger}^{\mu\mu json}} \mathcal{L}_{\mu\mu trigger}^{\mu\mu json} \quad (9)$$

706 The definition of the variables in the formula are as follows:

707 N_{evt}^{MB} : **The number of minimum bias events in dimuon PD with muon json.**

708 $N_{MB}^{\mu\mu json}$: **The number of event of all MB PDs with muon json.**

709 $\mathcal{L}_{MB}^{\mu\mu json}$: **The luminosity of all MB PDs with muon json.**

710 $\mathcal{L}_{\mu\mu trigger}^{\mu\mu json}$: **The luminosity of dimuon PD with muon json.**

711 To obtain the total number of minimum bias events, first we process one PD (PD5) minimum
 712 bias events and count the total number of events for centrality at 0 - 90% to obtain $N_{MB}^{\mu\mu json}$.
 713 Then, we run the brilcal for MB PD5 and sum the luminosity of HLT MB triggers:

714

715 Trigger 1: "HLT_HIMinimumBias_part0_v1"

716 Trigger 2: "HLT_HIMinimumBias_SinglePixelTrack_part0_v1"

717 Trigger 3: "HLT_HIMinimumBias_SinglePixelTrack_NpixBypass_part0_v1"

718 Trigger 4: "HLT_HIMinimumBias_SinglePixelTrack_NpixGated_part0_v1"

719 to obtain $\mathcal{L}_{MB}^{\mu\mu json}$, and

720 Trigger 5: "HLT_HIL3Mu0NHitQ10_L2Mu0_MAXdR3p5_M1to5_v1"

721 to obtain $\mathcal{L}_{MB}^{\mu\mu json}$.

722 Table 22 shows the luminosity of Trigger 1 – 5 above. The sum of trigger 1 – 4 will be $\mathcal{L}_{MB}^{\mu\mu json}$
 723 and trigger 5 will be $\mathcal{L}_{MB}^{\mu\mu json}$.

724 We have also obtained the number of events by processing one of the MB sample. The total
 725 number of events can be found in Table 23.

Table 22: Summary table of the luminosity of HLT triggers to obtain the number of minimum biased events.

HLT	Luminosity (μb^{-1})
HLT_HIMinimumBias_part0_v1	14.8269
'HLT_HIMinimumBias_SinglePixelTrack_part0_v1	1.3010
HLT_HIMinimumBias_SinglePixelTrack_NpixBypass_part0_v1	7.9468
HLT_HIMinimumBias_SinglePixelTrack_NpixGated_part0_v1	
Total	24.0748
HLT_HIL3Mu0NHitQ10_L2Mu0_MAXdR3p5_M1to5_v1	1657.1320

Table 23: Summary table of the total number of MB events vs centrality

Centrality	$\mathcal{L}_{\mu\mu trigger}^{\mu\mu json}$
0-10%	18276069
10-20%	17680482
20-30%	17687566
30-40%	17684913
40-50%	17685909
50-60%	17680807
60-70%	17686640
70-80%	18375623
80-90%	18749965
0-30%	53644117
30-90%	107863857
0-90%	161507974

726 For 0 - 90%, it is 161507974. The number of events can then be computed as follows:

$$N_{evt}^{MB} = \frac{N_{MB}^{\mu\mu json}}{\mathcal{L}_{MBtrigger}^{\mu\mu json}} \mathcal{L}_{\mu trigger}^{\mu\mu json} = \frac{1657.1320 \mu b^{-1}}{24.0748 \mu b^{-1}} \times 161507974 = 1.1823737719 \times 10^{10} \simeq 11.823737719 \text{ billion}$$
(10)

727 Hence, the number of minimum biased event $N_{MB} = 11.823737719$ billion.

728 We compile a table for the number of minimum biased events N_{MB} in 0 - 30%, 30% - 90%, and 0
729 - 90% Table 24.

Table 24: Summary table of the total number of MB events vs centrality

Centrality	N_{MB} (billion)
0-30%	3.941
30-90%	7.882
0-90%	11.82

730 The presentation for N_{MB} calculations can also be found in the presentation at https://twiki.cern.ch/twiki/pub/CMS/HiSpectra2019/20191015_MBcounting_MITMeeting.pdf.

733 The uncertainties of N_{MB} estimation can be found in the systematic subsection “Systematic
734 Uncertainties on the Number of Events Counting”.

735 9.2 dN/d p_T in PbPb collisions at 5.02 TeV

736 The dN/d p_T in PbPb collisions is defined as:

$$\frac{1}{T_{AA}} \frac{dN}{dp_T} \Big|_{|y|<2.4} = \frac{1}{T_{AA}} \frac{1}{2} \frac{1}{\Delta p_T} \frac{1}{BR \cdot N_{MB}} N_{B_s^0}^{\Big|_{|y|<2.4}} \langle \frac{1}{\alpha \times \epsilon} \rangle$$
(11)

737 The detailed number of number of MB event normalized corrected yield vs p_T and centrality
738 measured in PbPb collision for B_s^0 and B^+ can be found in Table. 25, Table. 26, Table. 27, and
739 Table. 28.

Table 25: Summary table of B_s^0 corrected yield for different p_T bins

Corrected yield (pb GeV $^{-1}$ c)	mean value	stat. up (+)	stat. down (-)	syst. up (+)	syst. down (-)
(7,10)	206848	42.9%	41.4%	51.08%	49.10%
(10,15)	79349	23.0%	21.4%	16.22%	15.53%
(15,20)	23079	21.1%	20.4%	13.20%	13.05%
(20,50)	2349	21.0%	19.5%	16.34%	16.22%

740 9.3 B_s^0 to B^+ corrected yield ratio

741 In Fig. 59, the ratio between the B_s^0 corrected yield obtained above and the B^+ corrected yield
742 calculated in [11] is presented, in function of p_T . The same ratios are shown in Fig. 60, now

Table 26: Summary table of B^+ corrected yield for different p_T bins

Corrected yield (pb GeV $^{-1}$ c)	mean value	stat. up (+)	stat. down (-)	syst. up (+)	syst. down (-)
(7,10)	337744	23.4%	24.0%	19.80%	19.14%
(10,15)	258447	7.58%	8.54%	18.14%	17.96%
(15,20)	61634	7.30%	10.00%	9.23%	9.01%
(20,50)	7454	5.50%	8.56%	8.44%	8.28%

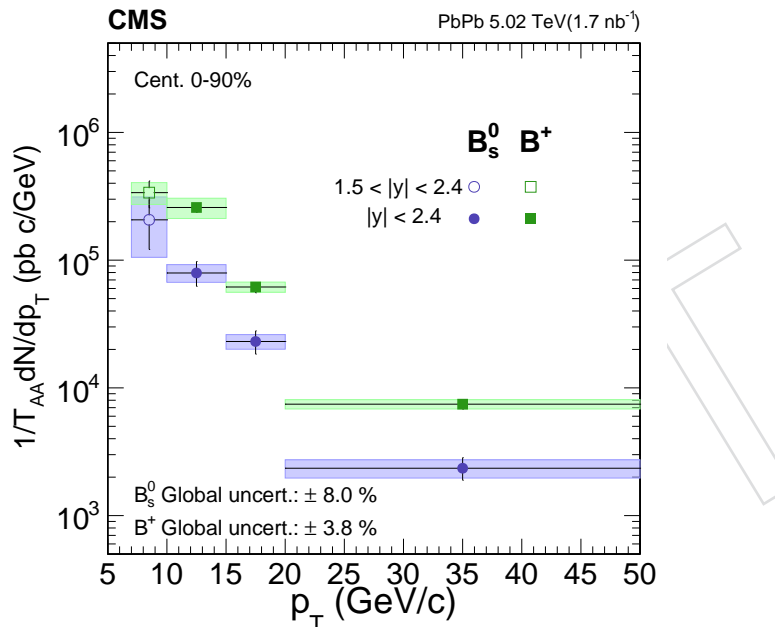
Table 27: Summary table of B_s^0 corrected yield for different centrality bins

Corrected yield (pb)	mean value	stat. up (+)	stat. down (-)	syst.. up (+)	syst. down (-)
0 - 30%	627470	22.8%	18.6%	16.7%	15.9%
30% - 90%	465295	20.3%	21.9%	13.5%	13.2%
0 - 90%	602714	16.6%	15.7%	14.3%	13.7%

743 for different centrality bins. The global uncertainties such as luminosity or T_{AA} uncertainty
 744 cancelled between the two analyses. The statistical uncertainty (the blue line in Fig. 60, and the
 745 green line in Fig. 60) are the quadratic sum of the B_s^0 and B^+ corrected yield statistical uncertain-
 746 ties. For the systematic uncertainty, we consider the ones related to tag and probe and tracking
 747 efficiency to be canceled between the two analyses. The rest of the systematic uncertainties are
 748 then again the quadratic sum of the B_s^0 and B^+ corrected yield analyses. In Tables 29 and 30
 749 detailed values of the corrected yield ratios vs p_T and centrality, respectively, are shown.

Table 28: Summary table of B^+ corrected yield for different centrality bins

Corrected yield (pb)	mean value	stat. up (+)	stat. down (-)	syst.. up (+)	syst. down (-)
0% - 30%	1686360	8.03%	8.89%	16.0%	15.9%
30% - 90%	2169610	11.6%	11.4%	12.7%	12.5%
0 - 90%	1855170	8.85%	7.95%	14.1%	13.9%

Figure 57: T_{AA} scaled PbPb corrected yield vs p_T Table 29: Summary table of B_s^0/B^+ corrected yield ratio vs p_T

B_s^0/B^+ yield ratio	mean value	stat. up (+)	stat. down (-)	syst. up (+)	syst. down (-)
(7,10)	0.6124	48.9%	47.9%	49.9%	49.5%
(10,15)	0.3070	24.2%	23.0%	19.1%	19.0%
(15,20)	0.3744	22.3%	22.7%	9.42%	9.42%
(20,50)	0.3151	21.7%	21.3%	12.9%	12.9%

Table 30: Summary table of B_s^0/B^+ corrected yield ratio vs centrality

B_s^0/B^+ yield ratio	mean value	stat. up (+)	stat. down (-)	syst. up (+)	syst. down (-)
0 - 30%	0.3721	24.1%	20.6%	17.4%	17.3%
30 - 90%	0.2145	23.4%	24.7%	10.9%	10.8%
0 - 90%	0.3249	18.8%	17.6%	13.4%	13.3%

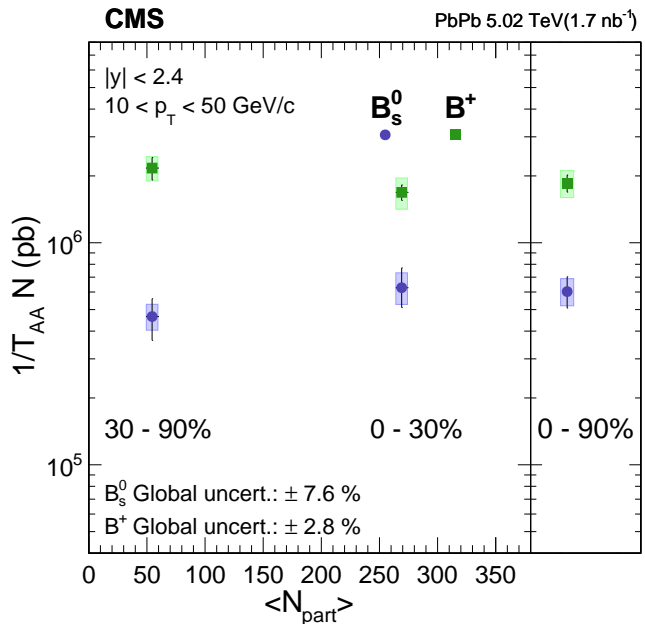


Figure 58: T_{AA} scaled PbPb corrected yield vs centrality for 0 - 30%, 30% - 90 % and inclusive 0 - 90%

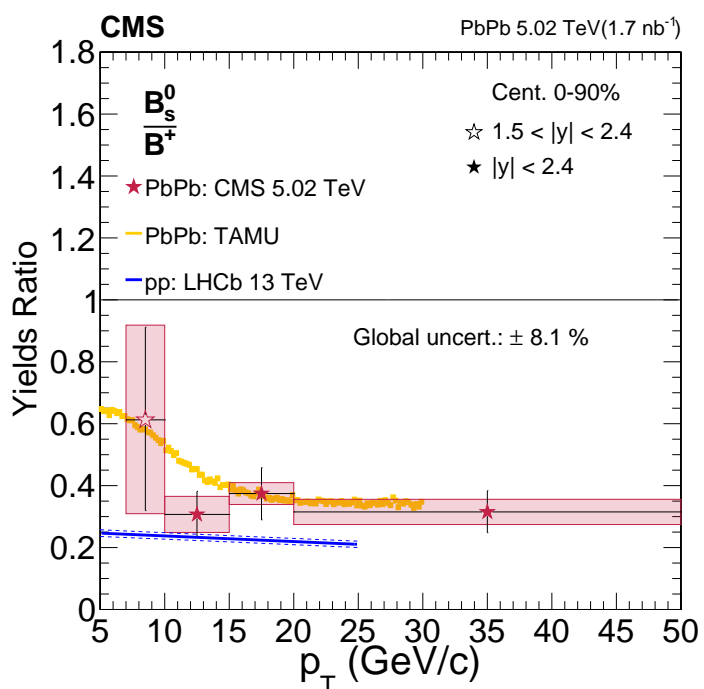


Figure 59: The corrected yield ratio between B_s^0 and B^+ measured in PbPb collisions at $\sqrt{s_{\text{NN}}} = 5.02 \text{ TeV}$ from 7 to 50 GeV/c and the comparison with the PDG (green band) and LHCb (blue data points) references

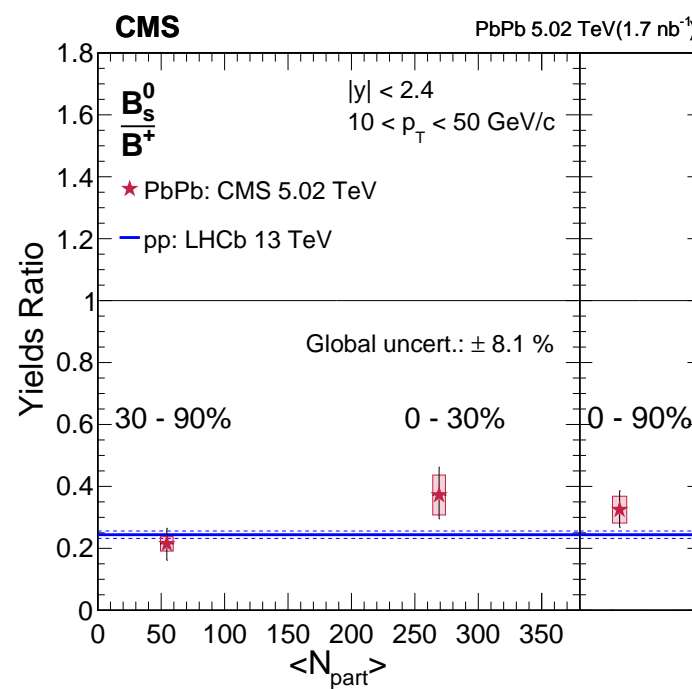


Figure 60: The corrected yield ratio between B_s^0 and B^+ measured in PbPb collisions at $\sqrt{s_{\text{NN}}} = 5.02 \text{ TeV}$ from centrality 0-30% (left), 30%-90% (middle), and the inclusive 0-90% (right)

750 10 Systematic uncertainties

751 10.1 Number of minimum biased events

752 We estimate the systematic uncertainties on the number of events counting. We consult the
 753 global observable group. The uncertainties come from two sources. The first one is from trigger
 754 and event selections. The details are provided by the global observable group and can be found
 755 in the following link:

756 https://twiki.cern.ch/twiki/bin/view/CMSPublic/SWGuideHeavyIonCentrality?redirectedfrom=CMS.SWGuideHeavyIonCentrality#PbPb_Data_2018_AN1

758 The percentage uncertainties on number of minimum biased events is about 136669812/11536000857
 759 = 1.18%

760 The second one is the event centrality definition when we select events of centrality classes 0 -
 761 30%, 30 - 90%, and 0 -90% according to the header. Again, the information can be found on the
 762 link above in the section "Centrality tables". We use the nominal hiHF edge bin as the nominal
 763 centrality definition to count the number of minimum biased events and quote the percentage
 764 deviation when using the systematic (up) and systematic (down) header. Table 31 shows the
 765 print out number of trigger pre-scale corrected events with different centrality headers

Table 31: Number of trigger pre-scale corrected events with different centrality headers are shown above.

Centrality	Nominal	Syst Up Header	Syst Down Header
0 - 10%	1282973828	1274718281	1290760749
10 - 20%	1283710705	1275442651	1291376572
20 - 30%	1284093587	1275999858	1291788730
30 - 40%	1283347661	1274840164	1291318905
40 - 50%	1283473360	1275407587	1290992844
50 - 60%	1283421647	1277418428	1291307883
60 - 70%	1283773186	1317413703	1291531187
70 - 80%	1333927036	1345854407	1291735521
80 - 90%	1365082200	1365760639	1353810118
90 - 100%	790269039	791216531	789449740
0 - 30%	3850778120	3826160790	3873926051
30 - 90%	7833025090	7856694928	7810696458
0 - 90%	11683803210	11682855718	11684622509

766 Adding the events from 0 - 30%, 30 - 90%, and 0 -90% and obtain the percentage difference
 767 between the up and down to the nominal as the systematic uncertainties. For 0 - 30%, the sys-
 768 tematic uncertainty is +0.601% and -0.639%; for 30 - 90%, the systematic uncertainty is +0.302%
 769 and -0.285%; for 0 - 90%, the systematic uncertainty is +0.07% and -0.08%.

770 Combining these two uncorrelated uncertainties, we obtain the final uncertainties as shown on
 771 the summary table 50 below.

772 10.2 Branching ratio

773 The systematic uncertainty on the branching ratio of the decay $B_s^0 \rightarrow J/\psi \phi$, with $J/\psi \rightarrow \mu^+ \mu^-$
 774 and $\phi \rightarrow K^+ K^-$, is calculated by adding in quadrature the uncertainties on each sub-channel.
 775 The resulting uncertainty for the full decay chain is 7.60% [12].

776 **10.3 Tracking efficiency**

777 The systematic uncertainties related to tracking efficiency or track reconstruction can be eval-
 778 uated based on the method described in the D meson analysis [3]. The strategy was to re-
 779 construct the D^* meson in both 3 and 5 prong decay channel and by correcting for the BR
 780 difference, the tracking efficiency to be obtained in data. For now, a conservative uncertainty
 781 of 5% per track is being considered. Therefore, for $B_s^0 \rightarrow \mu^+ \mu^- K^+ K^-$, we have two tracks and
 782 the tracking uncertainty will be about 10.0%.

783 **10.4 Muon efficiency: Tag and Probe**

784 The Tag and Probe (TnP) study for 2018 PbPb collisions is worked out by the Dilepton group.
 785 We used their head file results in our TnP systematic uncertainties studies.

786 We calculate the efficiency of muon trigger, tracking, and identification selections and quote
 787 unity ratio to their centrality value as the the scaling factor. We then directly multiply the 2D
 788 scaling factor map in Figure 33 to the efficiency calculations to correct the nominal efficiency.
 789 We then vary the scale factor by 1 + the upper bound TnP fractional uncertainties and 1 - the
 790 lower bound TnP fractional uncertainties to our entire analysis work flow. We then compare
 791 the $\langle \frac{1}{\alpha \times \epsilon} \rangle$ for both cases to the nominal results. We take the ratio between the 1 + the upper
 792 bound TnP fractional uncertainties and 1 - the lower bound TnP fractional uncertainties cases
 793 to the nominal results and quote the deviation from unity as the TnP systematic uncertainties.
 794 The results are shown on Figure 63 and 64 and Table 32 and 34.

795 Basically, we have taken into account the muon identification (denoted: muid), tracking (de-
 796 noted: trk), and triggering (denoted: trg). To calculate the scale factor, we apply the B meson
 797 optimal selection with the , PVz, and centrality reweighting implemented on the B meson can-
 798 didates. We have the nominal as well as the up and down with 1 sigma of the combined
 799 statistics and systematics value for each of the 3 scale factor according to the dilepton header
 800 file. Then, we individually apply these correction on the $\langle \frac{1}{\alpha \times \epsilon} \rangle$ for p_T (Figure 61) and centrality
 801 (Figure 62) are shown below:

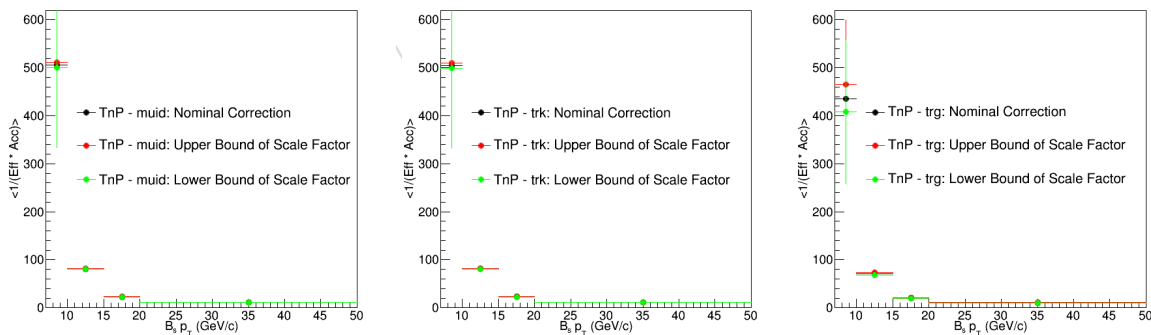


Figure 61: The $\langle \frac{1}{\alpha \times \epsilon} \rangle$ vs p_T with muon identification correction only (left), muon tracking only (middle), and muon trigger only (right) are shown above.

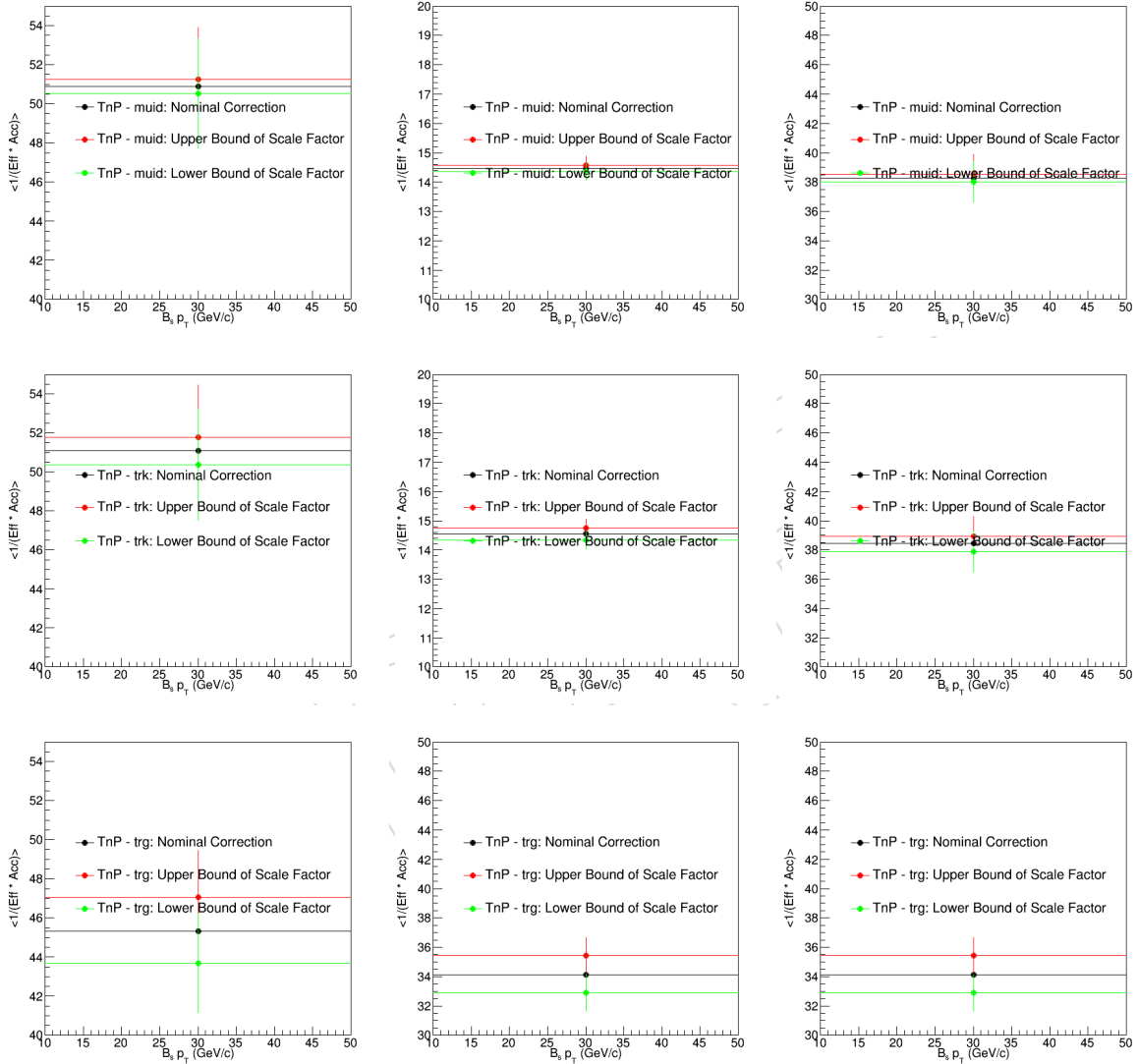


Figure 62: The $\langle \frac{1}{\alpha \times \epsilon} \rangle$ vs centrality in 0 - 30% (top), 30% - 90% (middle), 0 - 90% (bottom) with muon identification correction only (left), muon tracking only (middle), and muon trigger only (right) are shown above.

802 Then, the total nominal scale factor (central value) used in the analysis is given by the product
 803 of the 3 corrections: $total = muid \times trk \times trg$. The total scaling factor up and down uncertainties
 804 are added by their total up and down into quadrature: $\frac{\sigma_{total}}{total} = \sqrt{(\frac{\sigma_{muid}}{muid})^2 + (\frac{\sigma_{trk}}{trk})^2 + (\frac{\sigma_{trg}}{trg})^2}$. Our
 805 results for p_T and centrality are shown in Figure 63:

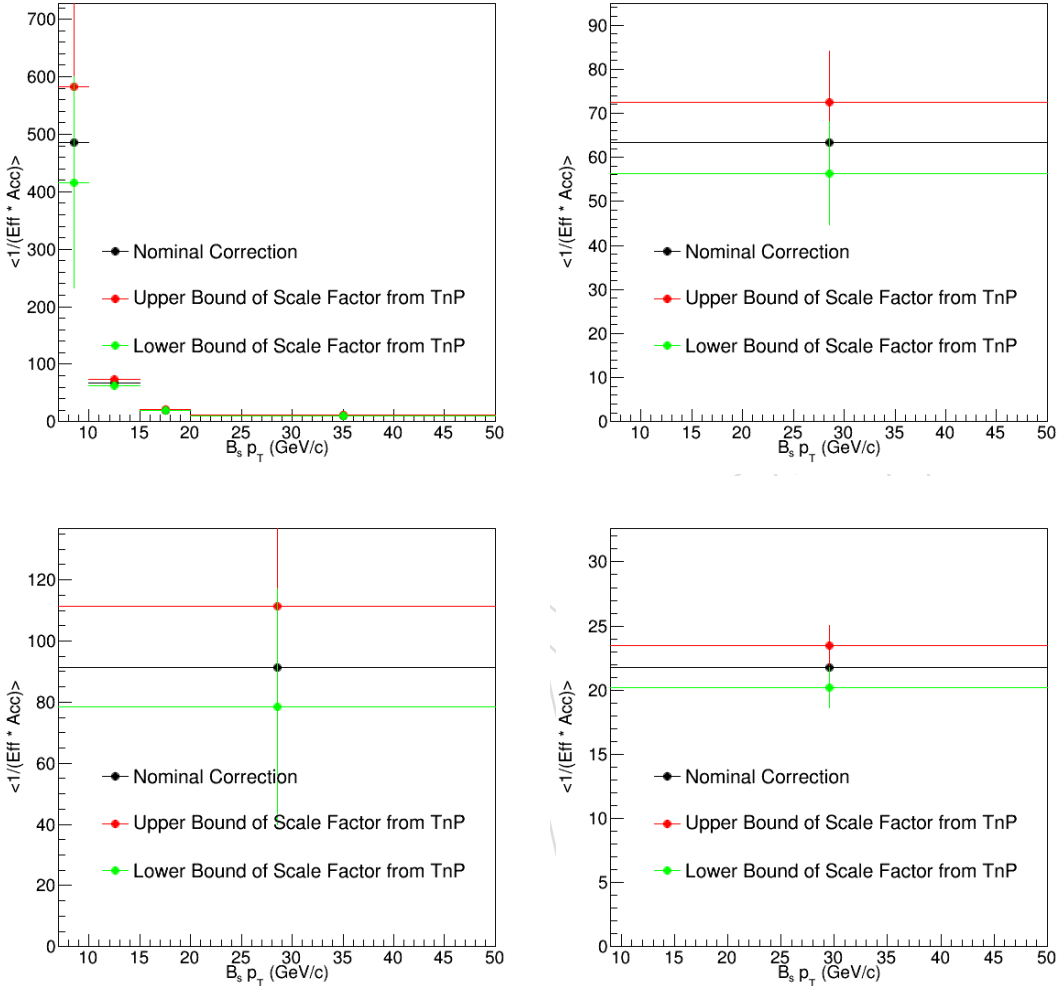


Figure 63: The comparison of the nominal to upper and lower bound $\langle \frac{1}{\alpha \times \epsilon} \rangle$ from TnP scale factor variation vs p_T (top left) and centrality at 0 -90% (top right), 0 -30% (bottom left), and 30 - 90% (bottom right) are shown above.

806 Finally, as stated previously, we quote the percentage deviation of the up and down varied
 807 scale factor with respect to the nominal scale factor as the tag and probe (TnP) systematic un-
 808 certainties. The results are shown below in Figure 64:

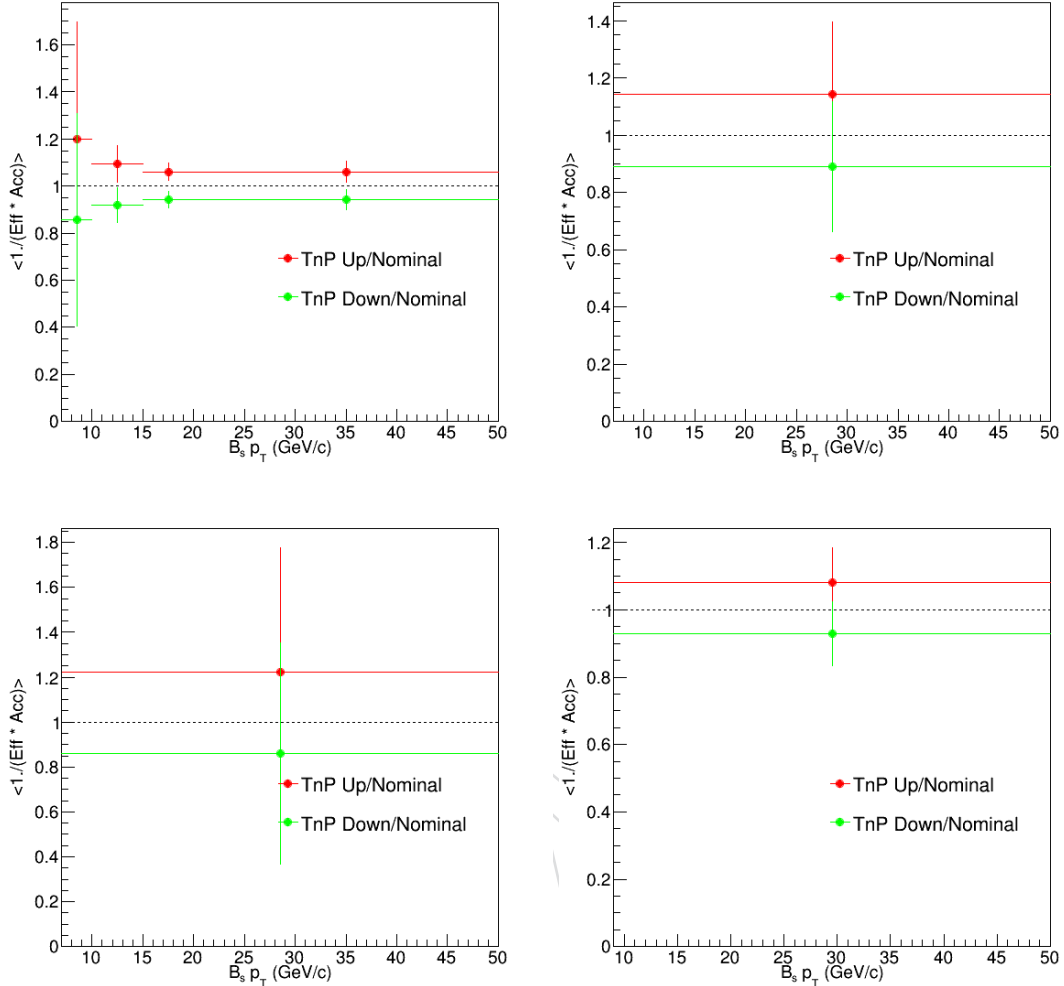


Figure 64: The ratio of upper and lower bound $\langle \frac{1}{\alpha \times \epsilon} \rangle$ to nominal vs p_T (top left) and centrality at 0 -90% (top right), 0 -30% (bottom left), and 30 - 90% (bottom right) and their comparisons to unity are shown above. We quote their deviation from unity as the TnP systematic uncertainties.

p_T (GeV/c)	5 - 10	10 - 15	15 - 20	20 - 50
TnP Systematics Upper Bound (+)	20.0%	9.34 %	6.01%	6.05%
TnP Systematics Lower Bound (-)	14.2%	8.08%	5.68%	5.73%

Table 32: The scaling factor and Tag and Probe systematics uncertainties for all four p_T bins are shown above.

Centrality	0 - 30%	30% - 90%	0 - 90%
TnP Systematics Upper Bound (+)	9.13%	7.23%	7.37%
TnP Systematics Lower Bound (-)	7.77%	6.64%	8.36%

Table 33: The scaling factor and Tag and Probe systematics uncertainties at 0 - 30%, 30% - 90%, and 0 - 90% centrality are shown above.

Centrality	0-30%	30-90%	0-90%
TnP Systematics	5.63%	5.31%	5.75%

Table 34: Tag and Probe systematics uncertainties for all three centrality bins are shown above.

10.5 Selection efficiency

10.5.1 Overview

An imperfect agreement between the kinematic variables distributions of B_s^0 signal in data and MC simulation can introduce a bias in the efficiency estimation and thus in the cross section measurement. In addition, the unknown information about the $B_s^0 p_T$ shape and the limited statistics of the MC can potentially introduce systematic uncertainties to our event-by-event weighting strategies for efficiency correction. In order to estimate the systematic uncertainties related to this, we have evaluated the systematic uncertainties in the following 2 subsections individual and compare their significance to the overall selection efficiency systematic uncertainties. The studies on the residue effect of p_T shape systematics is presented on Section 10.7.

10.5.2 Systematics Associated with Data-MC Disagreement

Again, the Data and MC have imperfect agreement with each other. To estimate this effect in efficiency correction, we create a weight from the Data/MC ratio using sPlot techniques. The details of the detail analysis are given in the reference [16]. From the analysis, we obtain files for there Data/MC weighting factors of different kinematic variables as well as BDT.

Since the variables we use for B meson reconstruction are BDT scores in several p_T ranges, it is most desirable to use Splot weights for the BDT variables to weight the MC. However, since B_s^0 has rather limited statistics, it is not feasible to implement BDT Splot weights with enough number of BDT binning. This may entail too conservative estimation of systematics. To use the BDT score from the sPlot, as a prerequisite, we check the correlations between the BDT variables with the signal extraction variable, namely, Bmass. Figure 65 below shows the correlations matrices between the BDT variables with Bmass in the range of 7 - 50 GeV/c for the data and MC:

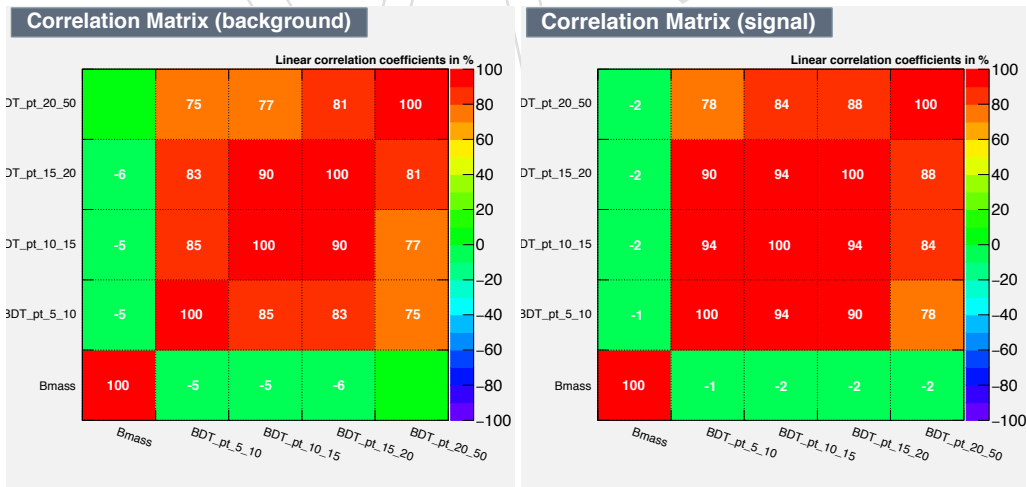


Figure 65: The plots above show the correlations matrices of the BDT at 5 - 10, 10 - 15, 15 - 20, 20 - 50 GeV/c to B_s mass of data (left) and MC (right).

As we can see, there is no significant correlations between the BDT variables and Bmass. This

833 not only shows that our BDT cuts are unbiased, but also confirms the validity of the sPlot
834 techniques by applying the BDT scores to the efficiency as variation to evaluate the systematic
835 uncertainties.

836 To deal with this issue, we examined B^+ track variable distributions instead. We use dimuon
837 and two tracks to reconstruct B_s^0 , whereas we use dimuon and one track to reconstruct B^+ .
838 Thus there is only difference in track in terms of kinematics. If we assume that the dimuon
839 distributions will be similar in both mesons, by giving weight to B^+ in terms of track variables'
840 Splot weights with much larger statistics, we can claim that the difference in B^+ data/MC in
841 track variables will be of the same order of that of B_s^0 .

842 We again loop through the candidate as what we have done in Section 7 and include the track
843 variable weight of each MC candidate as a reference and no weight as our nominal result. Then
844 we can create two 2D $\frac{1}{\alpha \times \epsilon}$ vs $B p_T$ and $B |y|$ with and without weight. Then we go through
845 the same work flow as the Section 7 to obtain the BDT weighted and unweighted (nominal)
846 efficiency. Then we compare the weighted and unweighted (nominal) $\langle \frac{1}{\alpha \times \epsilon} \rangle$ vs $B p_T$. We quote
847 the deviation from unity of ratio between weighted and unweighted $\langle \frac{1}{\alpha \times \epsilon} \rangle$ as the systematics
848 uncertainties associated with each variable. There are 7 track variables used in this estimation.
849 We applied weight to the MC for each variable, and then quote the maximum deviation among
850 them as our final systematics.

851 The comparison plots of $\langle \frac{1}{\alpha \times \epsilon} \rangle$ for the 7 track weights in differential p_T are shown in Figure 66
852 below. The inclusive p_T plots are shown in section B.1.

DRAFT

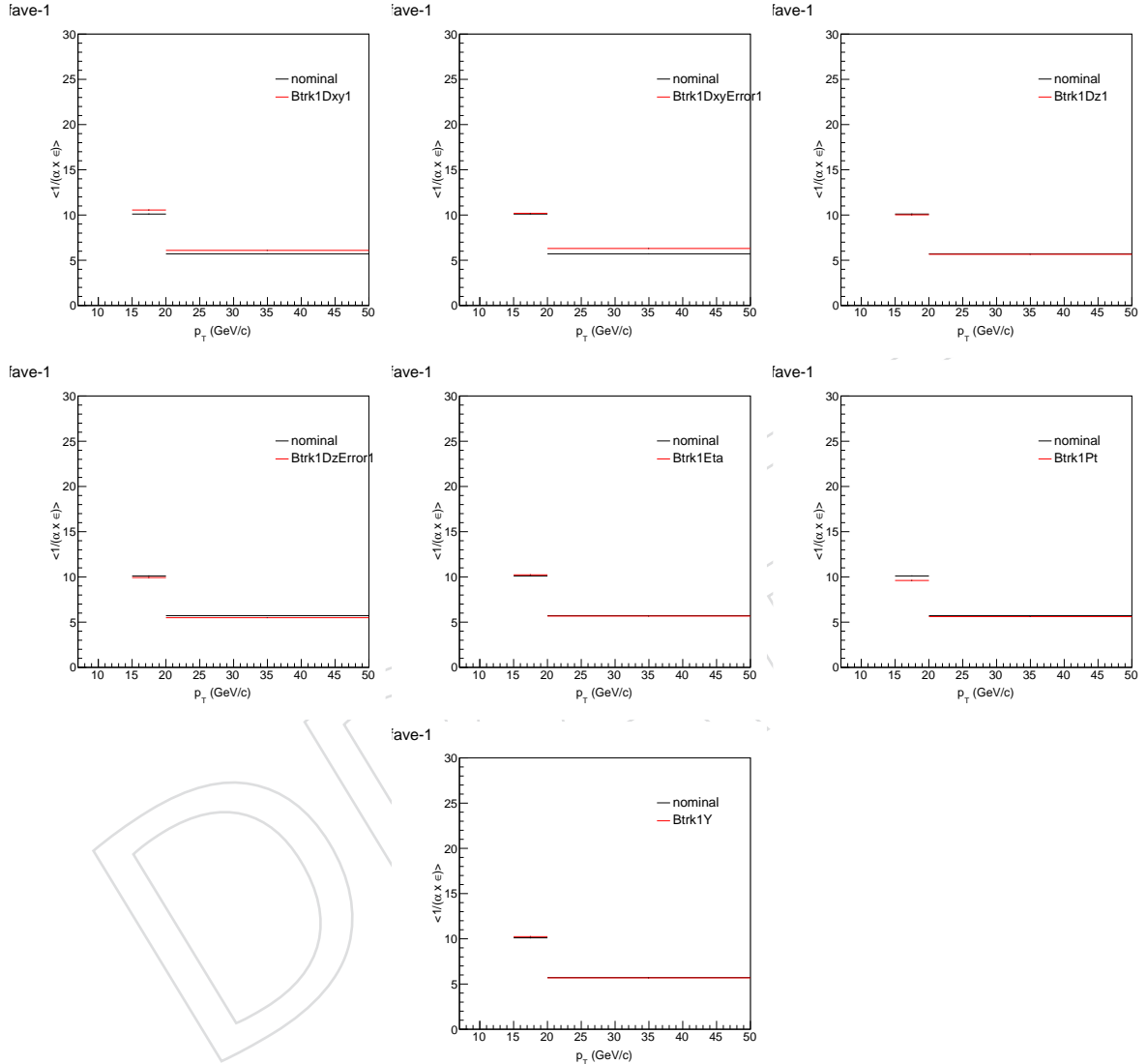


Figure 66: Track variable weighted and unweighted $\langle \frac{1}{\alpha \times \epsilon} \rangle$ comparison for 0 - 90% differential p_T . From left to right, top to bottom, the variables used are Btrk1Dxy1, Btrk1DxyError1, Btrk1Dz1, Btrk1DzError1, Btrk1Eta, Btrk1Pt, Btrk1Y, respectively.

853 The numerical results are summarize on Table 35 and Table 36

Table 35: Selection efficiency systematics by examination on B^+ track variables in differential p_T . Note that the quoted values are the maxima among 7 track variables used.

p_T	Selection efficiency systematics (B^+ track variable)
(7,10)	34.72%
(10,15)	4.74%
(15,20)	4.96%
(20,50)	10.36%

Table 36: Selection efficiency systematics by examination on B^+ track variables in inclusive p_T . Note that the quoted values are the maxima among 7 track variables used.

Centrality	Selection efficiency systematics (B^+ track variable)
(0, 30%)	2.26%
(30%, 90%)	3.04%
(0, 90%)	1.81%

854 10.5.3 Systematics Associated with MC Statistics

855 Due to the limited statistics of our MC, in the 2D finely binned $\frac{1}{\alpha \times \epsilon}$ vs $B p_T$ and $B |y|$ map,
 856 we will may introduce systematic uncertainties. To evaluate the systematic uncertainties, we
 857 generate 10k $\frac{1}{\alpha \times \epsilon}$ vs $B p_T$ and $B |y|$ maps by smearing each entry inside the nominal $\frac{1}{\alpha \times \epsilon}$ vs $B p_T$
 858 and $B |y|$ map with random Gaussian toy generation. The mean of the Gaussian is the central
 859 value of $\frac{1}{\alpha \times \epsilon}$ and the width is the error of $\frac{1}{\alpha \times \epsilon}$. We then calculate the $\langle \frac{1}{\alpha \times \epsilon} \rangle$ 10k trials and plot
 860 their distribution. We quote the RMS/mean as the systematic uncertainty due to the limited
 861 MC statistics. The acceptance, selection efficiency, and their product are shown on the Figure
 862 67 and 68 respectfully

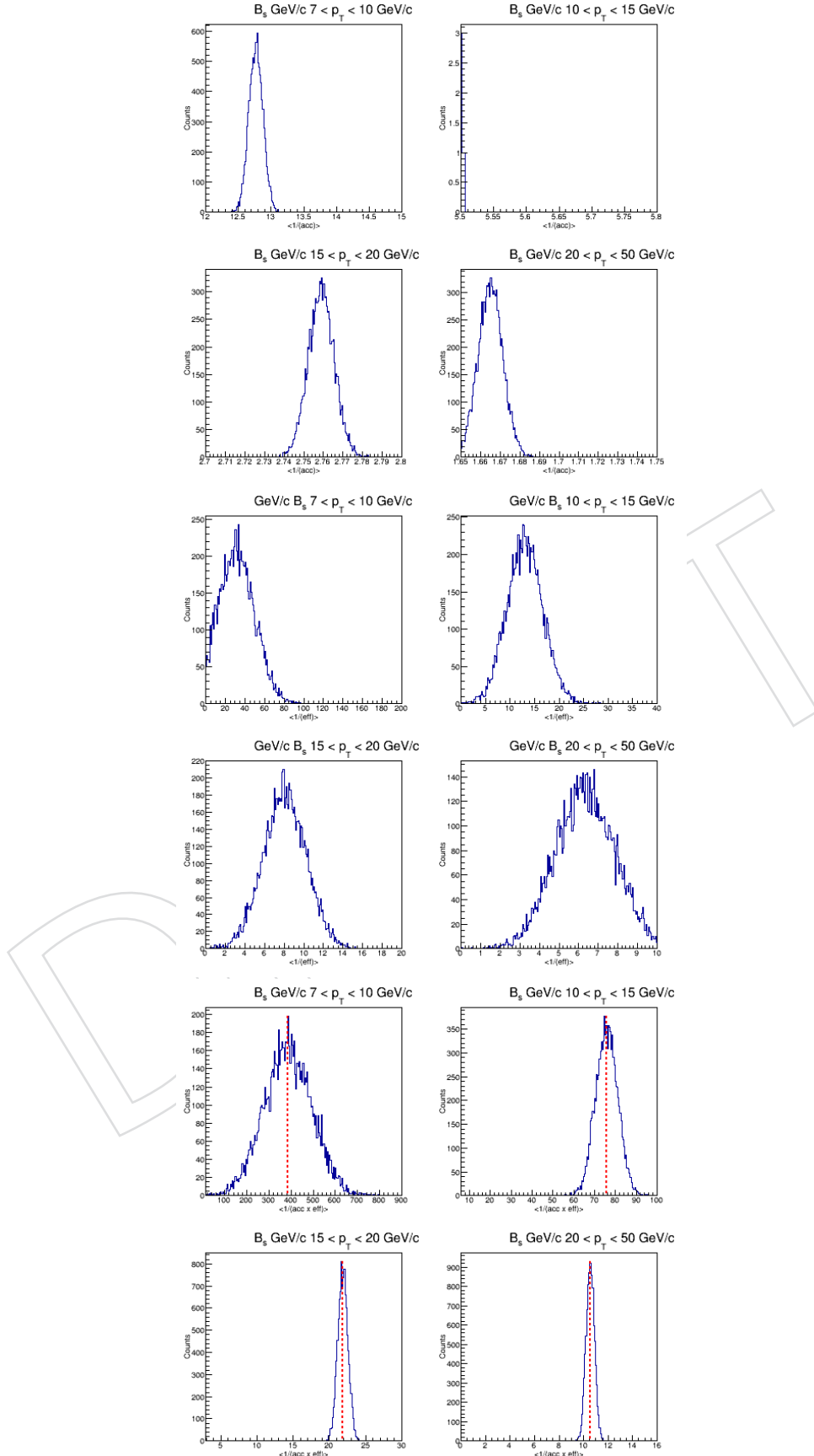


Figure 67: The distribution of $\langle \frac{1}{\alpha \times \epsilon} \rangle$ vs p_T at 0 - 90% are shown above. The red dash lines are our nominal value for efficiency correction.

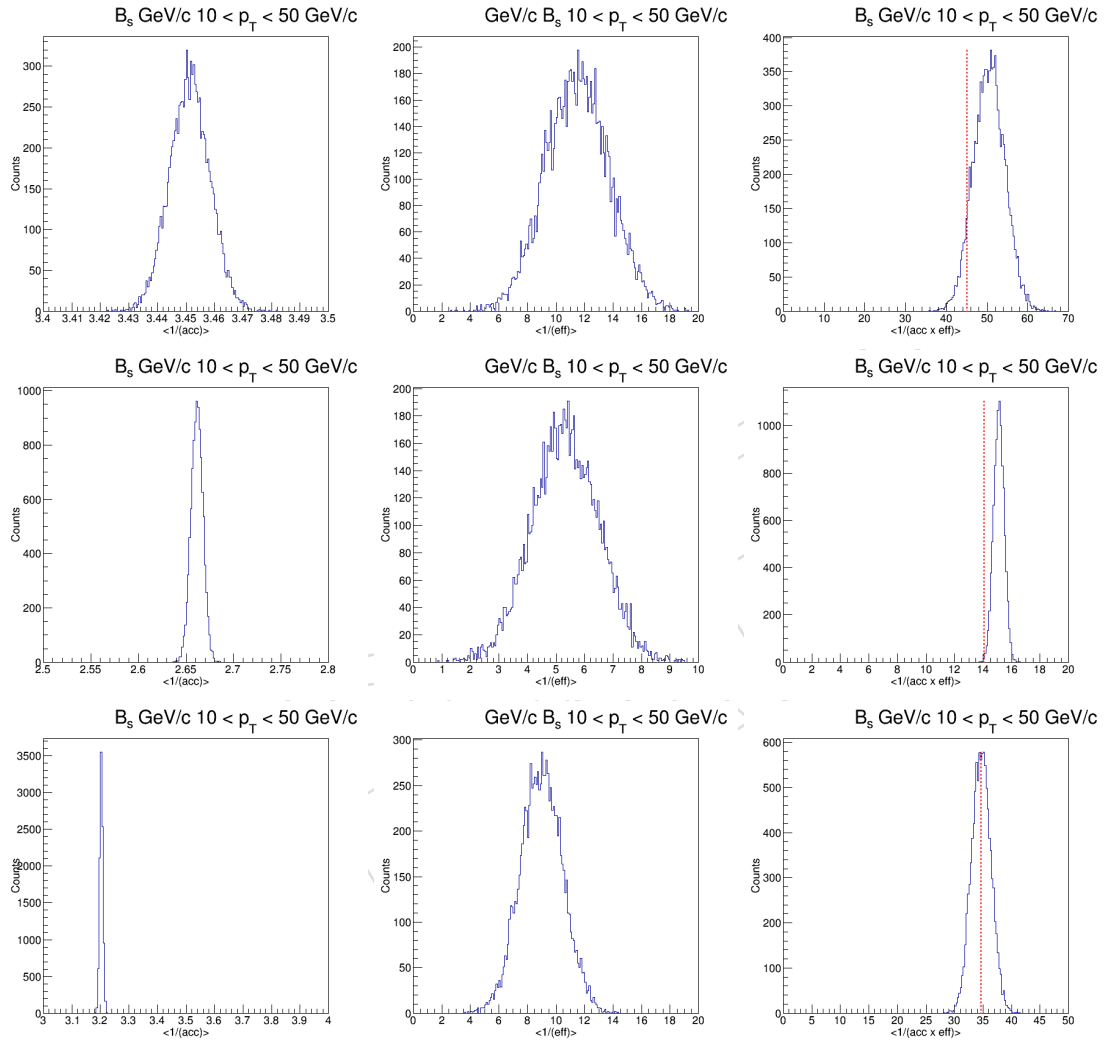


Figure 68: The distribution of $\langle \frac{1}{\alpha} \rangle$ (left), $\langle \frac{1}{\epsilon} \rangle$ (middle), $\langle \frac{1}{\alpha \times \epsilon} \rangle$ (right) for inclusive p_T at 0 - 30% (top), 30% - 90% (middle), 0 - 90% (bottom) are shown above. The red dash lines are our nominal value for efficiency correction.

863 The numerical results are summarize on Table 37 and Table 38

Table 37: Table of $\langle \frac{1}{\alpha \times \epsilon} \rangle$ for different p_T bins for unweighted, and weighted with BDT weighting factors, and their systematic uncertainties with centrality 0 - 90%

p_T Bin (GeV/c)	$\langle \frac{1}{\alpha} \rangle$ RMS/Mean	$\langle \frac{1}{\epsilon} \rangle$ RMS/Mean	$\langle \frac{1}{\alpha \times \epsilon} \rangle$ RMS/Mean
(7,10)	0.85%	52.2%	28.0%
(10,15)	0.04%	28.3%	7.04%
(15,20)	0.24%	27.1%	3.22%
(20,50)	0.37%	23.7%	3.23%

Table 38: Table of $\langle \frac{1}{\alpha \times \epsilon} \rangle$ for different p_T bins for unweighted, and weighted with BDT weighting factors, and their systematic uncertainties with centrality 0 - 90%

Centrality Bin	$\langle \frac{1}{\alpha} \rangle$ RMS/Mean	$\langle \frac{1}{\epsilon} \rangle$ RMS/Mean	$\langle \frac{1}{\alpha \times \epsilon} \rangle$ RMS/Mean
(0,30)	0.20%	19.4%	7.60%
(30,90)	0.24%	22.1%	2.44%
(0,90)	0.17%	16.4%	4.90%

864 10.6 Systematics associated with signal extraction

865 In this section, we check the effects of the choice of various PDFs on B_s^0 yield extraction. As
 866 discussed in Section 6, an exponential function is used as the default background PDF, and a
 867 double gaussian with a shape fixed from MC was chosen as the signal model. First, we vary
 868 the background PDF and then the signal PDF and we choose the maximum deviations from the
 869 nominal model. In the end, we sum both contributions in quadrature. The background PDF
 870 is changed to a linear function, 2nd and 3rd order polynomials. The B_s^0 raw yields from fits
 871 are compared with the yields from the nominal fit function. For the p_T bin from 7 to 10 GeV/c,
 872 0% is taken as the systematic arising from background variation, since there is practically no
 873 background in the sidebands of that bin. Fig. 69 and Fig. 70 show the invariant mass fit of B_s^0
 874 candidates with the nominal exponential function, linear, 2nd order and 3rd order polynomial
 875 as the background PDF respectively, for the lowest and highest B_s^0 p_T bins considered. The
 876 remaining invariant mass fits can be found in Appendix B.2. We calculate the systematic un-
 877 certainty associated with background PDF by considering the maximum yield difference (com-
 878 pared with default setting) among all different types of background PDF variation. Finally, the
 879 uncertainties associated to background PDF variation are available in Tab. 39, for different p_T
 880 bins, and in Tab 40 for different centrality bins.

Background Model (GeV/c)	$7 < p_T < 10$	$10 < p_T < 15$	$15 < p_T < 20$	$20 < p_T < 50$
Linear	0.02 %	1.45 %	1.45 %	3.30 %
2nd Poly	0.96 %	2.69 %	1.36 %	3.54 %
3rd Poly	0.96 %	2.64 %	0.28 %	6.11 %

Table 39: Summary table of signal extraction uncertainty on background PDF in 5.02 TeV PbPb collisions, for different p_T bins.

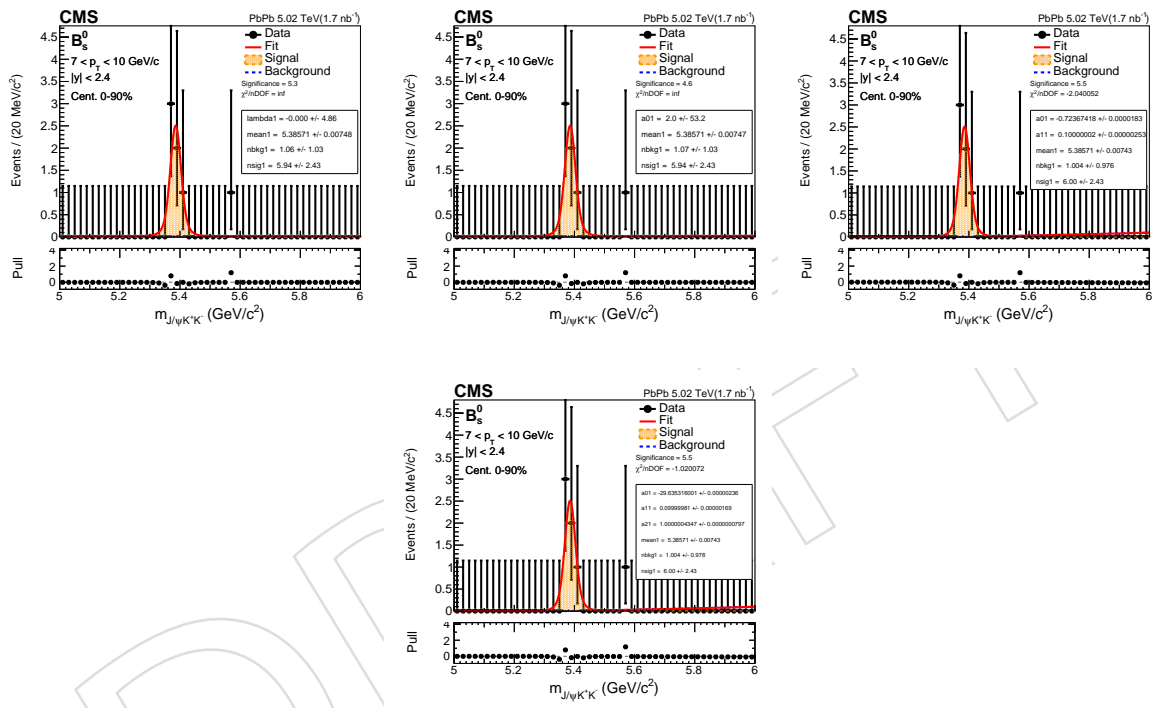


Figure 69: Invariant mass fit of B_s⁰ candidates for B_s⁰ p_T 7 < p_T < 10 GeV/c in 5.02 TeV PbPb. The background PDF from left to right is default exponential, linear, 2nd order polynomial and 3rd order polynomial.

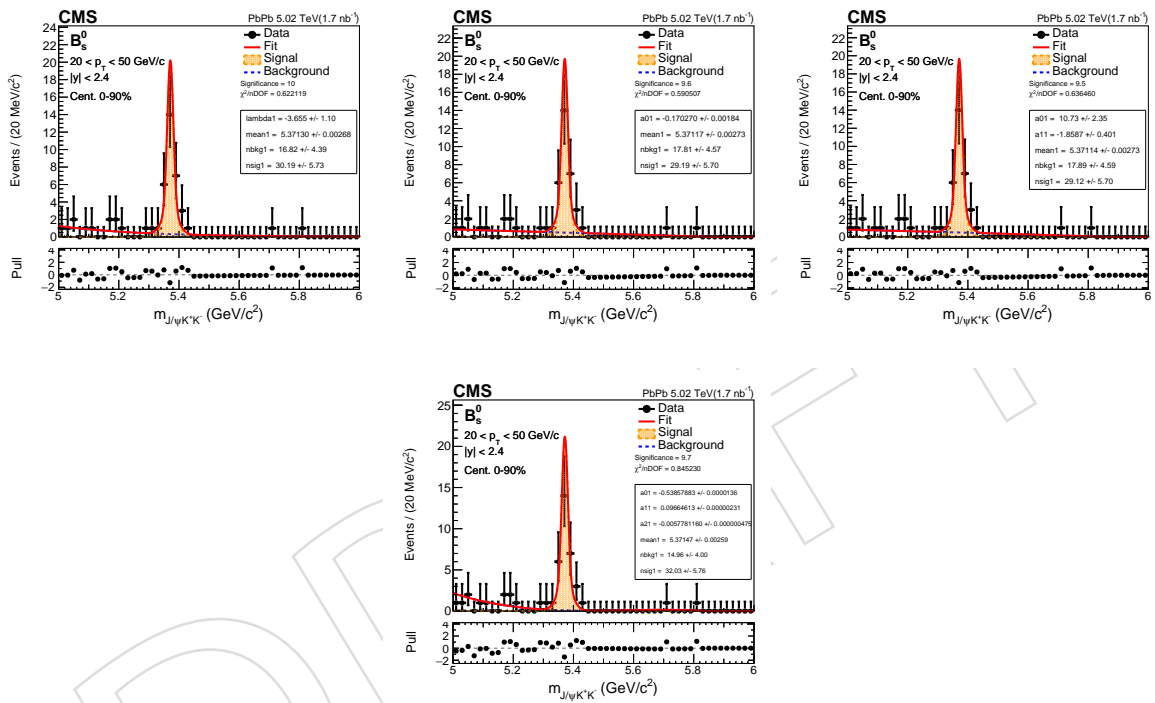


Figure 70: Invariant mass fit of B_s^0 candidates for $B_s^0 p_T 20 < p_T < 50 \text{ GeV}/c$ in 5.02 TeV PbPb. The background PDF from left to right is default exponential, linear, 2nd order polynomial and 3rd order polynomial.

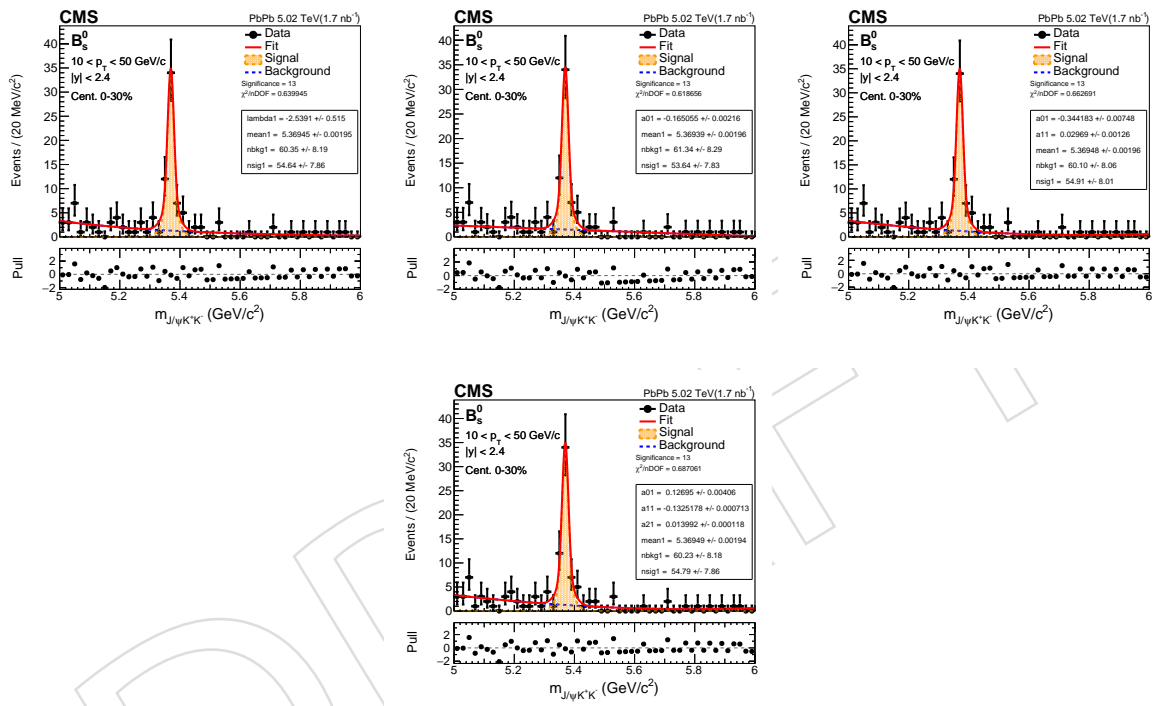


Figure 71: Invariant mass fit of B_s^0 candidates for B_s^0 in $0 < \text{Cent} < 30\%$ in 5.02 TeV PbPb. The background PDF from left to right is default exponential, linear, 2nd order polynomial and 3rd order polynomial.

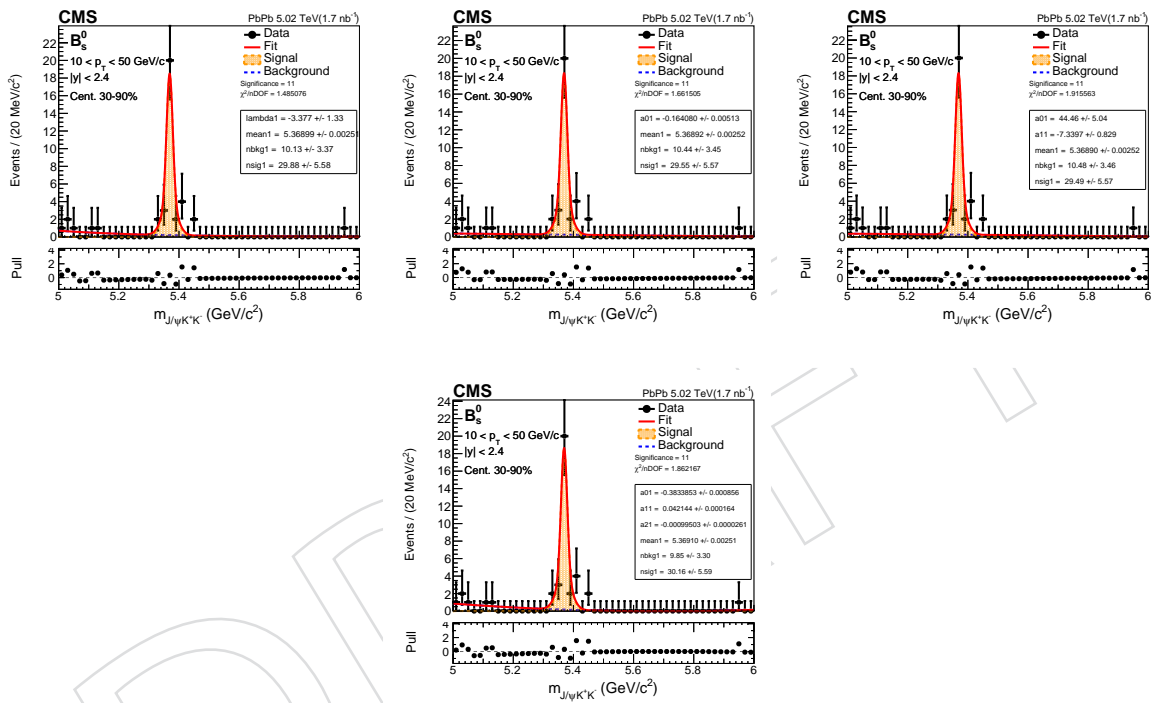


Figure 72: Invariant mass fit of B_s^0 candidates for B_s^0 in $30\% < \text{Cent} < 90\%$ in 5.02 TeV PbPb. The background PDF from left to right is default exponential, linear, 2nd order polynomial and 3rd order polynomial.

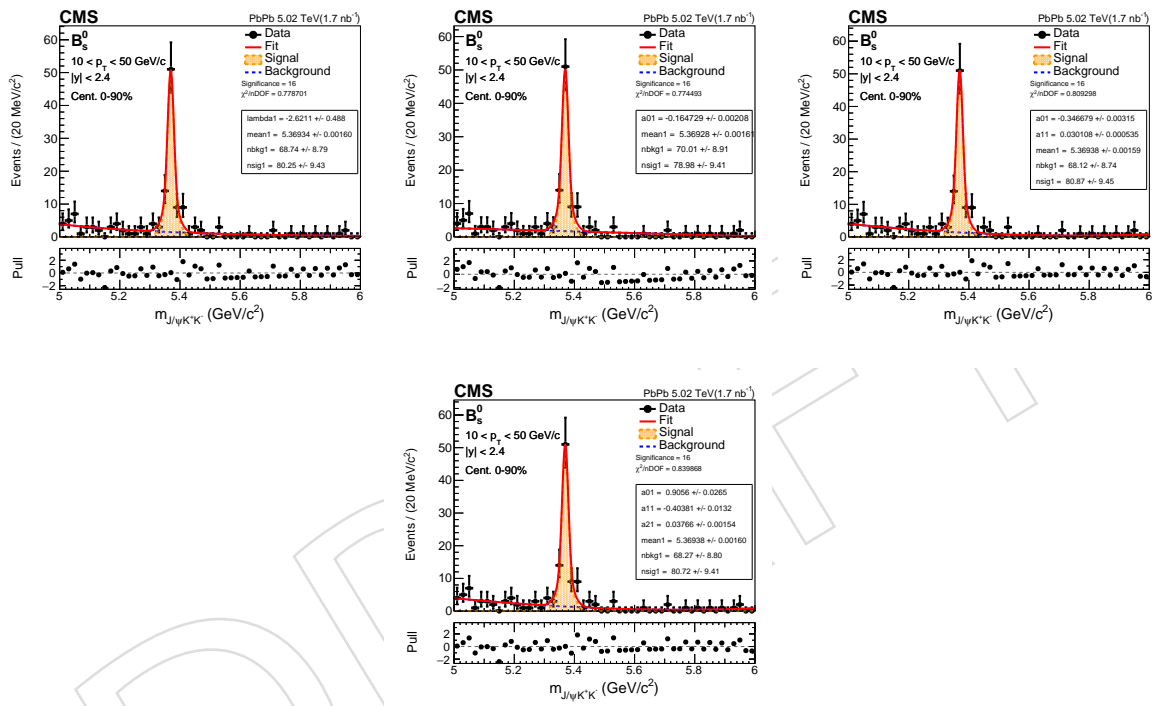


Figure 73: Invariant mass fit of B_s^0 candidates for B_s^0 in $0 < \text{Cent} < 90\%$ in 5.02 TeV PbPb. The background PDF from left to right is default exponential, linear, 2nd order polynomial and 3rd order polynomial.

Background Model	$0\% < Cent < 30\%$	$30\% < Cent < 90\%$	$0\% < Cent < 90\%$
Linear	1.83 %	1.14 %	1.58 %
2nd Poly	0.495 %	1.33 %	0.773 %
3rd Poly	0.029 %	0.912 %	0.592 %

Table 40: Summary table of signal extraction uncertainty on background PDF in 5.02 TeV PbPb collisions, for different centrality bins.

The systematic uncertainty arising from the variation of the signal PDF was calculated by changing the model from the nominal double Gaussian to a triple Gaussian. Furthermore, recall that in the signal extraction process the signal shape (except the gaussians' mean) is fixed from MC. Trying to cover a possible discrepancy between the MC and data gaussian resolution, a fit was done to the data with an extra free parameter - a scaling factor between the gaussians' width in data and MC. The signal model used in the fit to data is, in that study:

$$\alpha \frac{1}{a\sigma_1 \sqrt{2\pi}} e^{-\frac{1}{2} \frac{(B_{mass}-\mu)^2}{(a\sigma_1)^2}} + (1-\alpha) \frac{1}{a\sigma_2 \sqrt{2\pi}} e^{-\frac{1}{2} \frac{(B_{mass}-\mu)^2}{(a\sigma_2)^2}}, \quad (12)$$

where a is the resolution scaling factor (the same for both gaussians), α is the relative proportion between the gaussians, σ_1 and σ_2 are the gaussians' widths and μ is the mean shared by both gaussians. Since this study implies adding an extra free parameter, and there is more statistics for B^+ we used that channel to perform the study [11]. There, a variation of 10% from the nominal value of $a = 1$ was concluded to cover the discrepancies seen between the gaussians' resolution in data and MC. The fit with this signal model is also performed to the most inclusive bin for the B_s^0 , and can be seen in Figure 74, where that value is compatible with 1. In the end, 2 variations were done from the nominal signal model. An increased width with the parameter a set to 1.1 and a decreased width with the parameter a fixed to 0.9.

In addition to that, while in the default setting the mean value of the double Gaussian is a floating parameter, we also checked the effect of fixing the mean to the value obtained by fitting on signal MC .

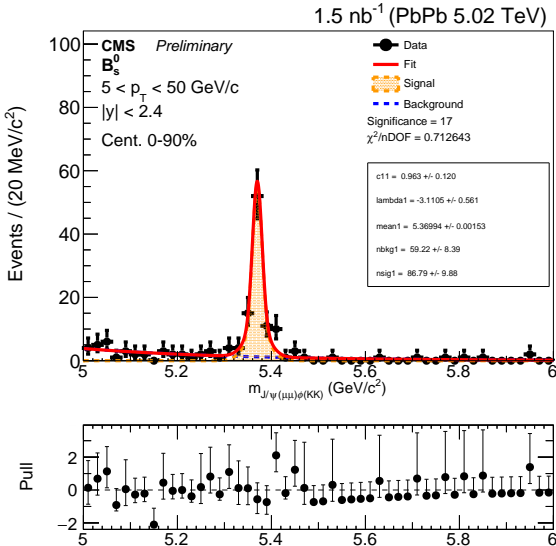


Figure 74: Invariant mass fit of B_s^0 candidates for p_T $5 < p_T < 50$ GeV/c in 5.02 TeV, with an extra free parameter in the signal model a , as described by Eq. 12

Fig. 75 and Fig 76 show examples of fits results, for the lowest and highest B_s^0 p_T bins. The remaining fits are included in Appendix B.2 Again we quote the systematic uncertainty associated with signal PDF by calculating the maximum yield difference (compared with default setting) among all the different variations. Detailed uncertainties due to signal PDF variation are available in Tab. 41, for different p_T bins, and in Tab. 42, for different centrality bins.

Finally, we also summarize the likelihood difference for different fits in the inclusive 10 - 50 GeV/c in 0 - 90% centrality in the table below 43.

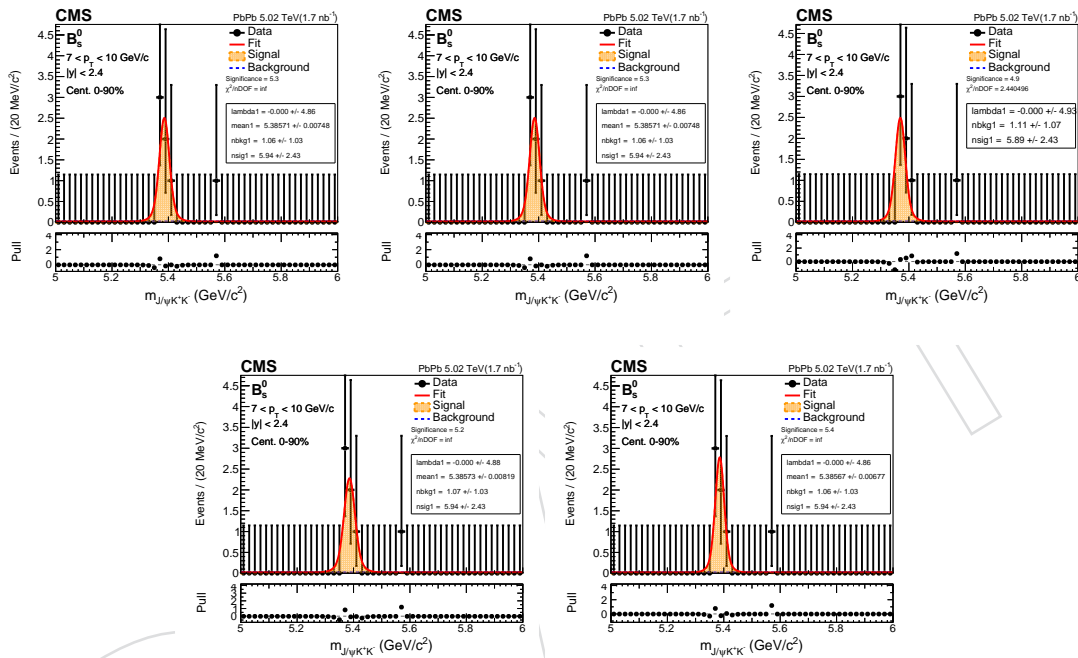


Figure 75: Invariant mass fit of B_s^0 candidates for $B_s^0 p_T$ from 7 to 10 GeV/c in 5.02 TeV PbPb. The signal pdf from left to right is default double gaussian (with widths and relative proportion fixed from MC), triple gaussian (with widths and relative proportions fixed from MC), double gaussian with all the parameters fixed (including the mean), increased width ($a=1.1$), and decreased width ($a=0.9$).

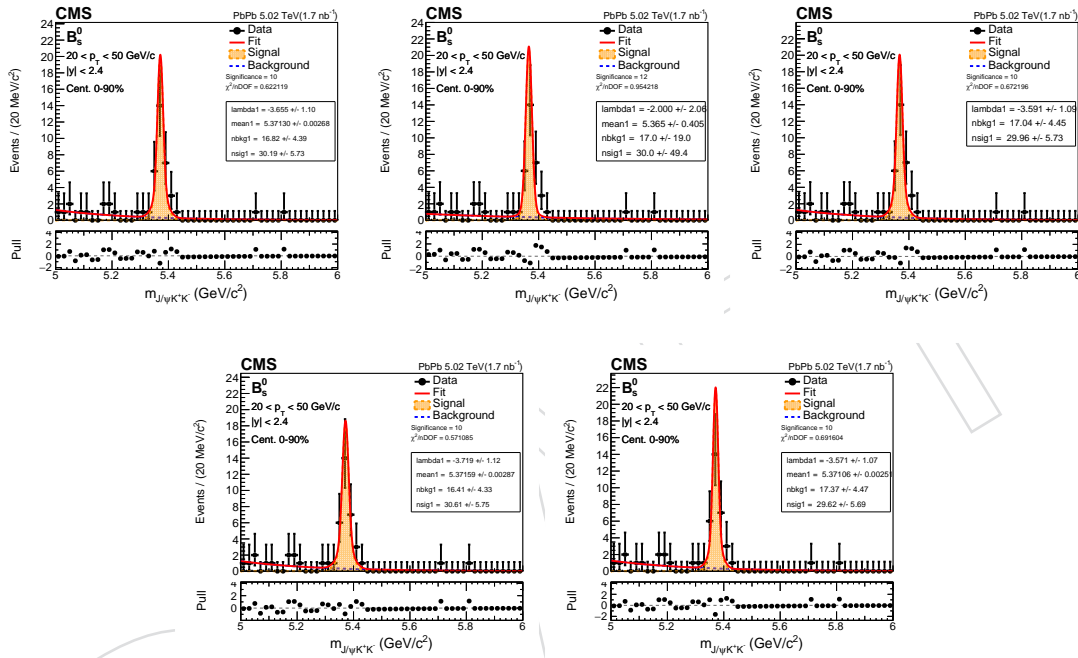


Figure 76: Invariant mass fit of B_s^0 candidates for $B_s^0 p_T$ from 20 to 50 GeV/c in 5.02 TeV PbPb. The signal pdf from left to right is default double gaussian (with widths and relative proportion fixed from MC), triple gaussian (with widths and relative proportions fixed from MC), double gaussian with all the parameters fixed (including the mean), increased width ($a=1.1$), and decreased width ($a=0.9$).

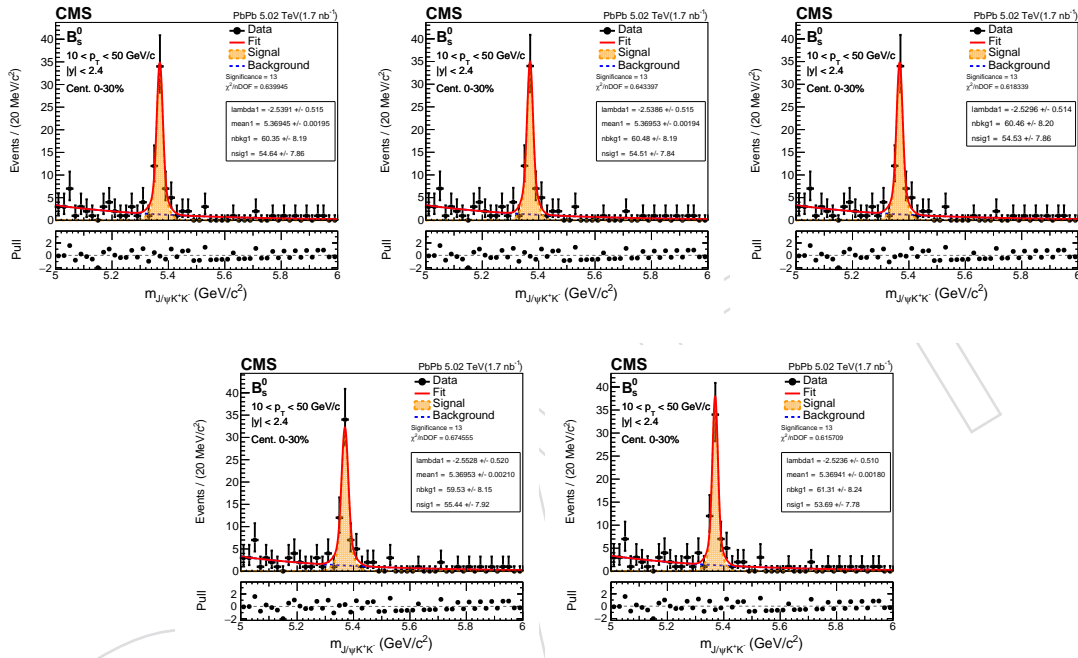


Figure 77: Invariant mass fit of B_s^0 candidates for B_s^0 centrality from 0 to 30% in 5.02 TeV PbPb. The signal pdf from left to right is default double gaussian (with widths and relative proportion fixed from MC), triple gaussian (with widths and relative proportions fixed from MC), double gaussian with all the parameters fixed (including the mean), increased width ($a=1.1$), and decreased width ($a=0.9$).

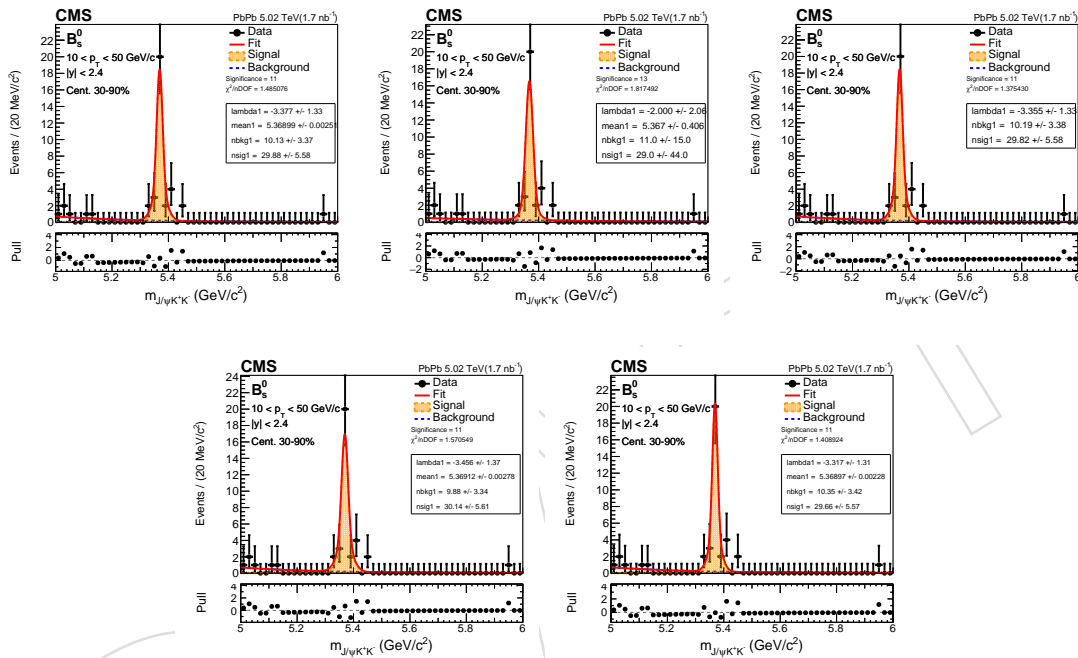


Figure 78: Invariant mass fit of B_s^0 candidates for B_s^0 centrality from 30% to 90% in 5.02 TeV PbPb. The signal pdf from left to right is default double gaussian (with widths and relative proportions fixed from MC), triple gaussian (with widths and relative proportions fixed from MC), double gaussian with all the parameters fixed (including the mean), increased width ($a=1.1$), and decreased width ($a=0.9$).

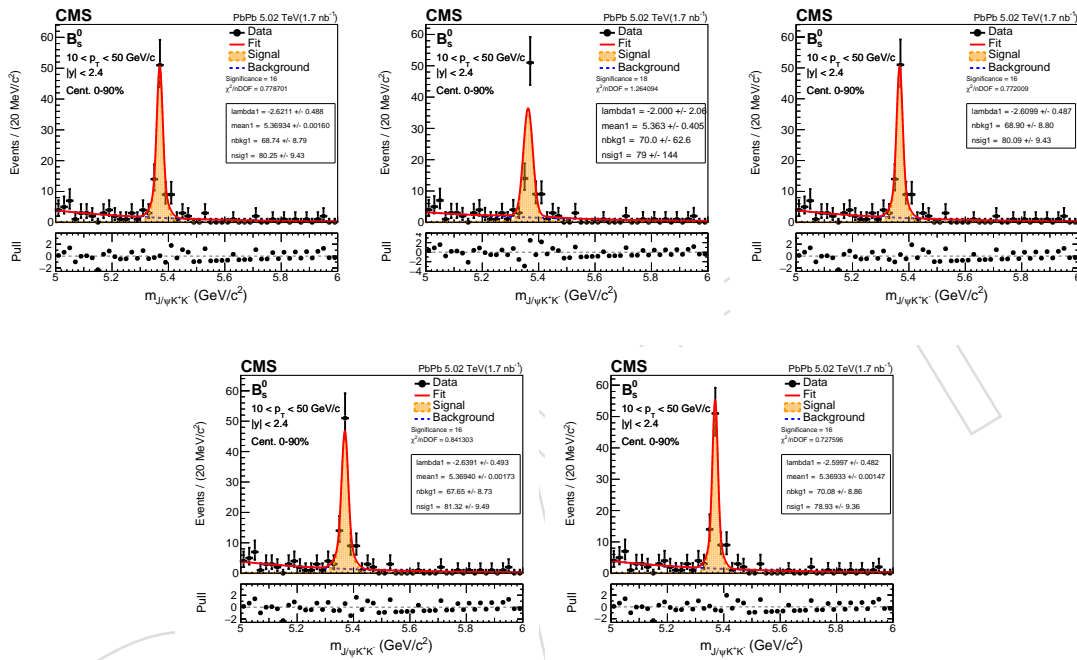


Figure 79: Invariant mass fit of B_s^0 candidates for B_s^0 centrality from 0 to 90% in 5.02 TeV PbPb. The signal pdf from left to right is default double gaussian (with widths and relative proportion fixed from MC), triple gaussian (with widths and relative proportions fixed from MC), double gaussian with all the parameters fixed (including the mean), increased width ($a=1.1$), and decreased width ($a=0.9$).

Signal Model (GeV/c)	$7 < p_T < 10$	$10 < p_T < 15$	$15 < p_T < 20$	$20 < p_T < 50$
Triple Gaussian	0.862 %	0.144 %	0.110 %	0.629 %
Fixed Mean	0.762 %	0.137 %	0.188 %	0.753 %
Increased σ scaling factor	0.066 %	1.83 %	1.02 %	1.40 %
Decreased σ scaling factor	0.056 %	2.34 %	1.00 %	1.88 %

Table 41: Summary table of signal extraction uncertainty on signal width in 5.02 TeV PbPb collisions, in different p_T bins.

Signal Model	$0\% < Cent < 30\%$	$30\% < Cent < 90\%$	$0\% < Cent < 90\%$
Triple Gaussian	0.241 %	2.96 %	1.56 %
Fixed Mean	0.192 %	0.208 %	0.20 %
Increased σ scaling factor	1.47 %	0.840 %	1.33 %
Decreased σ scaling factor	1.74 %	0.767 %	1.65 %

Table 42: Summary table of signal extraction uncertainty on signal width in 5.02 TeV PbPb collisions, in different centrality bins.

900 The final systematic uncertainty associated with pdf variation is calculated by the quadratic
 901 sum of the signal and background variation. The values are documented in Tables 44 and 45.

Variation	Variation Function	Likelihood Difference
Nominal	Double Gaussian	16.394
Signal	Triple Gaussian	17.935
Signal	Fixed Mean	16.339
Signal	Width + 10%	16.3304
Signal	Width - 10%	16.4289
Background	Linear	15.7384
Background	Quadratic	16.0074
Background	3rd Polynomial	16.0065

Table 43: Summary table of the square root of likelihood difference in the inclusive 10 - 50 GeV/c in 0 - 90% centrality. The smallest value is about 16.2 (variation with linear background). it is quoted as the significance in the paper draft.

Systematic Source (GeV/c)	$7 < p_T < 10$	$10 < p_T < 15$	$15 < p_T < 20$	$20 < p_T < 50$
Background	0.96 %	2.69 %	1.45 %	6.11 %
Signal	0.762 %	2.34 %	1.02 %	1.88 %
Total	1.23 %	3.57 %	1.77 %	6.39 %

Table 44: Summary table of signal extraction uncertainty, for different p_T bins.

Systematic Source	$0\% < Cent < 30\%$	$30\% < Cent < 90\%$	$0\% < Cent < 90\%$
Background	1.83 %	1.33 %	1.58 %
Signal	1.74 %	2.96 %	1.65 %
Total	2.53 %	3.25 %	2.28 %

Table 45: Summary table of signal extraction uncertainty, for different centrality bins.

902 10.7 Systematics on p_T shape

903 Even we finely bin the $\frac{1}{\alpha \times \epsilon}$ vs B p_T and B $|y|$, there can still be residue B p_T shape effect in the
 904 efficiency correction. Therefore, we check the final corrected yield as well as their closure. The
 905 B p_T shape function are quoted from the B p_T reweighting in 2. We have no weight (nominal),
 906 Linear, Quadratic, Linear + Inverse, Linear + Square Root, and Linear + Log. Table 46 and
 907 Table 47 show the corrected yields of different B p_T shape reweighting functions vs p_T and
 908 centrality respectfully

Table 46: Table of corrected yield for different p_T bins with different B p_T shape functions with
 centrality 0 - 90%

Corrected yield	No Weight	Linear	Quadratic	Linear + Inv	Linear + Sqrt	Linear + Log
(7,10)	1070540	1070800	1070370	1068740	1070040	1069870
(10,15)	684452	684457	684441	684361	684423	684415
(15,20)	199071	199054	199068	199070	199068	199067
(20,50)	121564	121548	121537	121532	121538	121538
(7,50)	2143750	2143980	2143530	2141760	2143170	2142990

Table 47: Table of corrected yield for different p_T bins with different B p_T shape functions with
 centrality 0 - 90% at 10 - 50 GeV/c

Corrected yield	No Weight	Linear	Quadratic	Linear + Inv	Linear + Sqrt	Linear + Log
(0,30%)	952729	952755	952677	952457	952628	952608
(30%, 90%)	156335	156331	156325	156318	156325	156324
(0, 90%)	1117760	1117740	1117720	1117630	1117700	1117690

909 The systematic on MC p_T shape was evaluated by comparing the corrected yield ratio of the
 910 nominal, which has no B p_T weight, to a variety of fitting functions to the data/MC p_T ratio
 911 shape. We quote the maximum deviation as the systematics uncertainties. Our final results for
 912 B p_T shape systematic uncertainties are summarized on Table 48 and Table 49 below

Table 48: Summary of deviation from unity for the corrected yield ratio for different referenced
 fitting functions compared to the nominal fitting function (No weight) vs p_T bins are shown
 as above. The bold values are the maximal deviation from unity and will be quoted as the p_T
 shape systematics for p_T bins.

Fitting Functions	(7, 10)	(10, 15)	(15, 20)	(20, 50)
Linear	0.024%	0.001%	0.008%	0.011%
Quadratic	0.016%	0.002%	0.002%	0.010%
Linear + Inverse	0.17%	0.013%	0.001%	0.093%
Linear + Square Root	0.047%	0.004%	0.003%	0.027%
Linear + Logarithm	0.063%	0.005%	0.002%	0.068%

913 We can see that, using this data-driven strategies, we still have the largest systematics for the
 914 lowest p_T bin at 5 - 10 GeV/c. For the centrality over an inclusive p_T bin 5 - 50 GeV/c, we can
 915 see that its uncertainty is in between the maximum and minimum deviation among the p_T bins.

Table 49: Summary of deviation from unity for the corrected yield ratio for different referenced fitting functions compared to the nominal fitting function (No weight) vs p_T bins are shown as above. The bold values are the maximal deviation from unity and will be quoted as the p_T shape systematics for centrality bins.

Fitting Functions	[0, 30]	[30, 90]	[0, 90]
Linear	0.003%	0.003%	0.002%
Quadratic	0.005%	0.006%	0.004%
Linear + Inverse	0.029%	0.011%	0.012%
Linear + Square Root	0.011%	0.006%	0.005%
Linear + Logarithm	0.013%	0.007%	0.006%

916 Here, we quote the maximal deviation from unity among the fitting function for each p_T and
 917 centrality bin as the p_T shape systematics. We can see that the p_T shape systematic uncertainties
 918 is well below 1%. This shows the triumph of the event-by-event efficiency reweighting method
 919 for efficiency correction $\langle \frac{1}{\alpha e} \rangle$. It indeed almost eliminated the p_T shape systematic uncertainties.

920 10.8 Summary table

921 Below is the summary table of various systematic uncertainties.

Table 50: Summary of systematic uncertainties from each factor in PbPb analysis for corrected yield vs p_T . All the value is shown in percentage.

Factors	(7,10)	(10,15)	(15,20)	(20,50)
Hadron tracking efficiency	10%	10%	10%	10%
Data-MC Discrepancy	34.72%	4.74%	4.96%	10.36%
p_T shape	0.17%	0.013%	0.008%	0.093%
PDF variation background	0.96%	2.69%	1.45%	6.11%
PDF variation signal	0.762%	2.34%	1.02%	1.88%
TnP Systematics +)	20.0%	9.34%	6.01%	6.05%
TnP Systematics -)	14.2%	8.08%	5.68%	5.73%
MC stat.	28.0%	7.04 %	3.22%	3.23 %
Total +)	51.08%	16.22 %	13.20%	16.34%
Total -)	49.10%	15.53 %	13.05%	16.22%
N_{MB+}) events	1.18%	1.18%	1.18%	1.18%
N_{MB-}) events	1.18%	1.18%	1.18%	1.18%
T_{AA}	2.2%	2.2%	2.2%	2.2%
Branching fractions	7.6%	7.6%	7.6%	7.6%
Global Systematics +)	8.00%	8.00%	8.00%	8.00%
Global Systematics -)	8.00%	8.00%	8.00%	8.00%

922 Finally, we plot the summary plots for the table above as follows in Fig 80

Table 51: Summary of systematic uncertainties from each factor in PbPb analysis for corrected yield vs centrality. All the value is shown in percentage.

Factors	0 - 30 %	30 % - 90%	0 - 90 %
Hadron tracking efficiency	10%	10%	10%
Data-MC Discrepancy	2.26%	3.04 %	1.81%
p_T shape	0.029%	0.011%	0.012%
PDF variation background	1.83%	1.33%	1.58%
PDF variation signal	1.74%	2.96%	1.65%
TnP Systematics +)	9.13%	7.23%	8.36%
TnP Systematics -)	7.77%	6.64%	7.37%
MC stat.	7.60%	2.44%	4.90%
T_{AA}	2%	3.6%	2.2%
N_{MB} events +)	1.32%	1.22%	1.18%
N_{MB} events -)	1.34%	1.21%	1.18%
Total +)	16.7%	13.5%	14.3%
Total -)	15.9%	13.2%	13.7%
Branching fractions	7.6%	7.6%	7.6%
Global Systematics +)	7.6%	7.6%	7.6%
Global Systematics -)	7.6%	7.6%	7.6%

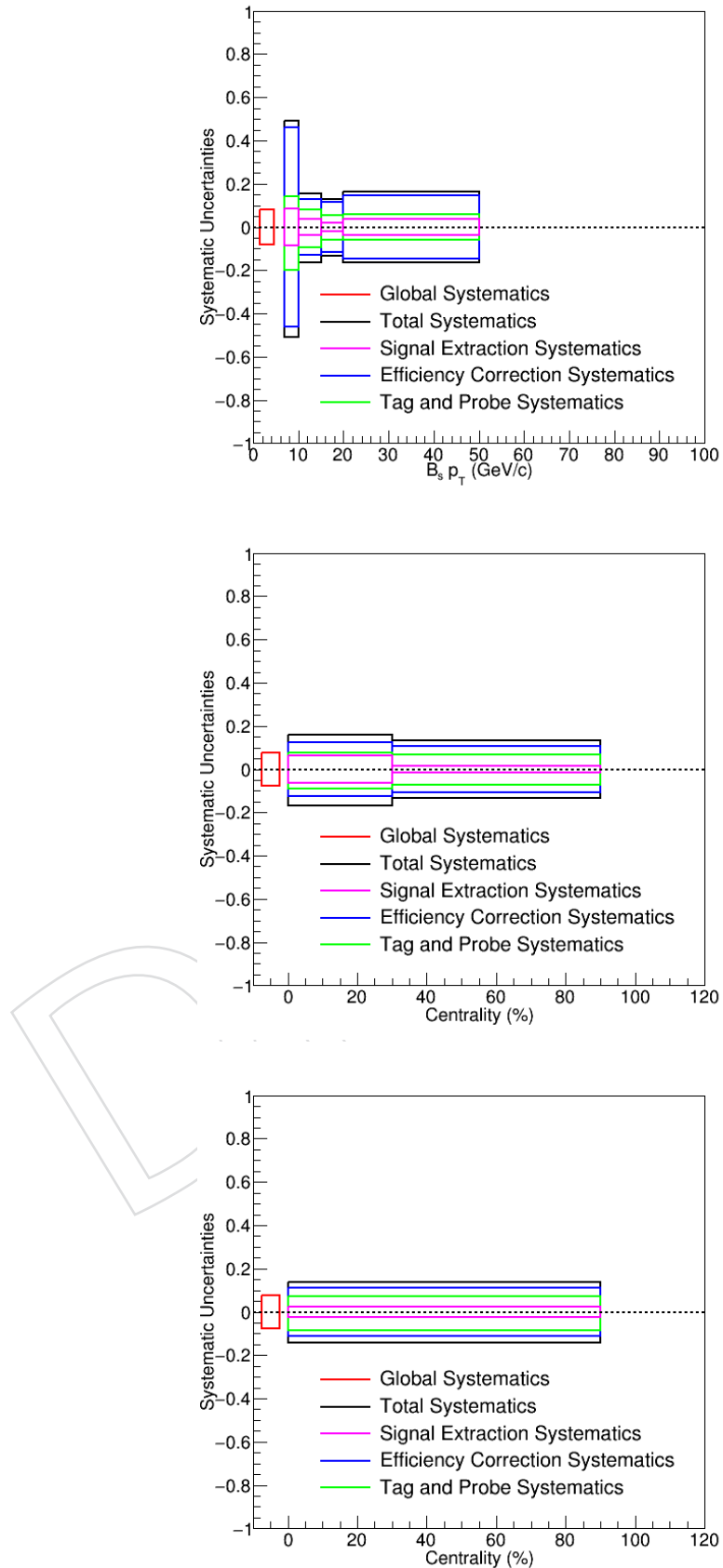


Figure 80: The plots summarizing the systematic uncertainties for p_T bins and centrality bins are shown above.

923 10.9 Additional studies: Invariant mass of BDT variables

924 As show in Section 4, we use the side band sufficiently far away from B_s^0 PDG mass value
 925 as the input for background in TMVA training. Due to the nature of the inputs of our BDT
 926 training, it is possible that the BDT has dependence on the invariant mass. To investigate the
 927 BDT dependence on the invariant mass. We perform the BDT shape comparison in differ-
 928 ent invariant mass side band range. Here we choose the mass side band to be $MassDown <$
 929 $|Bmass - B_s^0 PDG Mass| < MassDown + 0.04$. Here, Mass down is 0.20 - 0.24 - 0.28 - 0.32 - 0.36
 930 - 0.40 GeV/c^2 . Figure 81 below summarizes the color scheme for the plots in the section.

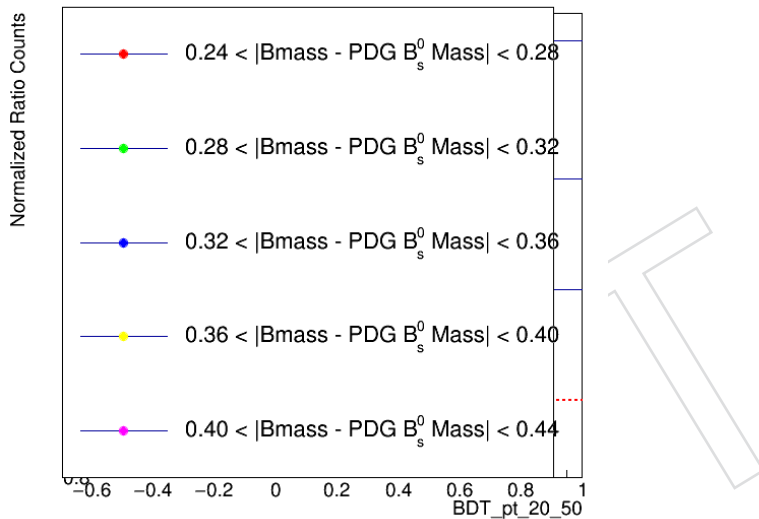


Figure 81: The legend for the color for BDT shapes in different B_s^0 mass side band in data is shown above. They apply to all the following plots below.

931 First, we compare the BDT shape for in different mass region for the BDT variables. Figure 82
 932 shows the comparison for four different p_T bins

933 We can see that the BDT at different invariant mass ranges have very similar shapes. To quan-
 934 tify the effect, we take the ratio of the colored point with respect to the reference shape black
 935 point $0.20 < |Bmass - B_s^0 PDG Mass| < 0.24 \text{ GeV}/c^2$ and compare them to unity. The results
 936 are show as follows in Figure 83

937 To estimate the effect on the efficiency correction, we then perform a linear fit on the pink
 938 ratio points ($0.40 < |Bmass - B_s^0 PDG Mass| < 0.44 \text{ GeV}/c^2$), which appear to have maximal
 939 deviation from unity. The fitting results are shown below in Figure 84

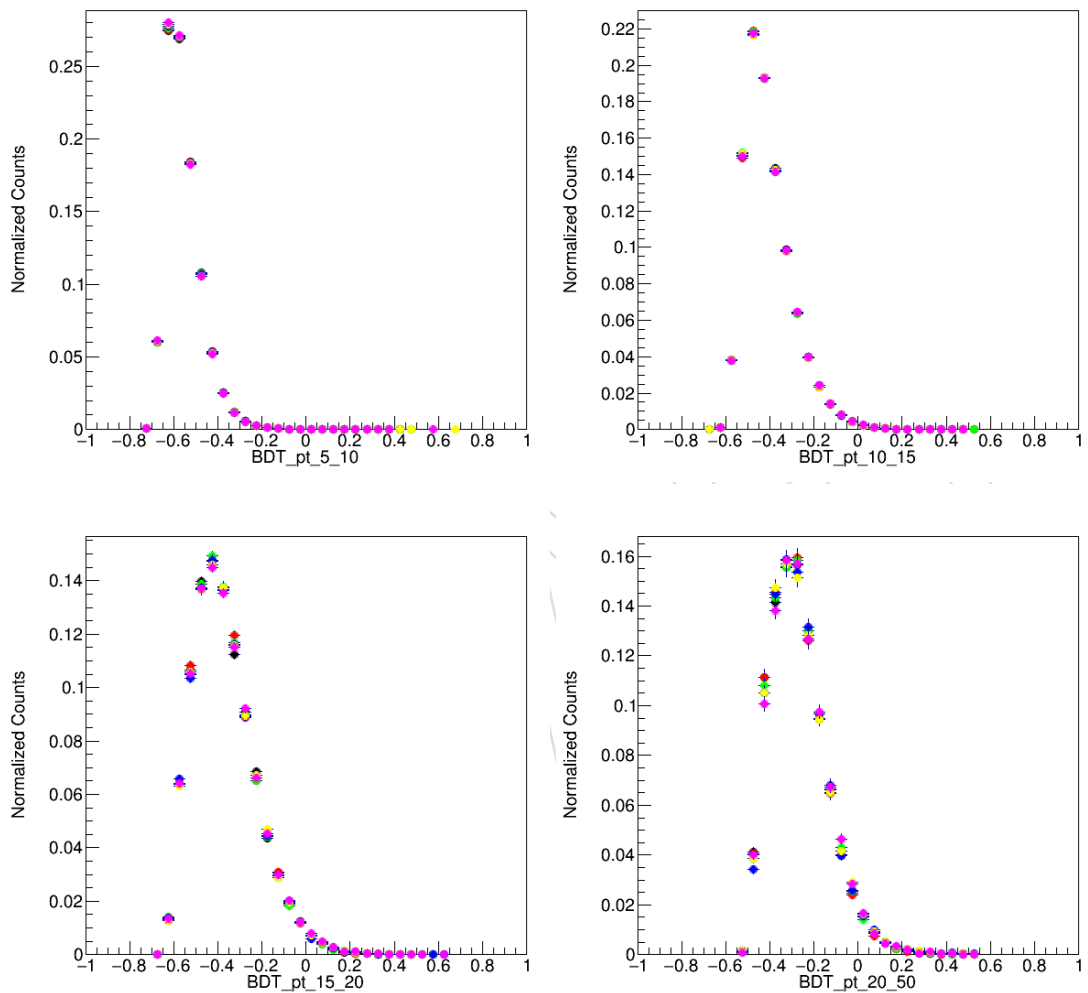


Figure 82: The BDT in p_T ranges from 5 - 10 (upper left), 10 - 15 (upper right), 15 - 20 (lower left), and 20 - 50 (lower right) GeV/c at different side band invariant mass region of B_s^0 data are shown above.

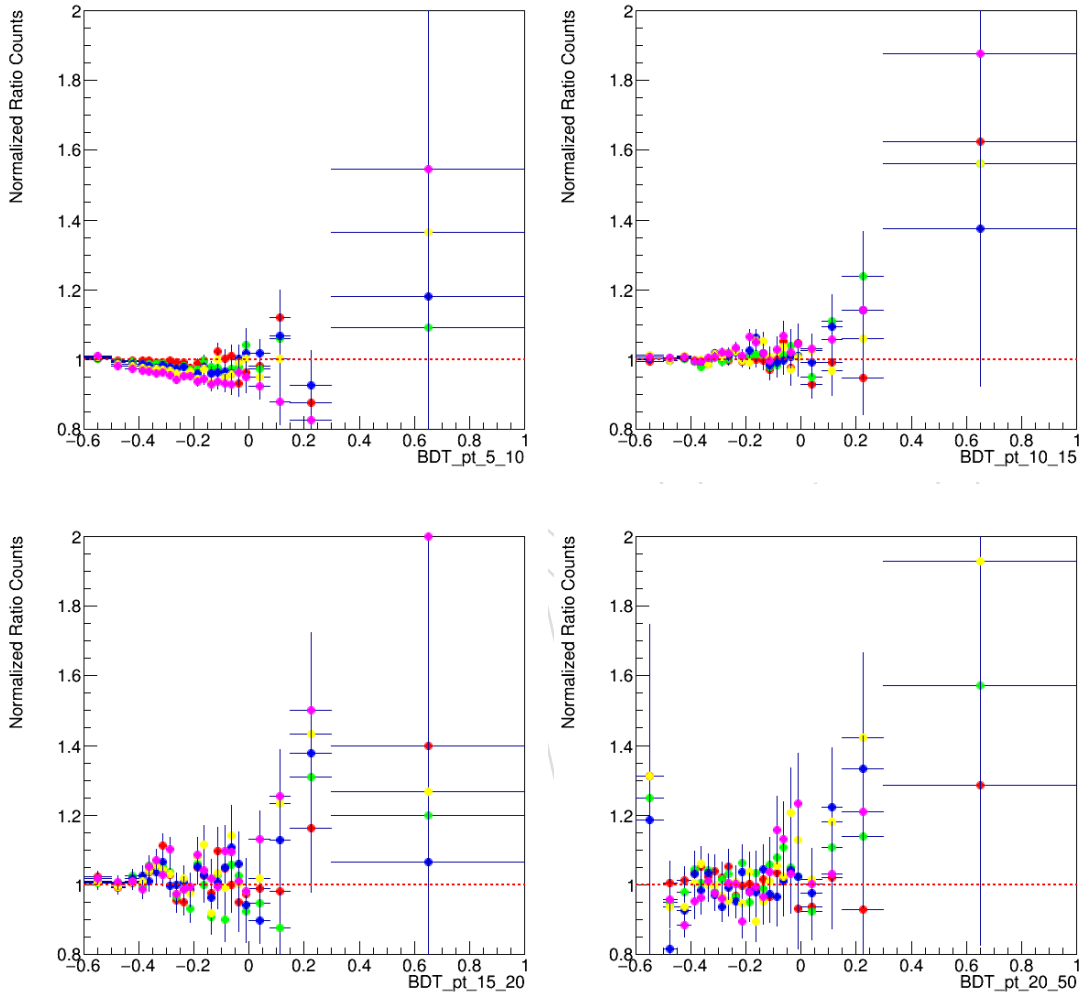


Figure 83: The BDT shape ratios with respect to $0.20 < |B_{mass} - B_s^0 PDGMass| < 0.24 \text{ GeV}/c^2$ in p_T ranges from 5 - 10 (upper left), 10 - 15 (upper right), 15 - 20 (lower left), and 20 - 50 (lower right) GeV/c at different side band invariant mass region of B_s^0 data are shown above. The red lines indicate unity.

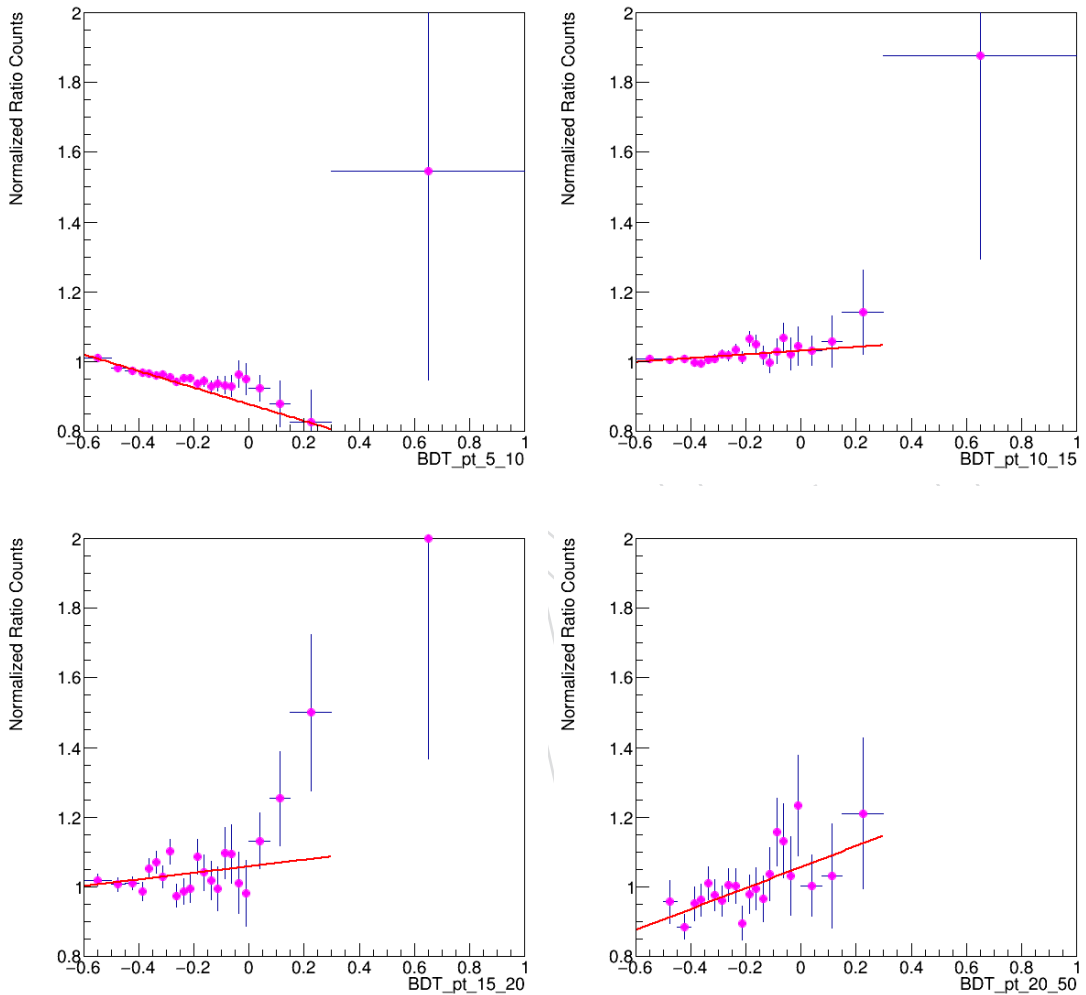


Figure 84: The fits on BDT shape ratio of $0.20 < |B_{mass} - B_s^0 PDGMass| < 0.24 \text{ GeV}/c^2$ with respect to $0.20 < |B_{mass} - B_s^0 PDGMass| < 0.24 \text{ GeV}/c^2$ in p_T ranges from 5 - 10 (upper left), 10 - 15 (upper right), 15 - 20 (lower left), and 20 - 50 (lower right) GeV/c at different side band invariant mass region of B_s^0 data are shown above.

⁹⁴⁰ The fitting parameter are summarized on the Table 52

Table 52: The y-intercept and slope of the linear fits (weight = [0] + [1] * BDT) to the BDT shape ratio of $0.20 < |B_{mass} - B_s^0 PDG Mass| < 0.24 \text{ GeV}/c^2$ with respect to $0.20 < |B_{mass} - B_s^0 PDG Mass| < 0.24 \text{ GeV}/c^2$ in different p_T bins are shown below.

p_T Bin (GeV/c)	y-intercept ([0])	slope ([1])
5 - 10	0.877	0.237
10 - 15	1.031	0.0534
15 - 20	1.058	0.0942
20 - 50	1.055	0.301

⁹⁴¹ We apply the linear function of the BDT value (weight = [0] + [1] * BDT) as a weight on the invariant distribution within the p_T range. Outside the p_T range, the weight is set to 1. Therefore, when apply correction to inclusive p_T bins, for instance, for p_T from 10 to 50 GeV/c , each BDT variable applies accordingly to its p_T range.

⁹⁴⁵ We perform the raw yield fits on the weighted and unweighted invariant mass distributions and look at the effect on the signal raw yields. Then, for the weighted raw yield, due to the BDT, our scale is above or below 1. We thus rescale the weighted signal raw yield by the factor ⁹⁴⁷ F: $F = \text{unweighted candidates}/\text{weighted candidates}$. The weighted raw yield fit as for different ⁹⁴⁸ p_T and centrality bins are shown on Fig 86 and Fig ?? respectfully

DRAFT

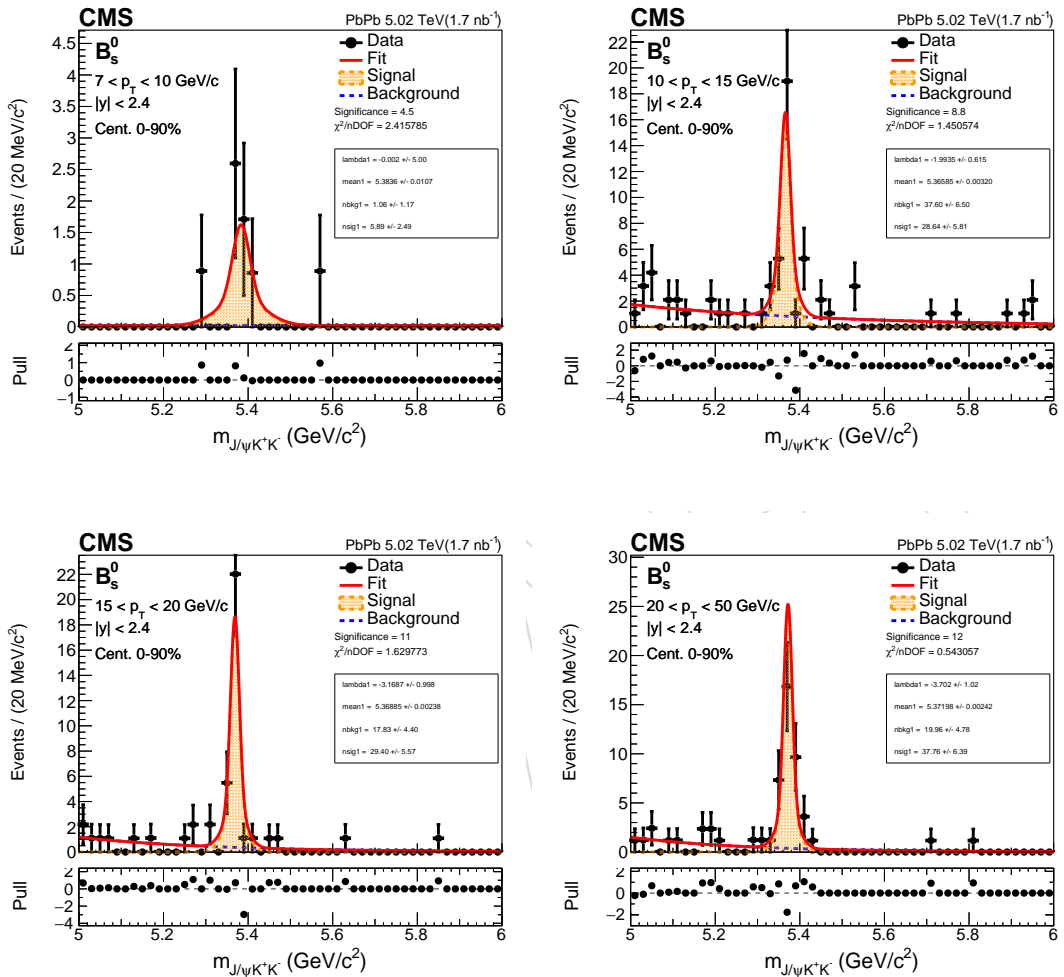


Figure 85: The unbinned fits on the BDT ratio weighted invariant mass distribution for raw yield extraction for p_T in the range of 7 - 10 GeV/c, 10 - 15 GeV/c, 15 - 20 GeV/c, and 20 - 50 GeV/c in centrality range of 0 - 90% are shown above.

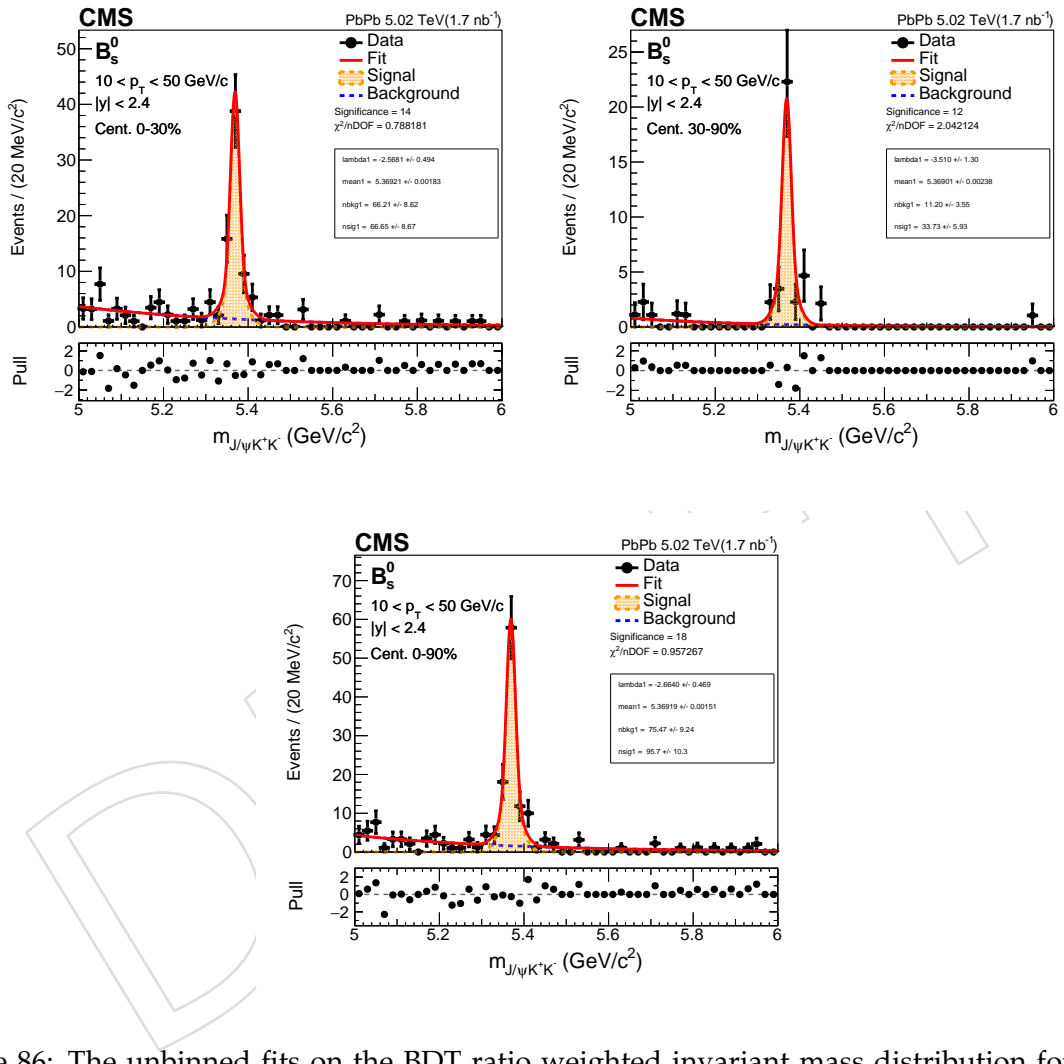


Figure 86: The unbinned fits on the BDT ratio weighted invariant mass distribution for raw yield extraction for centrality in the range of 0 - 30%, 30 - 90%, and 0 - 90% in the p_T range of 10 - 50 GeV/c are shown above.

950 We can see all the fits are good. Next we rescale the number of candidate from the weighted to
 951 unweighted raw yield fits by counting the total candidates. Finally, Table 53 shows the nominal
 952 and linearly weighted rescaled signal raw yield and the percentage deviation of the variated
 953 signal raw yield from nominal raw yield for each p_T and centrality.

Table 53: The summary table of BDT vs mass dependence systematics on the background yield from the fits in different p_T and centrality bins are shown below.

Centrality	p_T (GeV/c)	Nom. Signal Yield	Rescaled Weighted Signal Yield	Percent Deviation
0 - 90%	7 - 10	6.831	6.787	0.64%
0 - 90%	10 - 15	27.14	27.23	0.33%
0 - 90%	15 - 20	26.69	26.78	0.34%
0 - 90%	20 - 50	31.26	31.41	0.48%
0 - 30%	10 - 50	59.25	60.19	1.59%
30 - 90%	10 - 50	29.88	30.04	0.20%
0 - 90%	10 - 50	84.95	86.07	0.14%

954 The percentage deviations are quote the systematics due to BDT dependence on the B_s^0 invariant
 955 mass. We can see that the systematics uncertainties on the signal raw yield due to the BDT
 956 dependence on the B_s^0 invariant is relatively small (within 1.6%) and will not affect our final
 957 results significantly.

DRAFT

958 **A Cut Optimization**

959 In this section the plots referring to the [10, 15] and [15, 20] GeV $B_s^0 p_T$ bins are presented.

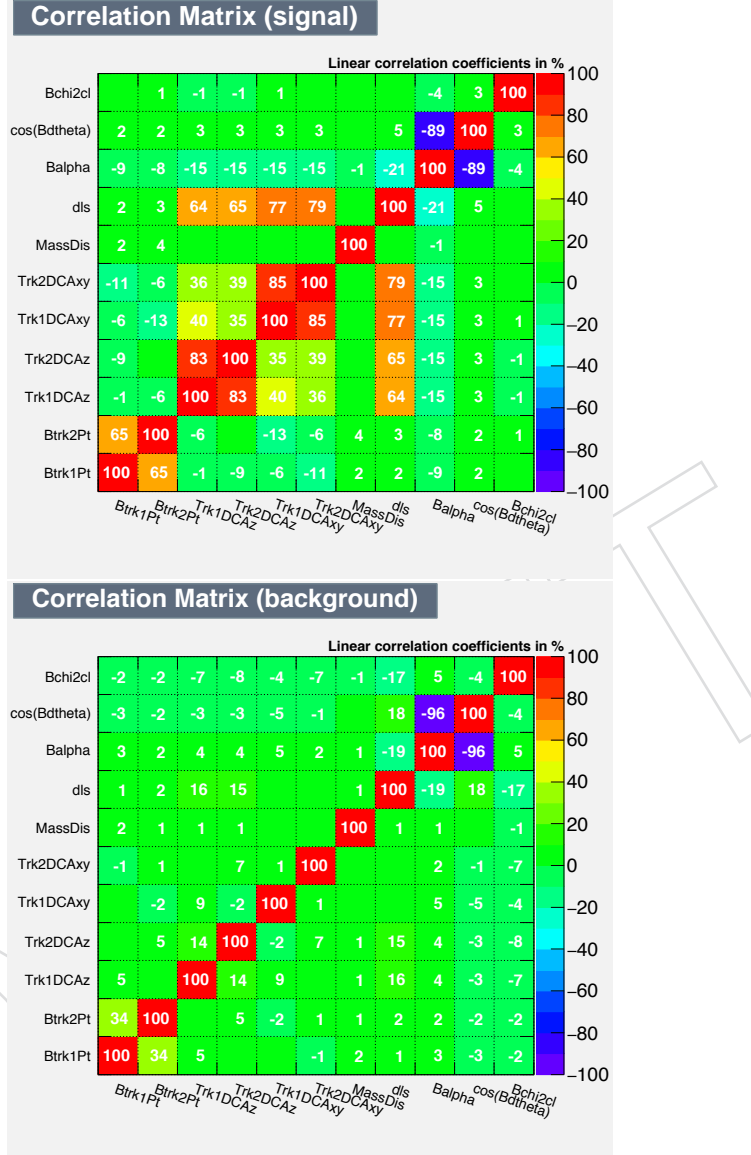


Figure 87: Correlation matrix between the variables used in MVA training for signal and background $B_s^0 p_T$ 10 to 15 GeV/c

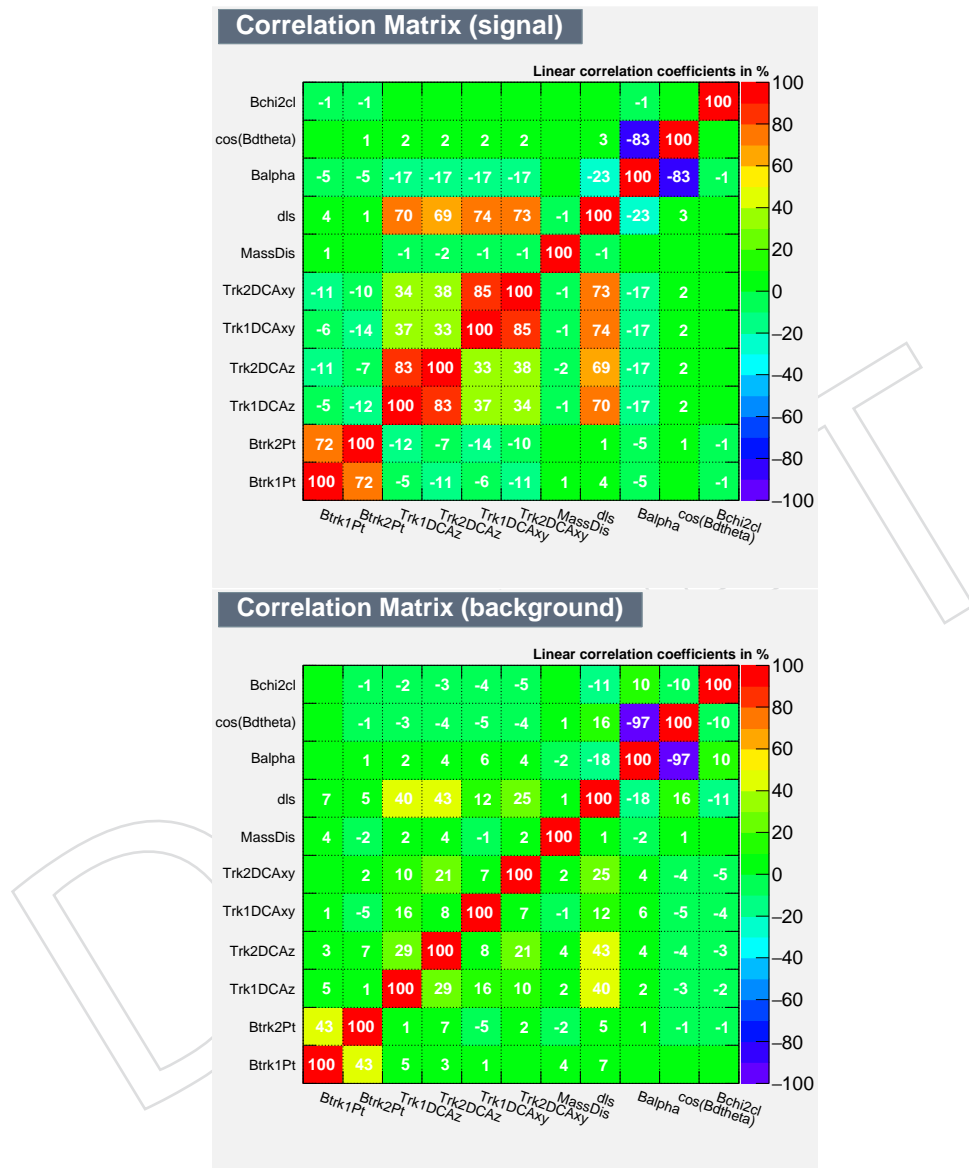


Figure 88: Correlation matrix between the variables used in MVA training for signal and background $B_s^0 p_T$ 15 to 20 GeV/c

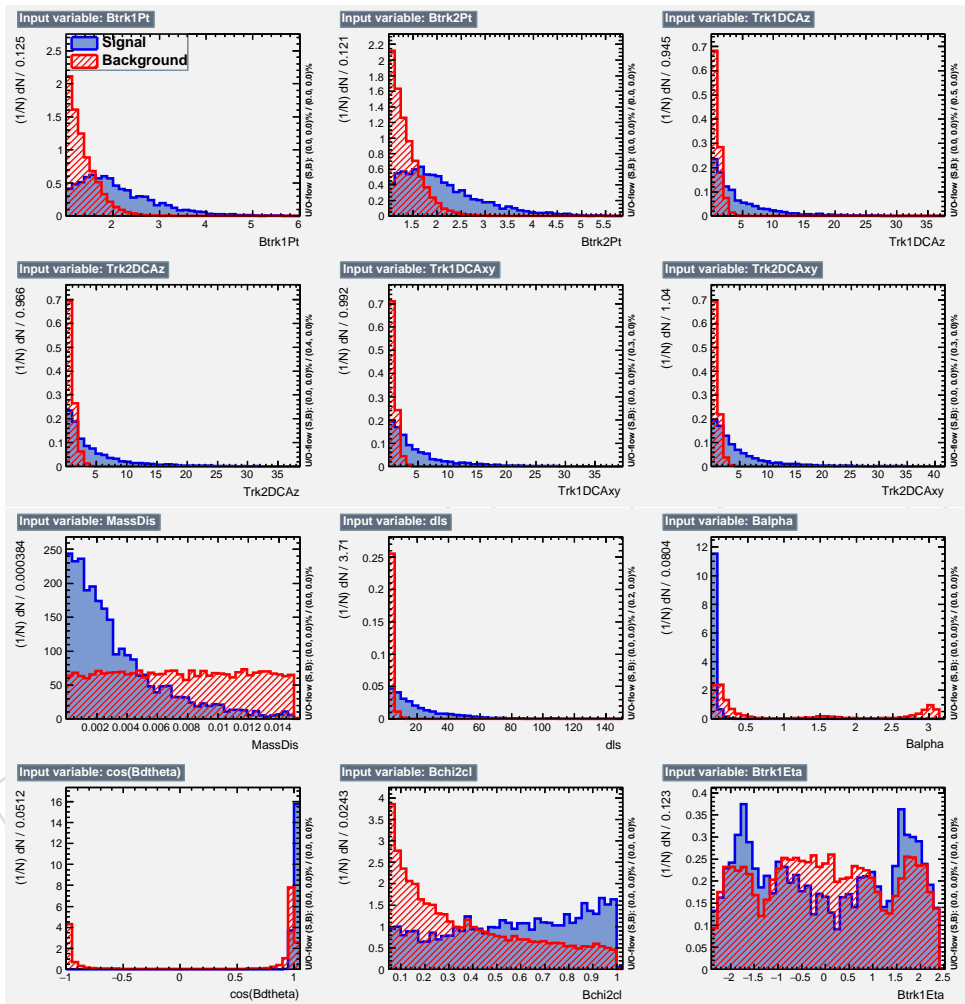


Figure 89: Input variables distributions for training used in PbPb B_s^0 p_T 10-15 GeV/c.

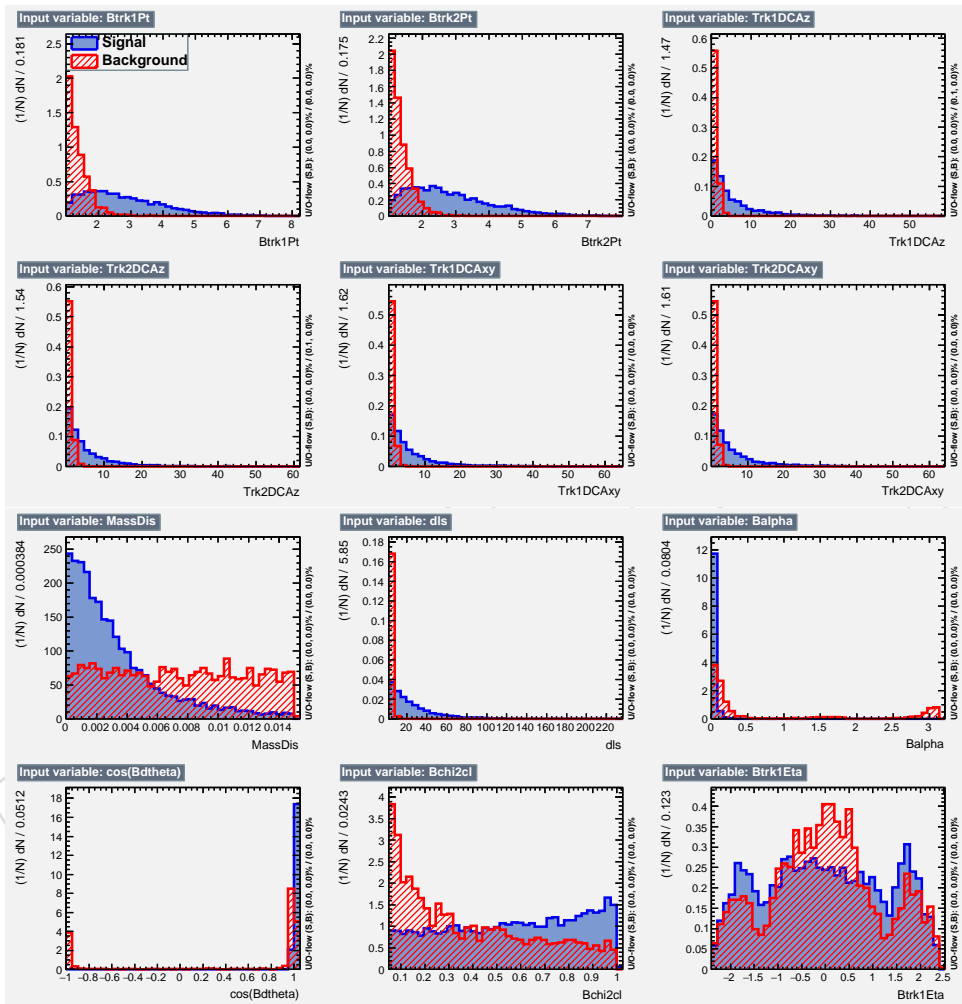


Figure 90: Input variables distributions for training used in $\text{PbPb } B_s^0 p_T 15-20 \text{ GeV}/c$.

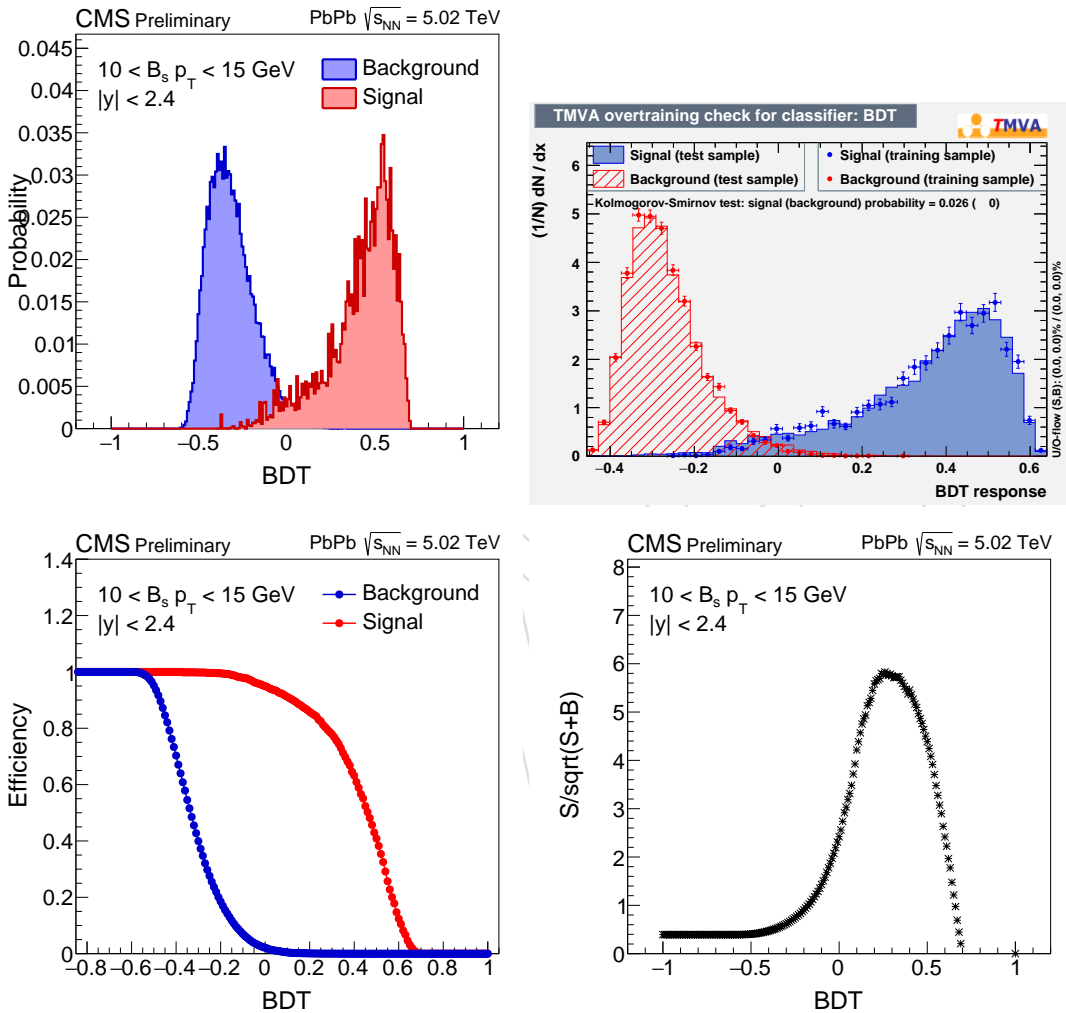


Figure 91: BDT distribution of signal and background from training sample (upper left) and the over train test (upper right). Efficiency as a function of BDT for training and testing samples (lower left). $S/\sqrt{S+B}$ as a function of BDT for $10-15 \text{ GeV}/c$ in PbPb collisions (lower right).

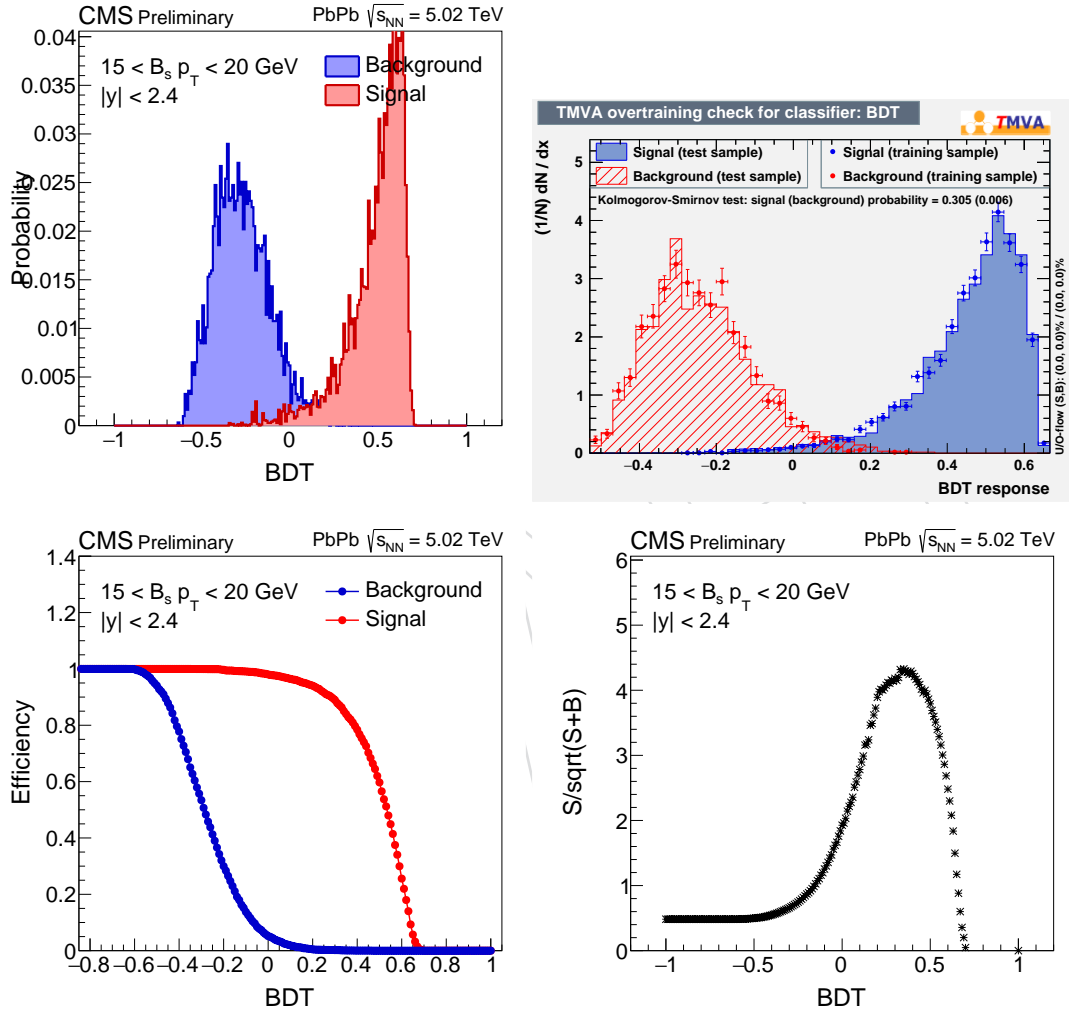


Figure 92: BDT distribution of signal and background from training sample (upper left) and the over train test (upper right). Efficiency as a function of BDT for training and testing samples (lower left). $S/\sqrt{S+B}$ as a function of BDT for $15-20 \text{ GeV}/c$ in PbPb collisions (lower right).

960 B Systematics

961 In this section are included the plots related to the systematics calculated in the B_s^0 p_T bins of
 962 [10,15] and [15,20] GeV for p_T and 0 - 30%, 30% - 90%, and 0 - 90% for centrality.

963 B.1 Selection Efficiency

964 The following is for selection efficiency systematics study by B^+ track variables in inclusive p_T .

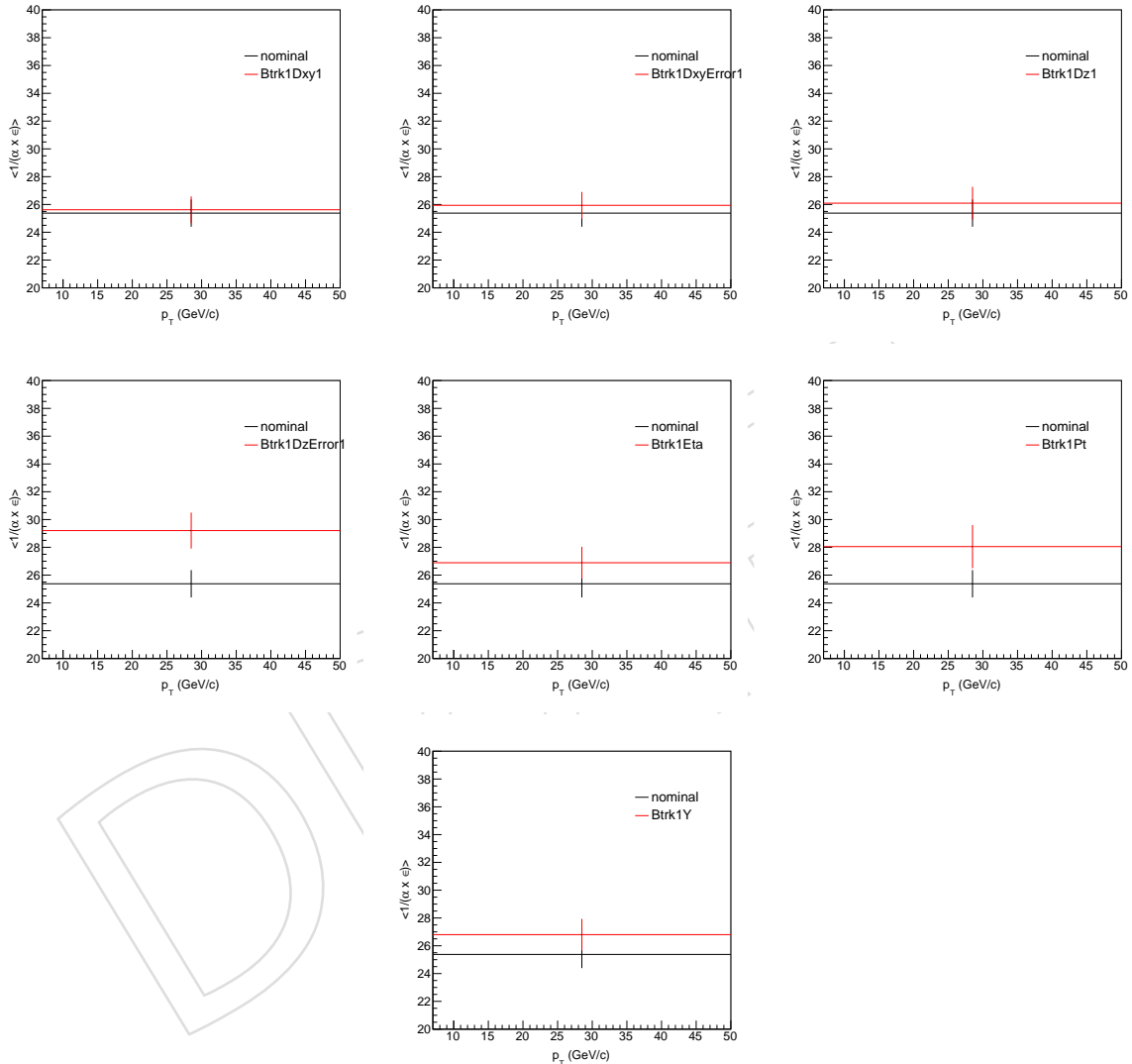


Figure 93: Track variable weighted and unweighted $\langle \frac{1}{\alpha \times \epsilon} \rangle$ comparison for 0 - 90% inclusive p_T . From left to right, top to bottom, the variables used are Btrk1Dxy1, Btrk1DxyError1, Btrk1Dz1, Btrk1DzError1, Btrk1Eta, Btrk1Pt, Btrk1Y, respectively.

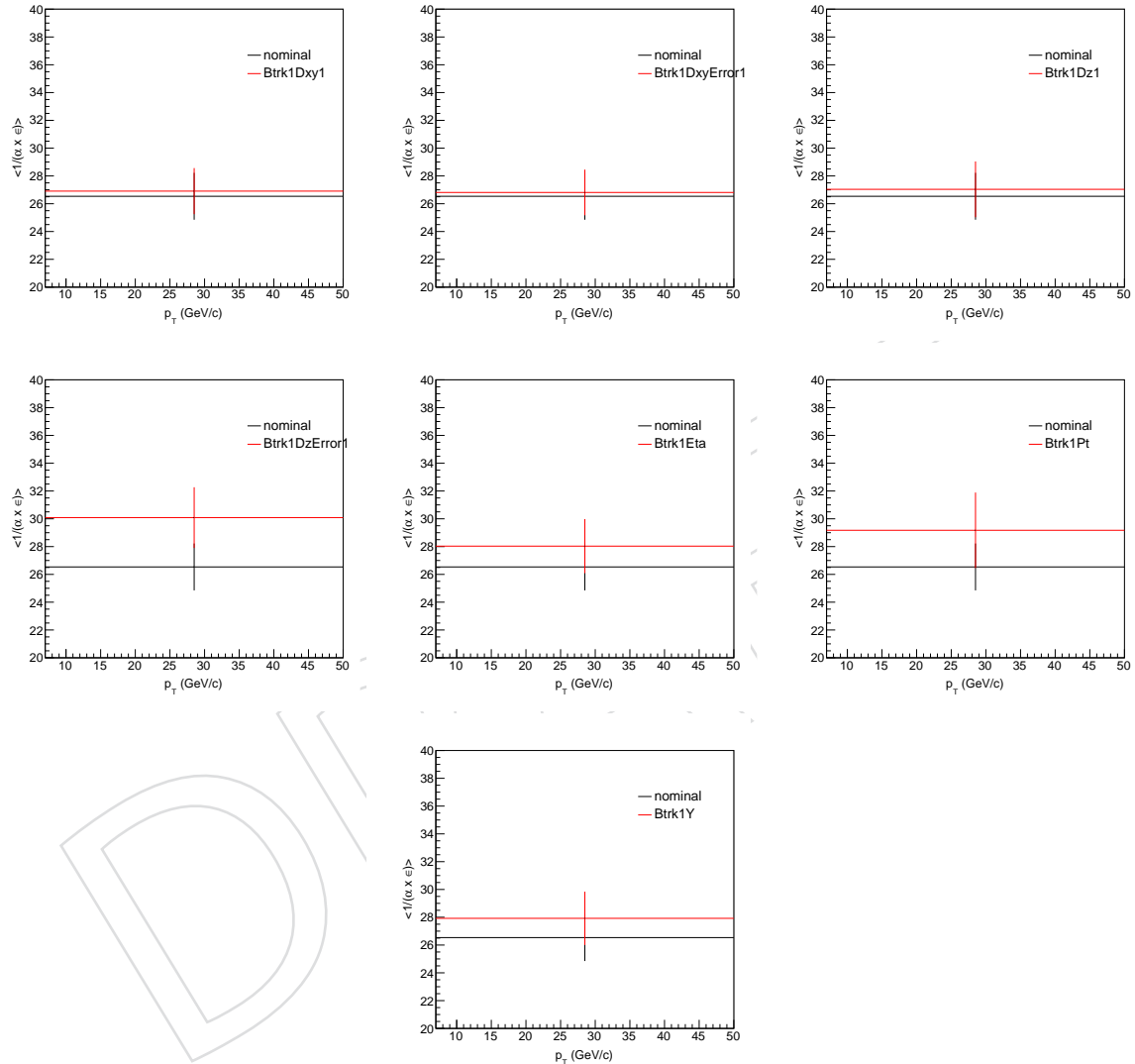


Figure 94: Track variable weighted and unweighted $\langle \frac{1}{\alpha \times \epsilon} \rangle$ comparison for 0 - 30% inclusive p_T . From left to right, top to bottom, the variables used are Btrk1Dxy1, Btrk1DxyError1, Btrk1Dz1, Btrk1DzError1, Btrk1Eta, Btrk1Pt, Btrk1Y, respectively.

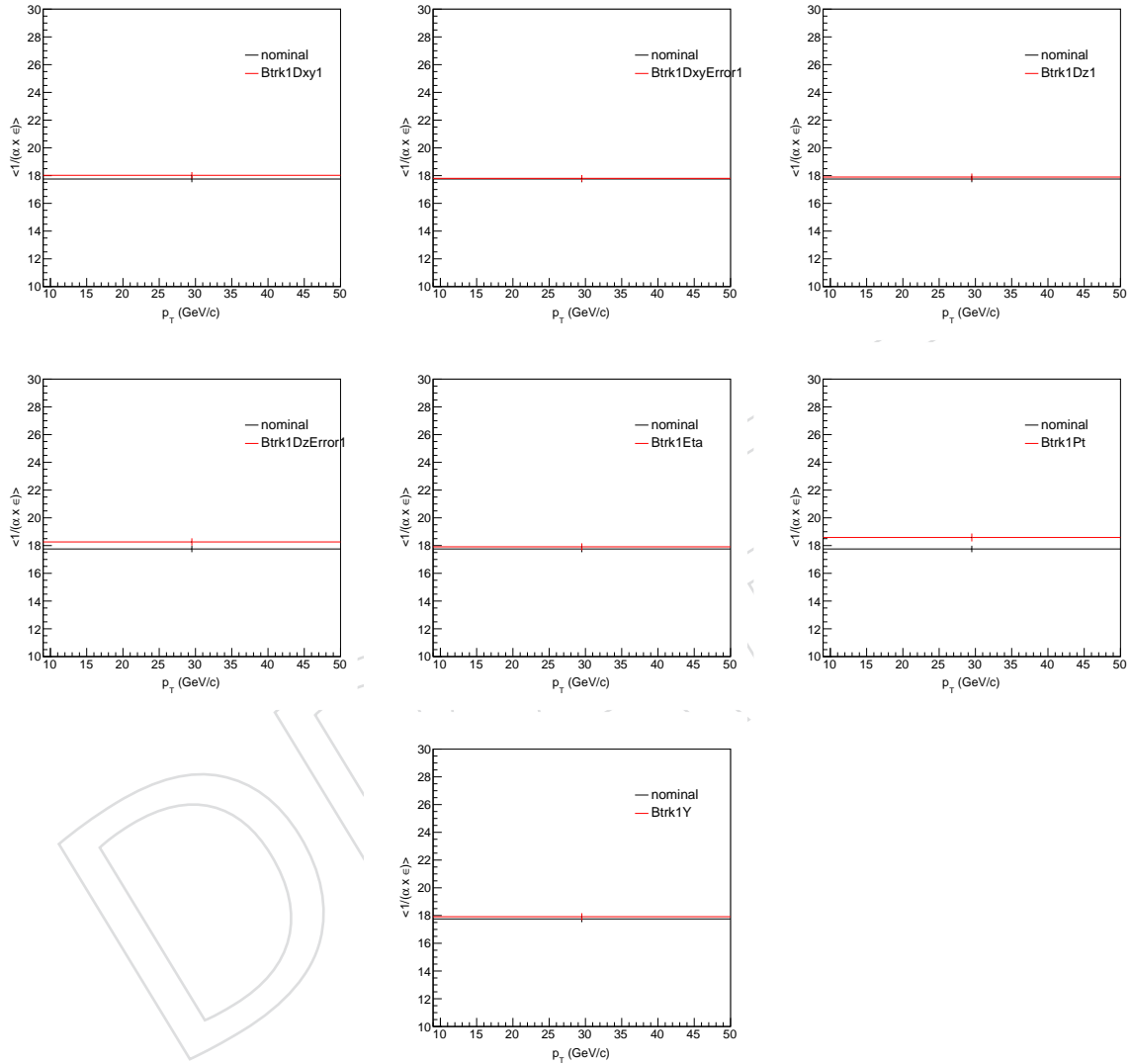


Figure 95: Track variable weighted and unweighted $\langle \frac{1}{\alpha \times \epsilon} \rangle$ comparison for 30 - 90% inclusive p_T . From left to right, top to bottom, the variables used are Btrk1Dxy1, Btrk1DxyError1, Btrk1Dz1, Btrk1DzError1, Btrk1Eta, Btrk1Pt, Btrk1Y, respectively.

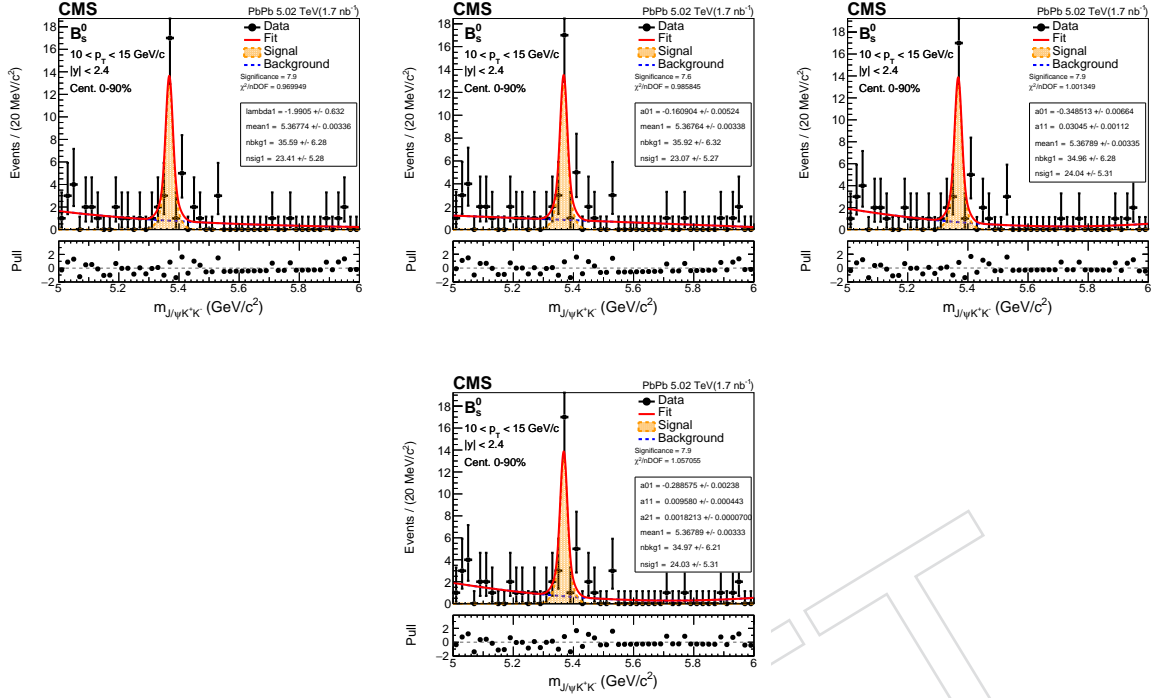
965 **B.2 Signal Extraction**

Figure 96: Invariant mass fit of B_s^0 candidates for $10 < p_T < 15 \text{ GeV}/c$ in 5.02 TeV PbPb. The background PDF from left to right is default exponential, linear, 2nd order polynomial and 3rd order polynomial.

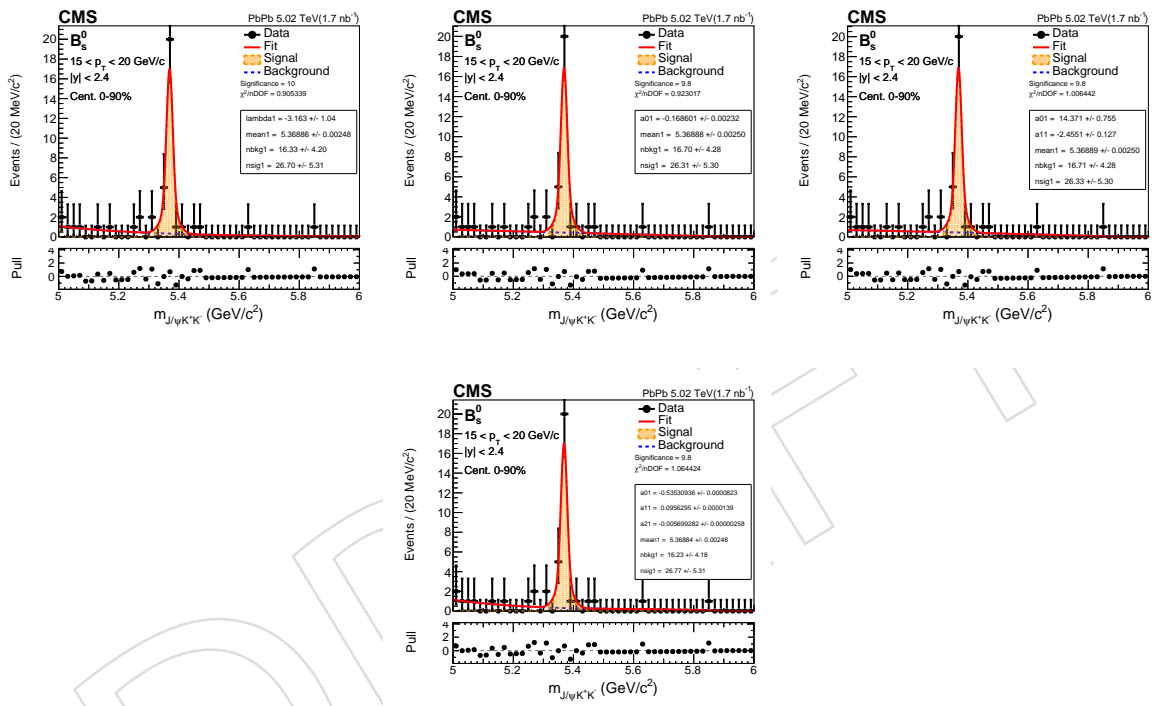


Figure 97: Invariant mass fit of B_s^0 candidates for $15 < p_T < 20$ GeV/c in 5.02 TeV PbPb. The background PDF from left to right is default exponential, linear, 2nd order polynomial and 3rd order polynomial.

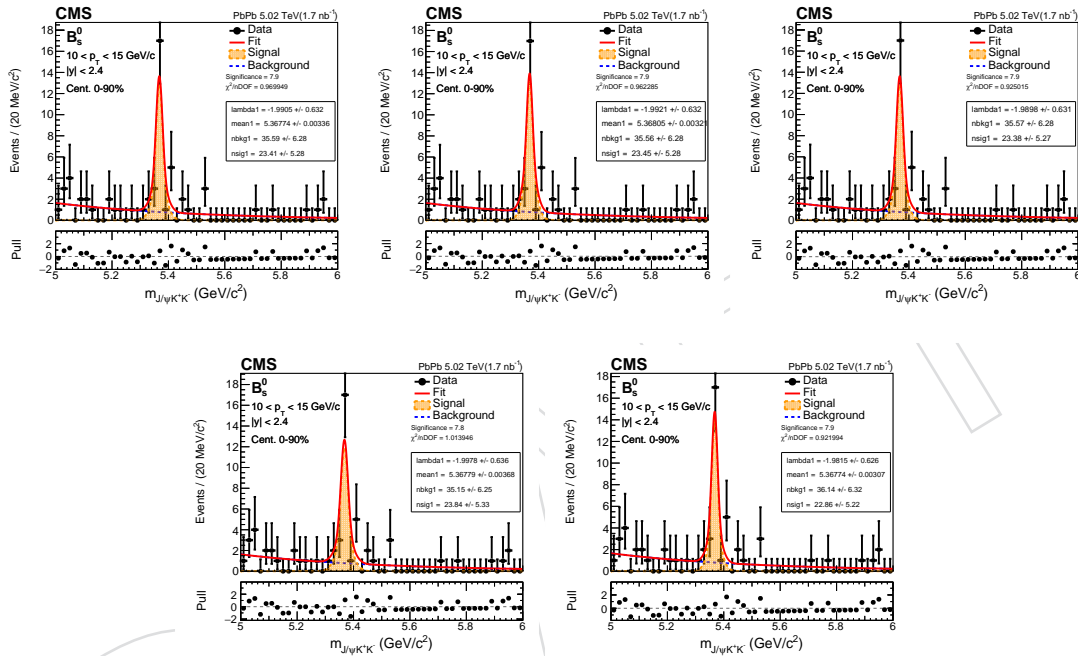


Figure 98: Invariant mass fit of B_s^0 candidates for $B_s^0 p_T$ from 10 to 15 GeV/c in 5.02 TeV PbPb. The signal pdf from left to right is default double gaussian (with widths and relative proportion fixed from MC), triple gaussian (with widths and relative proportions fixed from MC), double gaussian with all the parameters fixed (including the mean), increased width ($a=1.1$), and decreased width ($a=0.9$).

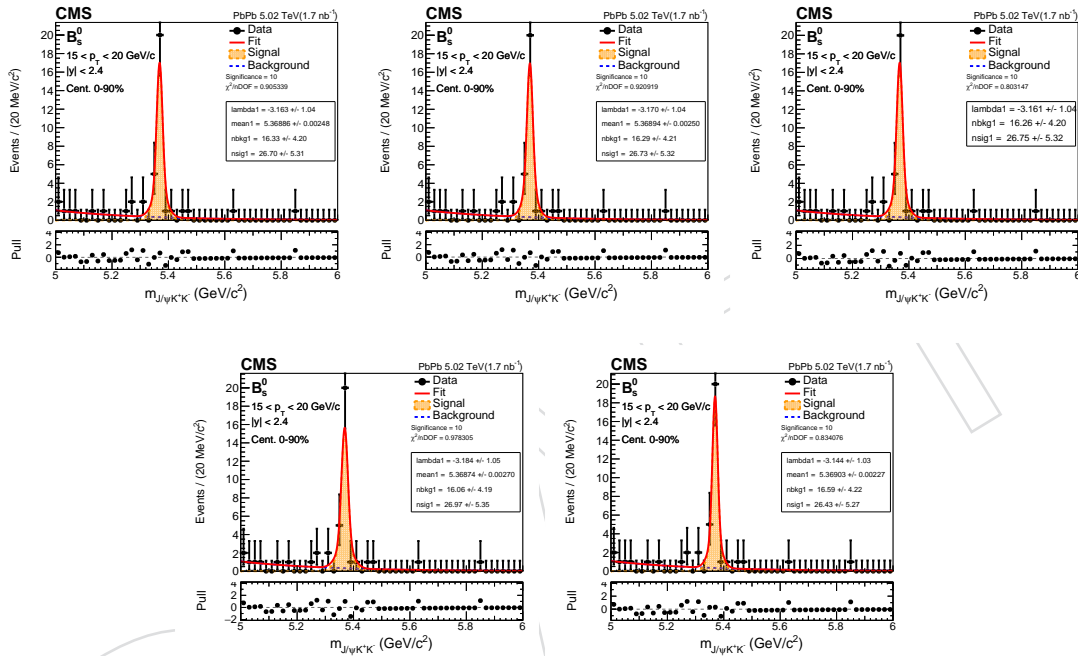


Figure 99: Invariant mass fit of B_s^0 candidates for $B_s^0 p_T$ from 15 to 20 GeV/c in 5.02 TeV PbPb. The signal pdf from left to right is default double gaussian (with widths and relative proportion fixed from MC), triple gaussian (with widths and relative proportions fixed from MC), double gaussian with all the parameters fixed (including the mean), increased width ($a=1.1$), and decreased width ($a=0.9$).

966 C Non-prompt J/ψ background

967 The production of J/ψ mesons occurs in three ways. The prompt J/ψ produced directly in
 968 the proton-proton collision or indirectly via the decay of heavier charmonium states, and non-
 969 prompt J/ψ from the decay of a b hadron. Non-prompt J/ψ lead to a measurement of the b-
 970 hadron cross section. There are potential background feed-down sources coming from other B
 971 meson decays in the B_s^0 invariant mass spectrum. These sources form a peaking structure in the
 972 region of interests. In order to prevent the potential bias of the yield extraction procedure, the
 973 peaking background structures need to be properly studied. To determine these components,
 974 we processed the inclusive B meson (i.e., non-prompt J/ψ) MC samples with the nominal B_s^0
 975 channel work flow. We then classify each reconstructed B_s^0 candidate by their gen-level particle,
 976 e.g. whether it is coming from a B^0 , B^+ or other decays that falls into the B_s^0 reconstruction work
 977 flow, in order to measure their individual contribution to the peaking structure.

978 Only a relatively small contribution from other B meson is observed. After applying opti-
 979 mal cuts, only negligible non-prompt contribution is left. This is due to the narrow ϕ meson
 980 natural width allowing we impose a tight track-pair mass window and thus remove a large
 981 fraction of non-prompt contribution which does not have an intermediate ϕ resonance. These
 982 contributions are presented below.

983 C.1 Individual channel contributions of NP Background

984 There are many small contributions that gives the form to the peaking background structure.
 985 We can not identified each of them individually but most of the contributed ones are deter-
 986 mined. Below is a list of example processes that compose of the majority of the peaking back-
 987 ground:

- 988 • 1 st case $X \rightarrow J/\psi\pi^-K^+$, here pion is mis-identified as kaon
- 989 • 2 nd case $B_s^0 \rightarrow J/\psi K^+K^-$, in which both Kaons are not coming from the decay of
 990 an intermediate ϕ meson resonance.
- 991 • 3 rd case $B^+ \rightarrow J/\psi K^+$, (added extra K^-)
- 992 • 4 th case $X \rightarrow J/\psi\pi^+\pi^-$, pions mis-identified as Kaons.
- 993 • 5 th case $B_s^0 \rightarrow J/\psi K^+K^-X$
- 994 • 6 th case $B_s^0 \rightarrow J/\psi\phi\pi\pi$
- 995 • 7 th case $B^0 \rightarrow J/\psi K^{*0}$

996 100 shows the contribution of the determined channels with respect to the total background
 997 after applying optimal cuts for PbPb for all $5 \text{ GeV}/c < p_T < 10 \text{ GeV}/c$, $10 \text{ GeV}/c < p_T < 15$
 998 GeV/c , $10 \text{ GeV}/c < p_T < 20 \text{ GeV}/c$, $20 \text{ GeV}/c < p_T < 50 \text{ GeV}/c$, and $5 - 50 \text{ GeV}/c$. The peak
 999 at the B_s^0 signal region was investigated and found out that mostly contributed channels are
 1000 $B^0 \rightarrow J/\psi K^{*0}$ in grey color and $B_s^0 \rightarrow J/\psi K^+K^-$ in black color.

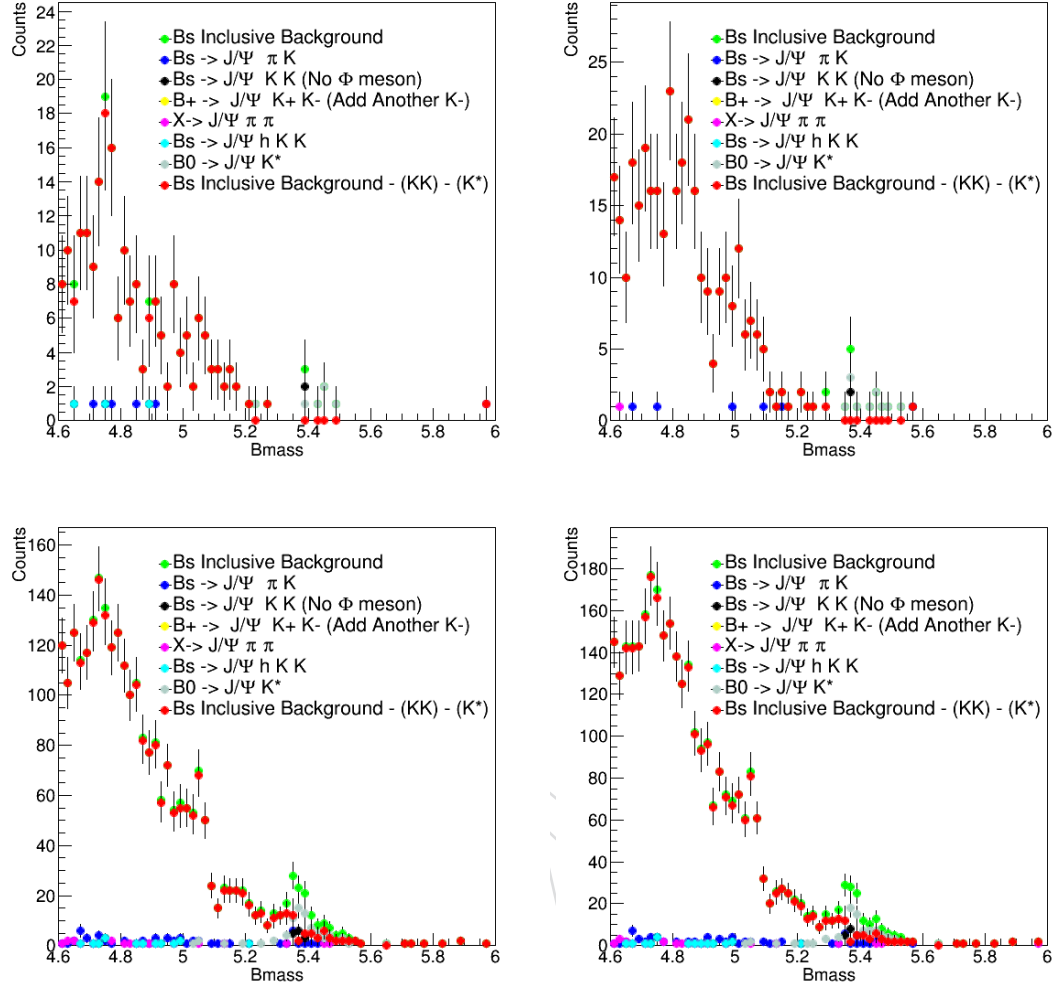


Figure 100: Individual Non Prompt background contributions with respect to the total background components for 10 to 15 GeV (top left), 15 to 20 GeV (top right), 20 to 50 GeV (bottom left), and 10 to 50 GeV (bottom right) for PbPb sample. We can see that the non-prompt background from all channels listed above are negligible compared to the inclusive background. Also, the no peak near the B_s resonance is observed when the inclusive background subtract the $B^0 \rightarrow J/\psi K^{*0}$ and $B_s \rightarrow J/\psi K^+ K^-$ components.

1001 101 also includes the signal component in the distribution. We can see that the non-prompt
 1002 background is insignificant compared to the total inclusive background and the inclusive back-
 1003 ground is low comparing to the $B_s \rightarrow J/\Psi\phi \rightarrow J/\Psi K^+ K^-$ signal in our studies.

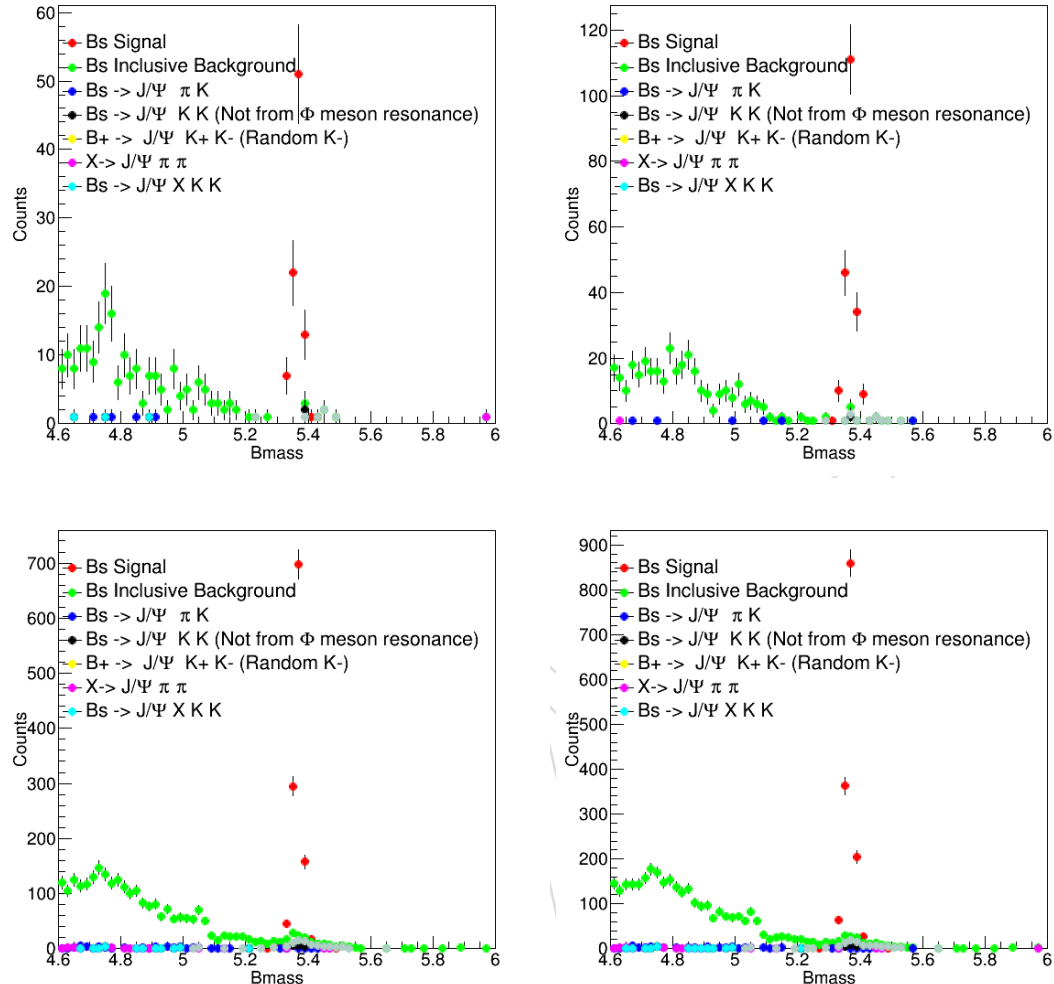


Figure 101: Individual Non Prompt background contributions with respect to the total background components and the signal channel for 10 to 15 GeV (top left), 15 to 20 GeV (top right), 20 to 50 GeV (bottom left), and 10 to 50 GeV (bottom right) for PbPb sample. We can see that the inclusive background is small compared to the signal we used in our studies.

1004 C.2 B meson contribution of NP Background

1005 From the non-prompt background studies above, we can see that there are many small contri-
 1006 butions. Those small components together summed up constructing a large background and
 1007 we can not identify all of them individually. Under this circumstances, another definition of in-
 1008 dividual component defined. The new definition of the NP background components are listed
 1009 below;

- 1010 • 1 st case : $B^+ \rightarrow J/\psi X$, all contribution from B^+
- 1011 • 2 nd case : $B_s^0 \rightarrow J/\psi X$, all contribution from B_s^0
- 1012 • 3 rd case : $B^0 \rightarrow J/\psi X$, all contribution from B^0
- 1013 • 4 th case : Other contributions

1014 In figure 102 the signal region is dominated by the B^0 , B^+ , and B_s^0 decays while the other
 1015 channels are contributed on the left side of the mass spectrum. For both pp and PbPb data, the
 1016 B_s^0 to $J/\psi + X$ (orange region) makes a big contribution.

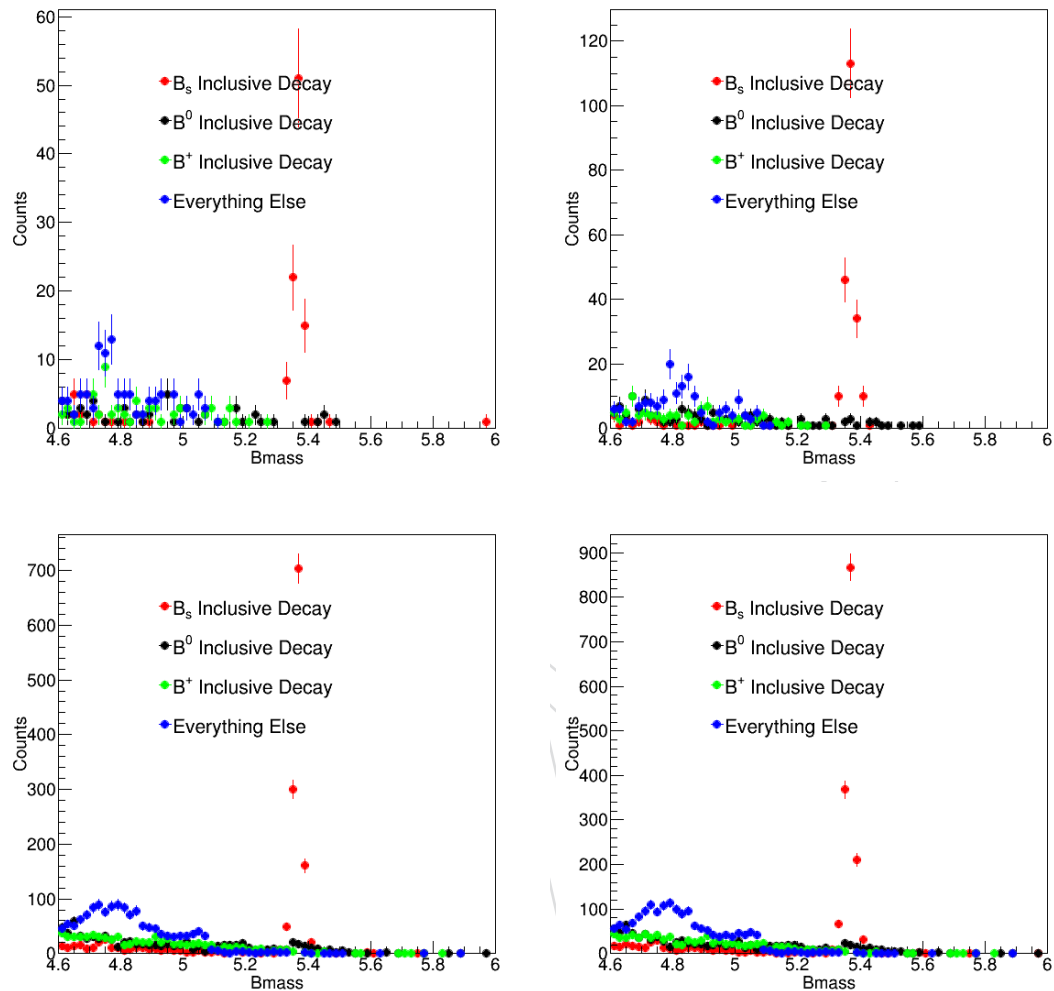


Figure 102: B^+ , B_s^0 , B^0 channels make nearly equal contribution in the signal region for all p_T bins 10 - 15 GeV/c, 15 - 20 GeV/c, 20 - 50 GeV/c, and 10 - 50 GeV/c.

1017 References

- 1018 [1] Y. L. Dokshitzer and D. E. Kharzeev, "Heavy quark colorimetry of QCD matter", *Phys.*
1019 *Lett.* **B519** (2001) 199–206, doi:10.1016/S0370-2693(01)01130-3,
1020 arXiv:hep-ph/0106202.
- 1021 [2] CMS Collaboration, "Measurement of the charged particle nuclear modification factor in
1022 PbPb collisions at $\sqrt{s_{\text{NN}}} = 5.02 \text{ TeV}$ ", Technical Report CMS-PAS-HIN-15-015, CERN,
1023 Geneva, 2016.
- 1024 [3] CMS Collaboration, "D⁰ meson nuclear modification factor in PbPb collisions at
1025 $\sqrt{s_{\text{NN}}} = 5.02 \text{ TeV}$ ", Technical Report CMS-PAS-HIN-16-001, CERN, Geneva, 2016.
- 1026 [4] CMS Collaboration, "Measurement of B_s⁰ meson production in pp and PbPb collisions at
1027 $\sqrt{s_{\text{NN}}} = 5.02 \text{ TeV}", Submitted to: Phys. Lett.$ (2018) arXiv:1810.03022.
- 1028 [5] CMS Heavy Ion Group, "Charmonia in 5.02 tev data", CMS Analysis Note 2016/067,
1029 CERN, 2016.
- 1030 [6] T. Sjöstrand, S. Mrenna, and P. Skands, "PYTHIA 6.4 physics and manual", *JHEP* **05**
1031 (2006) 026, doi:10.1088/1126-6708/2006/05/026, arXiv:hep-ph/0603175.
- 1032 [7] R. Field, "Early LHC Underlying Event Data – Findings and Surprises", in *Hadron*
1033 *collider physics. Proceedings, 22nd Conference, HCP 2010, Toronto, Canada, August 23-27,*
1034 2010. arXiv:1010.3558.
- 1035 [8] D. Lange, "The EvtGen particle decay simulation package", *Nucl.Instrum.Meth.* **A462**
1036 (2001) 152–155, doi:10.1016/S0168-9002(01)00089-4.
- 1037 [9] E. Barberio, B. van Eijk, and Z. Was, "PHOTOS: A Universal Monte Carlo for QED
1038 radiative corrections in decays", *Comput.Phys.Commun.* **66** (1991) 115–128,
1039 doi:10.1016/0010-4655(91)90012-A.
- 1040 [10] I. P. Lokhtin and A. M. Snigirev, "A model of jet quenching in ultrarelativistic heavy ion
1041 collisions and high- p_T hadron spectra at RHIC", *Eur. Phys. J.* **C45** (2006) 211,
1042 doi:10.1140/epjc/s2005-02426-3, arXiv:hep-ph/0506189.
- 1043 [11] CMS Heavy Ion Group, " b^+ production in pbpb collisions at $\sqrt{s_{\text{NN}}} = 5.02 \text{ tev}$ ", CMS
1044 Analysis Note 2019/132, CERN, 2019.
- 1045 [12] Particle Data Group, "Review of particle physics", *Phys. Rev. D* **98** (2018) 030001,
1046 doi:10.1103/PhysRevD.98.030001.
- 1047 [13] CMS Heavy Ion Group, "Dimuon performance studies in 2015 5.02tev pp and pbpb
1048 data", CMS Analysis Note 2016/048, CERN, 2016.
- 1049 [14] A. Hoecker et al., "TMVA: Toolkit for Multivariate Data Analysis", *PoS ACAT* (2007)
1050 040, arXiv:physics/0703039.
- 1051 [15] M. Pivk and F. R. Le Diberder, "SPlot: A Statistical tool to unfold data distributions",
1052 *Nucl. Instrum. Meth.* **A555** (2005) 356–369, doi:10.1016/j.nima.2005.08.106,
1053 arXiv:physics/0402083.
- 1054 [16] CMS Heavy Ion Group, "B meson production in pbpb data: signal extraction and mc
1055 validation", CMS Analysis Note 2019/219, CERN, 2019.

- 1056 [17] CMS Collaboration Collaboration, "Measurement of the B^\pm meson nuclear modification
1057 factor in pb-pb collisions at $\sqrt{s_{NN}} = 5.02$ TeV", *Phys. Rev. Lett.* **119** (Oct, 2017) 152301,
1058 doi:10.1103/PhysRevLett.119.152301.

DRAFT